UNIVERSITY OF TWENTE.

Faculty of Engineering & Technology

Improving the prediction of pressure gradient field in wind farm numerical simulation method, WAKEFARM

Gopala Krishnan Sankara Subramanian
Sustainable energy technology
M Sc. Thesis
October 2018
EFD-293

Supervisors:
dr. ir. Arne van Garrel
dr. Hüseyin Özdemir (Mentor ECN)
ir. Edwin Bot (Mentor ECN)

Faculty of Engineering & Technology,
Engineering Fluid Dynamics
University of Twente
P.O. Box 217
7500 AE Enschede
The Netherlands

Assessment committee

Supervisor
dr.ir.Arne van Garrel
Engineering fluid dynamics,
University of Twente

Chairman
Prof.dr.ir.C.H.Venner
Engineering fluid dynamics,
University of Twente

Supervisor from company
ir. Edwin Bot
Researcher, wind energy
Energy research centre of the netherlands

External member
dr. Maarten.J. Arentsen
Faculty of Behavioural, Management and Social Sciences
University of Twente

Abstract

The wind turbines in a wind farm interact aerodynamically through their wakes. The wakes are characterized by reduced wind speeds and increased turbulence. These wake effects influence the overall power production of the wind farm and cause additional fatigue loading. The numerical modelling of wind farms is vital, as it helps us to understand the wind turbine wake interactions and to predict the total power output of the wind farm better. The current wake model at the Energy research Centre of the Netherlands is implemented into a Fortran code named WAKEFARM. It simulates the wake properties of a single turbine or a row of turbines. WAKE-FARM solves Reynolds averaged Navier Stokes equations in perturbation form. The Reynolds averaged Navier Stokes equations used in WAKEFARM are parabolized in the streamwise direction. The two momentum equations in the transverse directions are elliptic and are solved iteratively. The axial pressure gradient in the axial momentum equation is neglected in the far wake and prescribed along with the body force, in the near wake. This axial pressure gradient is calculated using an inviscid vortex models. The induced velocity vectors calculated from the vortex model are given as initial guesses to the perturbation variables in the three momentum equations. In this thesis work, two vortex methods that give an improved prediction of the pressure gradient field are developed: model of a wind turbine rotor with more than three blades with span varying circulation and constant axial induction along the span and a model of a real wind turbine having three blades with span varying circulation and axial induction distributed along the span. Both the models trail a helical wake. The root vortex is included in both the models. The axial pressure gradient is calculated from inviscid, incompressible Navier Stokes equations. The trend in the calculated axial pressure gradient is in good agreement with the momentum theory. The two new near wake models (vortex models) are implemented in WAKE-FARM. The horizontal velocity profiles in the cross-flow direction at hub height are validated with field measurements in ECNs wind turbines test site in wieringemeer. The constant axial induction model correlates well with the experiments compared to the existing vortex models. The implementation of the root vortex was successful. The new method shows a flattened velocity profile near the centre of the wake, due to the influence of root vortex. The centerline velocity profiles are validated with wind

tunnel measurements in Marchwood laboratories. The centerline velocity profile at 5 rotor diameters downstream of the turbine, predicted by the constant axial induction model has the best correlation with the Marchwood experiments. The new constant axial induction model shows an improvement in comparisons with experiments.

Contents

List of Figures

List of Tables

List of Symbols

Symbols	Description	Units
a	Axial induction factor in the rotorplane	-
c	Chord distribution	m
C_l	Lift coefficient	-
C_μ, $C_{\varepsilon 1}$,$C_{\varepsilon 3}$,$C_{\varepsilon 3}$	Constants in $k - \varepsilon$ model	-
C_t	Thrust coefficient at rotor	-
D	Rotor diameter	m
$\varepsilon_0(z)$	Undisturbed dissipation rate of turbulent kinetic energy profile	J/kgs
H	Hub height	m
h	Pitch of helix	m
$k_0(z)$	Undisturbed turbulent kinetic energy profile	J/kg
k	Von Karman constant	-
L	Monin-Obukhov length scale	m
l	Torsional parameter of helix	m
L_{MBL}	Length scale in middle boundary layer	m
L_{UBL}	Length scale in upper boundary layer	m
L_{SL}	Surface layer Length scale	m
N_r	Number of spanwise vortex filaments	-
N_h	Number of streamwise vortex filaments	-
N_b	Number of blades	-
p	Pressure	Pa
R	Rotor radius	m
R_r	Root radius	m
L_w	Length of wake	
$\theta_0(z)$	Undisturbed potential temperature profile	K
$u_0(z)$	Undisturbed wind speed	m/s
U_∞	Undisturbed wind speed at hub height H	m/s
u_*	Friction velocity at roughness length	m/s
u	Velocity deficit in $x-$ direction	m/s
$\overline{u}_{ij}$	Velocity induced by a vortex ring j, at a point i	m/s
V_a	Total axial velocity induced by circular vortex rings	m/s
V_{axial}	Total axial induced velocity at the blade element	m/s
V_t	Total tangential velocity induced by circular vortex rings	m/s
V_{tan}	Total tangential induced velocity at the blade element	m/s

Symbols	Description	Units
V_p	Total velocity perceived at the blade element	m/s
V_y	Total velocity induced by a vortex rings in $y-$ direction	m/s
V_z	Total velocity induced by a vortex rings in $z-$ direction	m/s
v	Velocity deficit in $y-$ direction	m/s
w_x	Axial velocity induced by a single circular vortex ring	m/s
w_y	Tangential velocity induced by a single circular vortex ring	m/s
w	Velocity deficit in $z-$ direction	m/s
θ	Potential temperature perturbation	K
k	Perturbation in turbulent kinetic energy	J/kg
ε	Perturbation in dissipation rate of turbulent kinetic energy	J/kgs
x	Coordinate in wind direction	m
$x(t)$	x coordinate of helix	m
X_{end}	Length of computational domain in x-direction	m
y	Coordinate in cross flow direction	m
$y(t)$	y coordinate of helix	m
Y_{end}	Length of computational domain in y-direction	m
z	Coordinate in vertical direction	m
$z(t)$	z coordinate of helix	m
Z_{end}	Length of computational domain in z-direction	m
z_0	Roughness length	m
λ	Tip speed ratio	-
ω	Angular velocity of blade	rad/s
ω_w	Angular velocity of wake	rad/s
γ_t	Tangential vortex density	m^2/s
Γ_b	Bound circulation of blade	m^2/s
Γ_t	Trailed vortex strength	m^2/s
τ_{ij}^R	Reynolds stress	Pa
ϕ	Inflow angle at the blades	$\circ$

Symbols	Description	Units
α	Angle of attack at the blade section	$\circ$
β	Blade twist angle	$\circ$
ν_t	Eddy viscosity	m^2/s
δ_{ij}	Kronecker delta	-
ρ	Density	kg/m^3
β	Expansion coefficient	K^{-1}
g	Gravitational acceleration	m/s^2
R_f	Richarson number	-
U_e	Velocity at hub height far downstream	m/s
U_R	Velocity at the rotor of the wind turbine	m/s
$\overline{U_i}$	Mean flow in RANS equations	m/s
Ψ_m, Ψ_h	Stability functions in undisturbed flow model	-
f	Coriolis force	N

Abbreviations

Abbreviaton	Meaning
ABL	Atmospheric Boundary Layer
ADI	Alternating Direction Implicit
ECN	Energy research Centre of the Netherlands
EWTW	ECN Wind turbine Test site Wieringermeer
RANS	Reynolds averaged Navier-Stokes equations
SIMPLE	Semi Implicit Method for Pressure Linked Equations
CFD	Computational Fluid Dynamics
LES	Large Eddy Simulation
DNS	Direct Numerical Simulation

Chapter 1

Introduction

Climate change has already had many adverse effects on the environment. These include the melting of glaciers, rising sea levels and an increase in the number of heat waves. To curtail the harmful effects of climate change, both developing and developed countries have to curb their CO_2 emissions. In 2016, coal, oil, and natural gas had an energy supply share of 28.1%, 31.7%, and 21.6% respectively [13]. With a total of 81.4% of the energy supply coming from fossil fuels, energy production is the main concern in reducing climate change. To achieve CO_2 reduction goals, most of the energy must be generated using renewable methods. In addition to this fossil fuels are also getting depleted. With the exhaustion of conventional sources of energy and an increase of global warming, the need for renewable energy sources like wind energy is evident. It is impossible to generate the entire energy demand using just solar, hydropower and geothermal. Wind turbines are one of the cheapest forms of producing energy through renewables. Though the energy production through fossil fuels is cheaper, the real price we pay in the means of climate change and air pollution is high. Compared to solar panels, power production using wind turbines is energy intense. A single $250 kW$ wind turbine produces the same amount of energy as 2500 solar panels in the same time span. The land food print needed by wind turbines is lesser compared to the land footprint needed by solar panels to produce the same amount of energy. The demand for wind energy is increasing. The Global Wind Energy Council states that by 2030, wind turbines will account for 19% of all globally generated energy, and by 2050, the percentage will rise up to 30

Space for installation of turbines is however limited, hence smaller wind farms with closer spacing between the wind turbines have to be developed. The wind turbines in wind farm interact aerodynamically through their wakes. The wakes of wind turbines are characterized by reduced wind speeds and increased turbulence. These wake effects influence the overall power production of the wind farm and cause additional fatigue loading. An estimated $10 - 20\%$ power losses happen in large wind farms due to wake effects [14, 15, 16]. An incorrect analysis of the wake

1

effects can result in a bad wind farm layout, which can generate significant energy losses and increase the fatigue loads. This, in turn will affect the cash flow of the project [17]. In order to minimize these wake effects, we have to optimize the wind farm layout, so that the turbines feel these wake effects as little as possible. The numerical modelling of wind farms is vital, as it helps us to understand the wind turbine wake interactions and to predict the total power output of the wind farm better. Simulating an entire wind farm using CFD, where the flow is resolved everywhere, takes a very long time which is not practical during the design phase. The computational time can be reduced drastically by making several simplifications to the governing equations. ECNs wake model is implemented into a Fortran code named WAKEFARM. It simulates the wake properties of a single turbine or a row of turbines. It is based on UPMWAKE, developed at Universidad Polytechnica de Madrid [18, 19]. WAKEFARM solves Reynolds averaged Navier Stokes equations in perturbation form. The Reynolds averaged Navier Stokes equations used in WAKEFARM are parabolized in the streamwise direction. The two momentum equations in transverse directions are elliptic and are solved iteratively. The axial pressure in the axial momentum equation is neglected in the far wake and prescribed along with the body force, in the near wake. An inviscid vortex ring model is used to simulate the wake. The model approximates the wind turbine rotor as an actuator disc and the wake as vortex rings. The pressure field is calculated from Bernoulli's equation and the axial pressure gradient is calculated numerically using finite differences. The induced velocity vectors calculated from the vortex model are given as initial guesses to the perturbation variables in the three momentum equations. With the help of a good initial guess for perturbation and a good estimate for the pressure gradient field, WAKEFARM is able to simulate the wake of a single wind turbine in a few minutes.

1.1 Scope of thesis

When WAKEFARM results are compared with experimental data, a discrepancy is seen. The velocity deficit measured in EWTW measurements are higher compared to the velocity deficit predicted by WAKEFARM. Underestimation of the velocity deficit will lead to power output being overpredicted. The measured velocity profile shows a small hump near the centre of the wake, indicating the presence of root vortex. The existing vortex model in WAKEFARM assumes that hub radius and root radius is zero, and doesn't model the root vortex. Hence the current WAKEFARM model doesn't capture the effect of root vortex. The modelling of flow near the root section is essential as it influences the evolution of the wake near and far from the rotor. Any improvement made to the vortex model will improve the initial guess for velocity perturbation and the axial pressure gradient. In this thesis work, two vortex

models that predict the pressure gradient field better are developed.

- A model of a wind turbine rotor with more than 3 blades with span varying circulation and constant axial induction along the span.
  The blade is approximated as a lifting line. The circulation varies along the span, hence vortices are trailed from several locations in the lifting line, forming a helical sheet. The control points are selected as midpoints of the lifting line. The lifting line and the helical trailed vortices are discretized into straight vortex filaments. After calculating the influence matrix, boundary conditions are applied on the control points. The velocity at the control points calculated using actuator disc theory is used as a boundary condition. The axial induction factor at the rotor is specified. To get closer to the Actuator disc solution of a wind turbine, the number of blades is assumed to be greater than 3. With the calculated bound vortex strength, the induced velocity field and the axial pressure gradient field in the entire wake region is calculated. Root vortex is included by specifying a non zero root radius.

- A model of a real wind turbine having 3 blades with span varying circulation and axial induction distributed along the span
  An iterative process is followed in the second method, where the bound circulation is calculated iteratively by equating the lift force from Kutta Jukowsky theorem with the lift force calculated from local flow at the blade section. A three-bladed wind turbine is simulated. The aerodynamic properties such as chord distribution, twist distribution, aerofoils, are taken from existing wind turbine blade. Root vortex is included in the model. Later the induced velocity field and the axial pressure gradient field are calculated.

1.2 Research methodology

This thesis focuses on the aerodynamics of wind turbine wakes. The objective of thesis is to understand and improve the wake modelling in WAKEFARM numerical solver. The research was conducted in the following manner,

- Learning the basics of numerical vortex methods, Navier Stokes solvers and turbulence modelling. Reviewing the literature on helical wake models.

- Learning WAKEFARM source code and theory behind it.

- Developing constant axial induction, varying circulation model of wind turbine, based on inviscid vortex methods. Conducting a parameter sweep to test the reliability of the model.

- Including root vortex effects in the model.

- Developing a model of real rotor with 3 blades, with varying axial induction and varying circulation along blades.

- Implementing the two new models in the WAKEFARM numerical solver.

- Validating the horizontal velocity profiles from WAKEFARM with measurements. Comparing the velocity profiles predicted by the new models with the existing near wake models.

- Comparing the horizontal velocity profiles predicted by the constant axial induction model and varying axial induction model, to find out the best one.

1.3   Report organization

The outline of the report is as follows:

- **Chapter 2** describes the theory behind WAKEFARM code.

- **Chapter 3** explains about the existing vortex models which are used to evaluate the axial pressure gradient and induced velocities. The development of constant axial induction rotor model and the results obtained from the model are discussed in detail.

- **Chapter 4** discusses the varying axial induction model developed, and the results obtained from the model.

- **Chapter 5** then discusses the validation of the new near wake model in WAKE-FARM with velocity measurements in EWTW test site and wind tunnel experiments done in Marchwood boundary layer laboratories.

- **Chapter 6** concludes this work and provides recommendations for further study.

<div align="right">

Chapter 2

</div>

WAKEFARM model description

A wind turbine that operates in the wake of another turbine produces a lower energy yield because of the lower wind speeds in the wake. Having a good numerical model is necessary because of the following reasons

- It can help assess the wind farm power yield during the design process, help us optimize the wind farm layout.

- It helps us study the effect of wind farms on local weather, the effect of extreme weather conditions like gusts on wind farms etc

Need for fast numerical solvers

A simulation of a wind farm where the flow is completely resolved everywhere, in CFD takes an enormous amount of computational time. This is because CFD requires that the entire flow field in the wind farm with all the turbines be modelled simultaneously. A typical numerical simulation of wind farm includes cases with 25 wind speed levels and 72 wind directions. In order for a numerical model to give reliable results for different types of cases with different boundary conditions, it needs to model, or at least describe, the physics of the problem in an adequate way. Hence numerical solvers which model the flow field in wind farm make reasonable simplifications to obtain a faster numerical result.

Introduction to WAKEFARM

ECN's wake model is implemented into a Fortran code named WAKEFARM. It simulates wake properties for a single turbine or a row of turbines. It is based on UPMWAKE, developed at Universidad Polytechnica de Madrid by Crespo et.al. [19, 18]. UPMWAKE solves the steady parabolized RANS equation in perturbation form. Many improvements were made to the UPMWAKE model at ECN. WAKEFARM is the engine of FARMFLOW, a delphi code developed in ECN. FARMFLOW can

<div align="center">

5

</div>

compute the energy yield of the entire wind farm and the loads of wind turbines in wind farm. It can also calculate the aerodynamic interactions between several wind farms. [20]. Hence an improvement in WAKEFARM is an improvement to FARMFLOW[20, 21].

In WAKEFARM wake model, the wind turbine is immersed in the atmospheric boundary layer. The flow field is perturbed by the wind turbine. The flow field is divided into two regions, near-wake and far-wake. The near wake of wind turbine extends approximately 2-3 rotor diameters (D) downstream of the turbine. The near wake region has strong pressure gradients and feels the presence of wind turbine. After near wake, the flow transitions to far wake. In the far wake, turbulence in the atmosphere plays a vital role. The turbulence in the atmosphere reduces the wake deficit and helps in the recovery of wake. The different regions in wake of a wind turbine are shown in Fig 2.1.

In WAKEFARM, the near wake region is modelled using an inviscid vortex method. The effects of turbulence in the atmosphere are added using (parabolized) Navier-Stokes equations together with the $k\varepsilon$ turbulence model. While simulating multiple turbines in a row, the output of the first turbine is given as input to the next wind turbine.
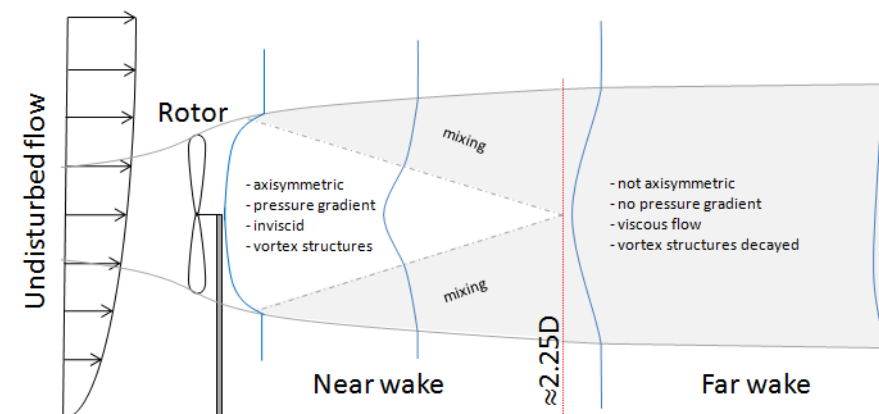
Figure 2.1: Different regions in the wake of a wind turbine

2.1 Coordinate system

WAKEFARM uses cartesian coordinates. The x- coordinate is taken along the wake direction, the y-coordinate is along the span of blade and z- coordinate is in the direction of increasing height.

WAKEFARM has four main components:

- Parabolized Navier Stokes and $k - \epsilon$ model

Figure 2.2: Coordinate system used in WAKEFARM

- Rotor model

- Free stream model/ Undisturbed flow model

- Near wake model

2.2 Governing equations

In this section, the Governing equations of WAKEFARM are described. WAKEFARM solves steady RANS equations in perturbation form. The RANS equation for turbulent flows reads,

$$\frac{\partial \overline{U_i}}{\partial x_i} = 0, \tag{2.1}$$

$$\frac{\partial (\overline{U_i}\,\overline{U_j})}{\partial x_j} = -\frac{1}{\rho}\frac{\partial \overline{p}}{\partial x_i} - \frac{\partial \tau_{ij}^R}{\partial x_j} + f, \tag{2.2}$$

where τ_{ij}^R is the Reynolds stress, given by.

$$\tau_{ij}^R = \frac{\partial (\overline{U_i' U_j'})}{\partial x_j} \tag{2.3}$$

2.2.1 Perturbed Navier Stokes equations

The mean flow $\overline{U_i}$ is linearized as a sum of undisturbed flow and perturbation. This perturbation u shouldn't be confused with turbulent fluctuation u'. The former is

caused by the wind turbine (velocity deficit). The undisturbed flow variables (denoted with subscript '0') are obtained from the ABL model described in section 2.4.

$$\overline{U} = u_0 + u \qquad \nu_t^* = \nu_{t0} + \nu_t \qquad k^* = k_0 + k, \qquad \nu_\theta^* = \nu_{\theta 0} + \nu_\theta, \qquad \varepsilon^* = \varepsilon_0 + \varepsilon. \quad (2.4)$$

Parabolizing Navier Stokes equations

The simplification of Navier-Stokes equations by parabolizing the momentum and energy equation is done in most wind farm codes. All the elliptic terms in the stream wise direction are neglected, therefore the Navier Stokes equations in $x-$direction together with energy equation become parabolic in the axial direction. This means that the information travels only downstream and only information upstream is needed for the calculation. A space marching procedure can be used instead of solving the whole grid [3]. The momentum equations in the $y-$ and in the $z-$direction are elliptic and they have to be solved iteratively in each $x-$plane.

Analogy with boundary layer equations

In the boundary layer equatons, the axial pressure gradient is prescribed. It is calculated using the flow at the edge of the boundary layer. In WAKEFARM, the the axial pressure gradient calculated from the near wake model (inviscid vortex model) is used as a source term in axial momentum equation. The near wake model is based on inviscid vortex theory. The existing vortex models are discussed in the next chapter 3. The axial pressure gradient thus is not calculated at each spatial step. The assumptions used in the equations are given below [3].

Assumptions

- The flow is steady.

- The flow is incompressible.

- The flow is dominant in the axial direction and there is no flow reversal.

- The velocity in the dominant flow direction is higher compared to the velocity components in other two directions. Hence they are neglected.

- The axial pressure gradient is neglected in the far wake. In near wake, the streamwise pressure gradient is prescribed along with the body force.

- The viscous stresses are negligible compared to Reynolds stress. The molecular heat transport is negligible compared to turbulent heat transport.

- The diffusion in streamwise direction is neglected. $\frac{\partial \tau_{ij}^R}{\partial x_i} = 0$.

- The turbulent heat conduction in stream-wise direction is neglected.

- The undisturbed flow in $y-$ and $z-$directions are neglected: $v_0 = 0$, $w_0 = 0$.

- The change in magnitude of v and w in $y-$ and $z-$directions are small,The first and second derivatives in two directions can be neglected. $\frac{\partial^2 w}{\partial y \partial z} = 0$.

Based on experimental observations, Boussinessq proposed that deviatoric Reynolds stress τ_{ij}^R is proportional to the mean rate of strain, Now equation for Reynolds stress, τ_{ij}^R can be rewritten in perturbation form as follows,

$$\tau_{ij}^R = \rho \left(\nu_{t0} + \nu_t \right) \left(\frac{\partial \left(u_i + u_{i0} \right)}{\partial x_j} + \frac{\partial \left(u_j + u_{j0} \right)}{\partial x_i} \right) - \frac{2}{3} \delta_{ij} \left(k + k_0 \right), \qquad (2.5)$$

where ν_t-kinematic turbulent (eddy) viscosity. It is not a material property and depends on flow properties. ν_{t0} is the eddy viscosity associated with undisturbed flow. k, turbulent kinetic energy per unit mass is defined as,

$$k = \frac{\left(\overline{u'}^2 + \overline{v'}^2 + \overline{w'}^2 \right)}{2} \qquad (2.6)$$

k_0 is the turbulent kinetic energy present in the undisturbed flow. Expressions 2.37 is used to evaluate the turbulent kinetic energy per unit mass in the undisturbed flow. u', v', w' are the turbulent fluctuations in the velocity in the three directions. The main purpose of velocity fluctuation of turbulence is to enhance the shear stress. The perturbed equations are given by

Continuity:

$$\frac{\partial u}{\partial x} + \frac{\partial v}{\partial y} + \frac{\partial w}{\partial z} = 0 \qquad (2.7)$$

x-momentum equation

$$(u + u_0) \frac{\partial u}{\partial x} + v \frac{\partial u}{\partial y} + w \frac{\partial u}{\partial z} = \frac{\partial \nu_t}{\partial y} \frac{\partial u}{\partial y} + (\nu_t + \nu_{t0}) \frac{\partial^2 u}{\partial y^2} + \left(\frac{\partial \nu_t}{\partial z} + \frac{\partial \nu_{t0}}{\partial z} \right) \frac{\partial u}{\partial z} + \frac{\partial \nu_t}{\partial z} \frac{\partial u_0}{\partial z}$$
$$+ (\nu_t + \nu_{t0}) \frac{\partial^2 u}{\partial z^2} + \nu_t \frac{\partial u_0}{\partial z} + f. \qquad (2.8)$$

the term f in $x-$momentum equation is the axial pressure gradient calculated from the near wake model. The near wake model is explained in the next chapter.

$$f = -\frac{1}{\rho} \frac{\partial p}{\partial x} \qquad (2.9)$$

y-momentum equation

$$(u + u_0)\frac{\partial v}{\partial x} + v\frac{\partial v}{\partial y} + w\frac{\partial v}{\partial z} = -\frac{1}{\rho}\frac{\partial p}{\partial y} + 2\frac{\partial \nu_t}{\partial y}\frac{\partial v}{\partial y} + 2(\nu_t + \nu_{t0})\frac{\partial^2 v}{\partial y^2} + \left(\frac{\partial \nu_t}{\partial z} + \frac{\partial \nu_{t0}}{\partial z}\right)\frac{\partial v}{\partial z}$$
$$+ (\nu_t + \nu_{t0})\frac{\partial^2 v^2}{\partial z} + \left(\frac{\partial \nu_t}{\partial z} + \frac{\partial \nu_{t0}}{\partial z}\right)\frac{\partial w}{\partial y} - \frac{2}{3}\frac{\partial}{\partial y}(k + k_0), \text{(2.10)}$$

z-momentum equation

$$(u + u_0)\frac{\partial w}{\partial x} + v\frac{\partial w}{\partial y} + w\frac{\partial w}{\partial z} = -\frac{1}{\rho}\frac{\partial p}{\partial z} + \frac{\partial \nu_t}{\partial y}\frac{\partial w}{\partial y} + (\nu_t + \nu_{t0})\frac{\partial^2 w}{\partial y^2} + 2\left(\frac{\partial \nu_t}{\partial z} + \frac{\partial \nu_{t0}}{\partial z}\right)\frac{\partial w}{\partial z}$$
$$+ 2(\nu_t + \nu_{t0})\frac{\partial^2 w}{\partial z^2} + \frac{\partial \nu_t}{\partial y}\frac{\partial w}{\partial z} - \frac{2}{3}\frac{\partial}{\partial z}(k + k_0) + \beta g\theta. \quad \text{(2.11)}$$

A complete derivation of the perturbed Navier-Stokes equations can be found in [3]. Kinematic turbulent viscosity, ν_t can be expressed as a product of a velocity scale and a length scale.

$$\nu_t = C_\mu v l \tag{2.12}$$

Two equations ($k - \varepsilon$) are used to model the eddy viscosity term. Using k and ε, the velocity and length scales are defined as follows,

$$v = \sqrt{k} \tag{2.13}$$

$$l = \frac{k^{\frac{3}{2}}}{\varepsilon} \tag{2.14}$$

Equations 2.17 and 2.18 are used to predict k and ε.

Energy equation

The energy equation is used to model the buoyancy term in the momentum equations. The potential temperature is linearized as a sum of potential temperature of the undisturbed flwo and perturbation.

$$(u + u_0)\frac{\partial \theta}{\partial x} + v\frac{\partial \theta}{\partial y} + w\frac{\partial \theta}{\partial z} = \frac{\partial}{\partial y}\left((\nu_\theta + \nu_{\theta_0})\frac{\partial(\theta + \theta_0)}{\partial y}\right) + \frac{\partial}{\partial z}\left((\nu_\theta + \nu_{\theta_0})\frac{\partial(\theta + \theta_0)}{\partial z}\right) \text{(2.15)}$$

which leads to

$$(u + u_0)\frac{\partial \theta}{\partial x} + v\frac{\partial \theta}{\partial y} + w\frac{\partial \theta}{\partial z} = \frac{\partial \nu_\theta}{\partial y}\frac{\partial \theta}{\partial y} + (\nu_\theta + \nu_{\theta_0})\frac{\partial^2 \theta}{\partial y^2} + \left(\frac{\partial \nu_\theta}{\partial z} + \frac{\partial \nu_{\theta_0}}{\partial z}\right)\frac{\partial \theta}{\partial z}$$
$$+ (\nu_\theta + \nu_{\theta_0})\frac{\partial^2 \theta}{\partial z^2} + \frac{\partial \nu_{\theta_0}}{\partial z}\frac{\partial \theta}{\partial z} + \nu_{\theta_0}\frac{\partial^2 \theta_0}{\partial z}. \quad \text{(2.16)}$$

Perturbed $k - \varepsilon$ turbulence model

The $k - \varepsilon$ turbulence is used for the closure of momentum equations. It has 2 equations [22, 23, 24],

- Equation for turbulent kinetic energy per unit mass-k

- Equation for the rate of dissipation of turbulent kinetic energy per unit mass ε

Equation 2.17 calculates the energy in turbulence and Equation 2.18 calculates the scale of turbulence. Turbulent kinetic energy:

$$(u + u_0) \frac{\partial k}{\partial x} + v \frac{\partial k}{\partial y} + w \frac{\partial (k_0 + k)}{\partial z} = (\nu_k + \nu_{k_0}) \frac{\partial^2 k}{\partial y^2} + (\nu_k + \nu_{k_0}) \frac{\partial^2 k}{\partial z^2} + \frac{\partial \nu_k}{\partial y} \frac{\partial k}{\partial y} + (\nu_k) \frac{\partial^2 k_0}{\partial z^2}$$

$$+ (\nu_t + \nu_{t_0}) \left[\left(\frac{\partial u}{\partial y} \right)^2 + \left(\frac{\partial u}{\partial z} \right)^2 + 2 \frac{\partial u}{\partial z} \frac{\partial u_0}{\partial z} \right] + \nu_t \left(\frac{\partial u_0}{\partial z} \right)^2 - \beta g \nu_\theta \left(\frac{\partial \theta}{\partial z} + \frac{\partial \theta_0}{\partial z} \right) - \beta g \nu_\theta \frac{\partial \theta}{\partial z}$$

$$(2.17)$$

Dissipation rate of the turbulent kinetic energy:

$$(u + u_0) \frac{\partial \varepsilon}{\partial x} + v \frac{\partial \varepsilon}{\partial y} + w \frac{\partial (\varepsilon_0 + \varepsilon)}{\partial z} = (\nu_\varepsilon + \nu_{\varepsilon_0}) \frac{\partial^2 \varepsilon}{\partial y^2} + (\nu_k + \nu_{k_0}) \frac{\partial^2 \varepsilon}{\partial z^2} + \frac{\partial \nu_\varepsilon}{\partial y} \frac{\partial \varepsilon}{\partial y} + (\nu_\varepsilon) \frac{\partial^2 \varepsilon_0}{\partial z^2}$$

$$+ \left(\frac{\partial \nu_\varepsilon}{\partial z} + \frac{\partial \nu_{\varepsilon_0}}{\partial z} \right) \frac{\partial \varepsilon}{\partial z} + \frac{\partial \nu_\varepsilon}{\partial z} \frac{\partial \varepsilon_0}{\partial z} + \nu_\varepsilon \frac{\partial^2 \varepsilon_0}{\partial z^2} + C_{\varepsilon 1} \frac{\varepsilon_0 + \varepsilon}{k_0 + k} (\nu_t + \nu_{t0}) \left[\left(\frac{\partial u}{\partial y} \right)^2 + \left(\frac{\partial u}{\partial z} \right)^2 + \left(\frac{\partial u_0}{\partial y} \right)^2 \right]$$

$$+ 2 \frac{\partial u}{\partial z} \frac{\partial u_0}{\partial z} + (1 - C_{\varepsilon 3}) \beta g \frac{1}{\sigma_\theta} \frac{\partial (\theta + \theta_0)}{\partial z} + C_{\varepsilon 1} \frac{\varepsilon_0}{k_0} \nu_{t0} \left[\left(\frac{\partial u_0}{\partial z} \right)^2 - (1 - C_{\varepsilon 3}) \beta g \frac{1}{\sigma_\theta} \frac{\partial \theta_0}{\partial z} \right]$$

$$- C_{\varepsilon 2} \frac{(\varepsilon_0 + \varepsilon)^2}{k_0 + k} + C_{\varepsilon 2} \frac{\varepsilon_0^2}{k_0} \qquad (2.18)$$

The closure coefficients are,

$$C_\mu = 0.033, C_{\epsilon 1} = 1.21, C_{\epsilon 2} = 1.92, C_{\epsilon 3} = 0.8, \sigma_\theta = \sigma_k = 1.0, \sigma_\epsilon = 1.3 \qquad (2.19)$$

2.3 Rotor model

In the existing WAKEFARM model, the wind turbine rotor is modelled using actuator disk theory. The wind turbine is treated as an actuator disc (infinite number of blades). There is a pressure jump at the actuator disk. The velocity far upstream is

U_∞, far downstream is U_e, and at the rotor disc, it is taken as U_R. The velocity at the rotor according to actuator disk momentum theory is defined as follows,

$$U_R = \frac{1}{2}(U_\infty + U_e) \tag{2.20}$$

2.3.1 Induction factor and thrust coefficient

A non-dimensional quantity called induction factor is defined as follows,

$$a = \frac{U_\infty - U_R}{U_\infty} \tag{2.21}$$

The velocity at the rotor disc and far downstream is defined as follows,

$$U_R = U_\infty(1 - a) \tag{2.22}$$

$$U_e = U_\infty(1 - 2a) \tag{2.23}$$

The thrust coefficient is defines as follows,

$$C_T = \frac{T}{\frac{1}{2}\rho U_\infty^2} = 4a(1 - a) \tag{2.24}$$

For heavily loaded rotors, Glauert included a correction. The Glauert correction
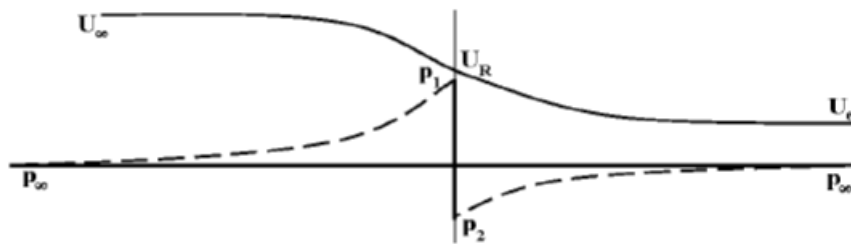
Figure 2.3: Pressure and Velocity distributions in actuator disk model

reads as follows,

$$\phi_m = \begin{cases} \frac{1}{2}\left(1 - \sqrt{1 - 0.8}\right), & \text{if } a > 1.4 \\ \frac{1}{2}(-2.5(C_T - 0.8)^2 + C_T + 0.2 - \sqrt{1 - 0.8}), & \text{if } 0.8 < a < 1.4 \\ \frac{1}{2}\left(1 - \sqrt{1 - C_T}\right), & \text{if } 0 < a < 0.8 \end{cases} \tag{2.25}$$

2.4 Undisturbed flow model - Atmospheric boundary layer stability model

The undisturbed flow here is referred to as the flow far upstream of the wind turbine. This mainly consists of the atmospheric boundary layer (ABL) above the surface of earth. The Atmospheric boundary layer in WAKEFARM is modelled using two different empirical models suggested by Panofsky-Dutton [25] and Gryning[26].

2.4.1 Panofsky Dutton ABL model

Panofsky model uses a surface layer model to model the atmospheric boundary layer. The surface layer is the lower 10% part of the atmospheric boundary layer, where the magnitude of wind speed changes. The direction of wind is more or less constant.

Velocity profile

The undisturbed mean flow $'u'_o$ and turbulent statistics is to be modelled. The undisturbed flow is assumed to vary in z-direction only. The Reynolds number in the stream-wise direction is very high, hence stream-wise diffusion is neglected. The molecular viscous stresses are small compared to the Reynolds stress term $\overline{u'w'}$. By Boussinessq approximation the Reynolds stress is defined as follows,

$$\tau^R = \overline{u'w'} = \rho \nu_{t0} \frac{\partial u_0}{\partial z} \tag{2.26}$$

where ν_{t0} is eddy viscosity or turbulent viscosity, u_0 undisturbed mean flow, u_* friction velocity, the characteristic velocity at the wall is expressed as follows[25]

$$u_* = \sqrt{\frac{\tau^R}{\rho}} \tag{2.27}$$

leading to

$$\frac{\partial u_0}{\partial z} = \frac{u_*^2}{\nu_{t0}} \tag{2.28}$$

Monin and Obukhov in their similarity theory [27] calculated eddy viscosity ν_{t0} as follows,

$$\nu_{t0} = \frac{k u_* z}{\phi_m(\frac{z}{L})} \tag{2.29}$$

where von Karman constant, k, taken as 0.4 in [18], ϕ_m Monin Obukhov function, L Monin Obukhov length, discussed in C.0.1. Substituting equation 2.28 in equation

2.29,

$$\frac{\partial u_0}{\partial z} = \frac{u_*}{kz}\phi_m\left(\frac{z}{L}\right) \tag{2.30}$$

Both sides of equation (2.30) are integrated from z_0 to z, to obtain the velocity profile.

$$\int_{z_0}^{z} \frac{\partial u_0}{\partial z} dz = \int_{z_0}^{z} \frac{u_*}{kz}\phi_m\left(\frac{z}{L}\right) dz = \frac{u_*}{k}\int_{z_0}^{z}\left(1-\left[1-\phi_m\left(\frac{z}{L}\right)\right]\right)\frac{dz}{z} \tag{2.31}$$

leading to,

$$u_0(z) = \frac{u_*}{k}\left[ln\left(\frac{z}{z_0} - \Psi_m(\xi)\right)\right] \tag{2.32}$$

where $\xi = \frac{z}{L}$, together with,

$$\Psi_m(\xi) = \int_0^{\xi}(1-\phi_m(\xi))\frac{d\xi}{\xi} \tag{2.33}$$

Ψ_m is stability correction function discussed in C.3. The value of the function varies as the stability of the atmosphere varies (see section C.0.1) to learn about stability classification.

Potential temperature profile

Similar to the velocity profile, potential temperature profile can be derived

$$\theta_0 - \theta_{0s} = \frac{T_*}{k}\left[ln\left(\frac{z}{z_0}\right) - \Psi_h(\xi)\right], \tag{2.34}$$

$$\Psi_h(\xi) = \int_0^{\xi}\left(1 - \frac{\nu_{\theta 0}}{\nu_{t0}}\phi_m(\xi)\right)\frac{d\xi}{\xi} \tag{2.35}$$

where,

$$T_* = \frac{Q}{\rho C_p u_*} \tag{2.36}$$

with, $\nu_{\theta 0}$ is the thermal diffusivity of heat, θ_{0s} is the potential temperature of the ground, Q is the turbulent heat flux to the ground. Ψ_h is stability correction function discussed in section C.3.

Profile of k_0 and ϵ_0

The expression for the profile of turbulent kinetic energy in ambient flow as given in [18], is as follows

$$k_0(z) = \frac{u_*^2}{\sqrt{C_\mu}}\Psi_k(\xi) \tag{2.37}$$

where C_μ is a constant used in $k - \varepsilon$ model and is set as 0.033. Similarly the expression for dissipation rate of turbulent kinetic energy in ambient flow ε_0 used in WAKEFARM is given below,

$$\varepsilon_0(z) = \frac{3u_*}{kz}\Psi_e(\xi) \tag{2.38}$$

$\Psi_e(\xi)$ and $\Psi_k(\xi)$ are stability correction functions discussed in section C.3

2.4.2 Gryning ABL model

Gryning [1] mentions that the height of surface layer is in the order of $50 - 80m$. The wind turbines have grown in size. Haliade-X which is the world's powerful offshore wind turbine to date (July 2018), has a total height of $260m$. The upper part of wind turbine lies outside the surface layer[28]. Sathe et.al. [28] showed that by using the surface layer profile in higher heights, the loads are predicted much larger compared with those obtained using a boundary layer wind profile (which includes an accurate description of above surface layer profiles) [28]. Hence the assumption that the whole of wind turbine lies in the surface layer is not reliable. The wind profile length l scale consists of 3 terms, surface layer length scale L_{SL}, length scale in the middle of boundary layer L_{MBL}, length scale in the upper boundary layer L_{UBL}.

$$\frac{1}{l} = \frac{1}{L_{SL}} + \frac{1}{L_{MBL}} + \frac{1}{L_{UBL}} \tag{2.39}$$

Figure 2.4 illustrates the behaviour of the 3 length scales for a neutral boundary layer of height $1000m$. The surface layer where the length scale varies linearly with height is applicable only up to $50m$. After $50m$, the influence of L_{MBL} can be seen. The height of the boundary layer L_{UBL} influences the length scale at $150m$. The different types of atmospheric stability are discussed in section C.0.1.

Velocity profile

A detailed derivation of velocity profile is given in [26]. The velocity profile is given by,

Neutral conditions

$$u_0(z) = \frac{u_*}{k}\left(ln\left(\frac{z}{z_0}\right) + \frac{z}{L_{MBL}} - \frac{z}{z_i}\left(\frac{z}{2L_{MBL}}\right)\right) \tag{2.40}$$

Stable conditions

The profile of u_0 for stable conditions reads[1],

$$u_0(z) = \frac{u_*}{k}\left(ln\left(\frac{z}{z_0}\right) + \frac{5z}{L}\left(1 - \frac{z}{2z_i}\right) + \frac{z}{L_{MBL}} - \frac{z}{z_i}\left(\frac{z}{2L_{MBL}}\right)\right) \qquad (2.41)$$

Unstable conditions

For unstable atmospheric conditions, the undisturbed wind profile can be expressed as,

$$u_0(z) = \frac{u_*}{k}\left(ln\left(\frac{z}{z_0}\right) - \Psi_m(\xi) + \frac{z}{L_{MBL}} - \frac{z}{z_i}\left(\frac{z}{2L_{MBL}}\right)\right) \qquad (2.42)$$
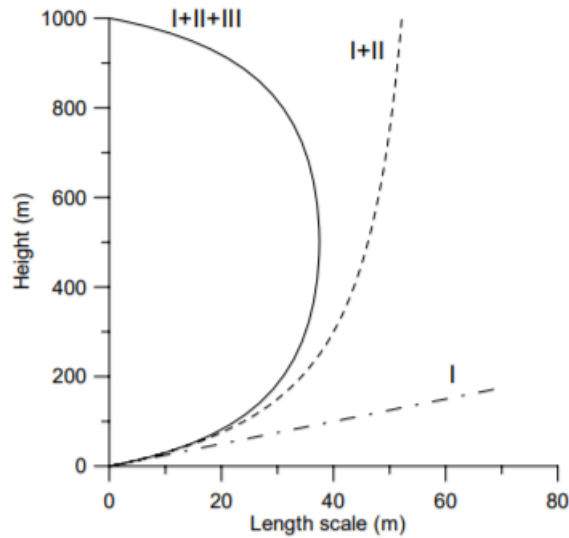
Figure 2.4: Profiles of the length scale for neutral conditions with boundary layer height of $1000m$ and roughness length $z_0 = 0.05m$ The dashed-dotted line correlates to the surface layer scaling. The dashed line includes the effect of first two terms and the full line includes the effect of all three terms in the formulation of the length scale [1].

The stability correction function $\Psi_m(\xi)$ is obtained from equation C.9. In all the equations above, L represents the Monin-Obukhov length, L_{MBL}, the length of middle boundary layer z_i, the total height of the boundary layer, u_*, the friction velocity near the ground surface, z, vertical position

The last two terms in equation (2.40), equation (2.41), equation (2.42) are the corrections terms included, to add the effect of length scales L_{MBL} and L_{UBL}

Table 2.1: Stability classification based on Monin-Obukhov length(L)

$10 < L < 50$	Very Stable
$50 < L < 200$	Stable
$200 < L < 500$	near neutral/stable
$L > 500, L < -500$	neutral
$-500 < L < -200$	near neutral/unstable
$-200 < L < -100$	unstable
$100 < L < -50$	very unstable

Parameterization of L_{MBL}

The length of middle boundary layer L_{MBL} is calculated from the following expression

$$\frac{u_*}{fL_{MBL}} = \left(-2ln\left(\frac{u_*}{fz_0} + 55\right)exp\left(-\frac{\left(\frac{u_*}{fL}\right)^2}{400}\right)\right) \tag{2.43}$$

The above expression is derived by relating the wind speed at the top of the boundary layer to the friction velocity u_* near the ground [1]. By knowing u_*, L, z_0 and Coriolis force f, L_{MBL} can be derived. The height of the boundary layer is approximated as

$$z_i \equiv 0.1\frac{u_*}{f} \tag{2.44}$$

The profile of potential temperature θ_0, k_0, ε_0 are calculated with expressions in section 2.4.1. The stability classification is given in the table 2.1 [1].

2.5 Grid generation

WAKEFARM uses a stretched grid in the $x-$direction and an uniform grid in $y-$ and $z-$directions. The grid is stretched until $0.5D$, and from then on the grid is uniform. A finer grid is used close to the rotor, where sharp gradients are present. The domain extends to $7.5D$ in $x-$direction, $3.8D$ in $y-$ and $z-$directions.

2.6 Numerical methods

Due to the parabolic nature of the $x-$momentum equation, it can be solved by marching in stream-wise direction. The governing equations described in the previous section are discretized with finite difference scheme on a rectangular grid. The SIMPLE method (Semi Implicit Method for Pressure Linked Equations) is used to
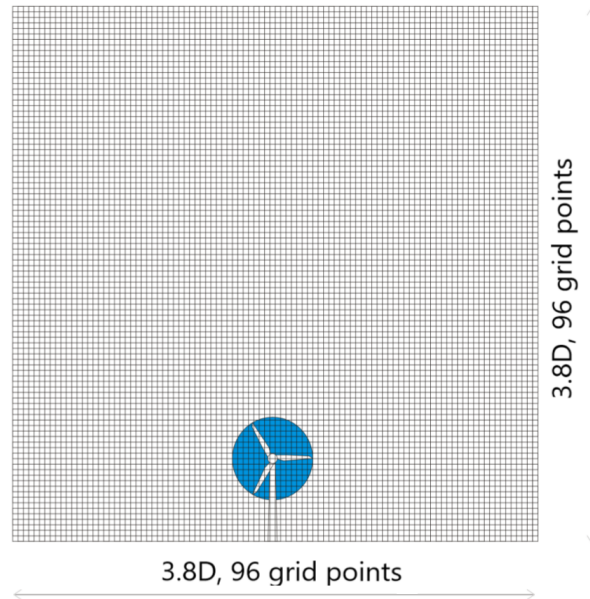
Figure 2.5: Computational domain in $y - z$ plane in WAKEFARM [2]

calculate the pressure gradients in y and z directions. (see section 2.6.2) and ADI method (Alternating Direction Implicit scheme (section 2.6.1)). The idea behind using ADI methods is to obtain a tridiagonal system which is easier to solve. In ADI method, computational domain is swept one line at a time. To obtain a tridiagonal system, the governing equations in WAKEFARM equations 2.8 -2.18 are rewritten in a new way. The elements outside three diagonals are moved to the right-hand side of the equation. Their values are assumed to be known. The process is repeated till convergence [29] In a row-wise sweep, the information propagates instantaneously from left to right boundary. However, the information does not propagate efficiently in the other direction. To circumvent this checkerboard problem, the direction of the line wise sweeps is alternated. Hence the name alternating direct implicit method [29]. The resulting tridiagonal system is solved by using Thomas algorithm. While solving the momentum equations in an iterative way, non-uniform pressure field or oscillatory pressure fields may occur in the intermediate steps. Central differences might not be able to capture such a non uniform pressure field. Upwind schemes could be used, but they have a disadvantage that the information travels only from one direction. To avoid these issues, a staggered grid is used for pressure (see Figure 2.7) [3]. The velocities are calculated in the main grid points (solid points in Figure2.7) and the pressure is calculated in the staggered grid points (crosses in Figure2.7). While deriving the pressure correction formula for the SIMPLE algorithm, the continuity equation is written on the staggered grid. The derivation of the pressure correction formula can be seen in [3].

The convective terms are modelled by upwind schemes [3] and the remaining

terms are modelled by central differences.

2.6.1 ADI method

The variable $\Phi_{i,j}$ denotes the flow variables in WAKEFARM $(u, v, w, p, t, k, \varepsilon)$. All the 7 governing equations in WAKEFARM are solved using ADI method. The ADI method is summarized below.

- Start with an initial guess $\Phi_{i,j}$

- Set up a tridiagonal solver for each row (e.g. row wise sweep). This can be treated as an intermediate step (step at $n + \frac{1}{2}$).

- Set up a tridiagonal solver for each column (e.g.column-wise sweep). The updated solution from the row wise sweep is used as an initial guess to the column-wise sweep (n+1 step).

- Iterate till convergence

$$a_i \Phi_{i+1,j} + b_i \Phi_{i,j} + c_{j-1,i} = d \qquad (2.45)$$

where, d is the known value (value at the current iteration) of the entries outside the tridiagonal system. The following set of equations are obtained.

$$\begin{bmatrix} a_{i \to nz} & b_{i \to nz} & c_{i \to nz} \end{bmatrix} \begin{bmatrix} \Phi_{i \to nz} \end{bmatrix} = \begin{bmatrix} d_{i \to nz} \end{bmatrix} \qquad (2.46)$$
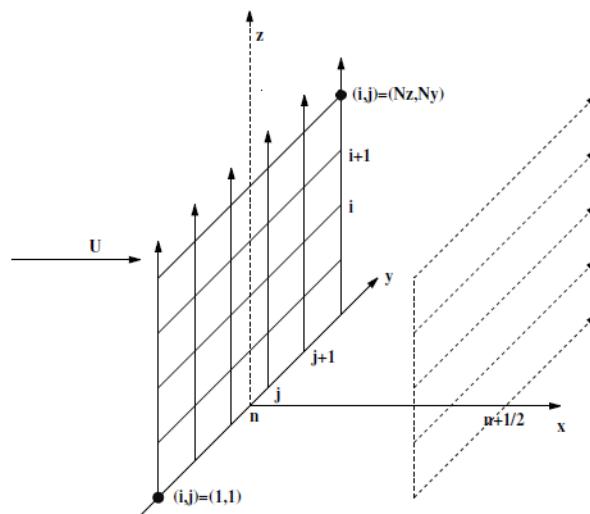
Figure 2.6: First step in ADI method

2.6.2   The SIMPLE method

The SIMPLE algorithm is summarized below,

- Calculate the velocity field for the next axial plane from the momentum equations using ADI method.

- Obtain pressure correction from the pressure correction formula.

- Perform Gauss Seidel relaxation, till the continuity equation is satisfied.

- Once the pressure is converged, the velocities are calculated from $y-$momentum and $z-$momentum equations.

- When the above mentioned steps are completed, the values of θ, k, ε are calculated for the next axial plane, using ADI method.

- Complete the space marching procedure.

A detailed description of the SIMPLE method is found in [30]
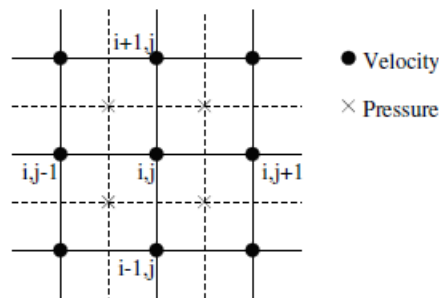
Figure 2.7: Staggered grid
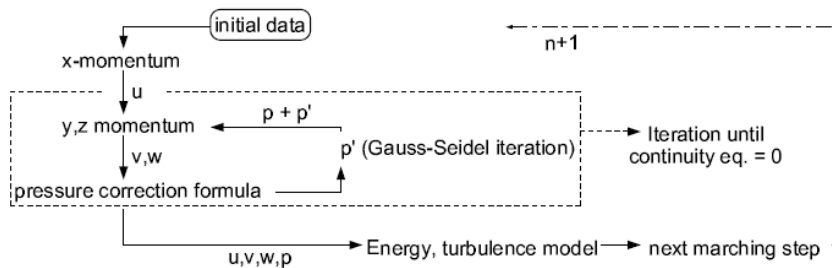
Figure 2.8: SIMPLE method [3].

2.6.3   Boundary conditions

The boundary conditions are specified at the extremities of each $y - z$ plane (see Figure 2.6) at each spatial step. On all the boundaries, the flow reaches frees stream conditions (u_0, v_0, w_0. The perturbation values at the boundaries should be zero :

$$u = v = w = p = \theta = k = \varepsilon = 0 \tag{2.47}$$

substituting this in the $y-$momentum equation we get,

$$-\frac{1}{\rho}\frac{\partial p}{\partial y} \approx 0 \tag{2.48}$$

The same exercise can be repeated to top and bottom edge of the domain using $z-$ momentum equation. The pressure at the first row of points inside normal grid should be zero. The boundary condition for pressure reads,

$$p_{j-\frac{1}{2},i-\frac{1}{2}} = 0 \, for \begin{cases} j = 1, 2, Ny, Ny + 1, i = 1, 2, ..., Nz + 1 \\ i = 1, 2, Nz, Nz + 1, j = 1, 2, ...Ny + 1 \end{cases} \tag{2.49}$$

2.7   Example WAKEFARM result

The horizontal velocity profile in the cross-flow direction at hub height and at downstream distance $2.5D$ is presented in this section. The velocity profile measured in EWTW measurements show a higher velocity deficit compared to velocity deficit predicted by WAKEFARM (see Figure 2.9). Towards the centre of the wake, the experimental velocity profile shows a small hump. This is due to the presence of root vortex in the wind turbine wake. This behaviour is not captured by WAKEFARM. The centerline velocity profile at a downstream distance of $5D$ is also presented in Figure 2.10. The velocity profile measured in Marchwood experiments have a higher velocity deficit compared to the centerline velocity profile predicted by WAKEFARM. These discrepancies could be avoided by implementing better near wake models that would predict the pressure gradient field and the velocity field better. This is discussed in the next chapter.
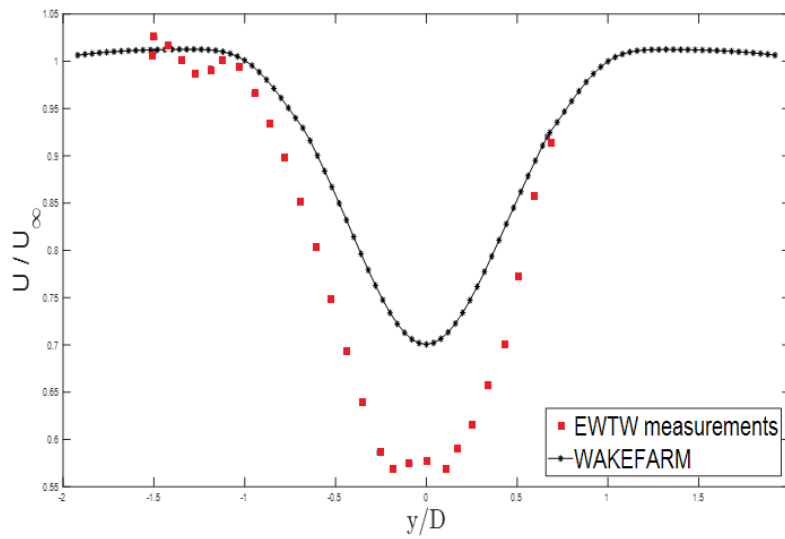
Figure 2.9: Comparison of horizontal velocity profile in the cross flow direction at hub height and at downstream distance $2.5D$ with EWTW measurements. The axial induction factor at rotor $a = 0.245$ and the free stream velocity at hub height is $11m/s$
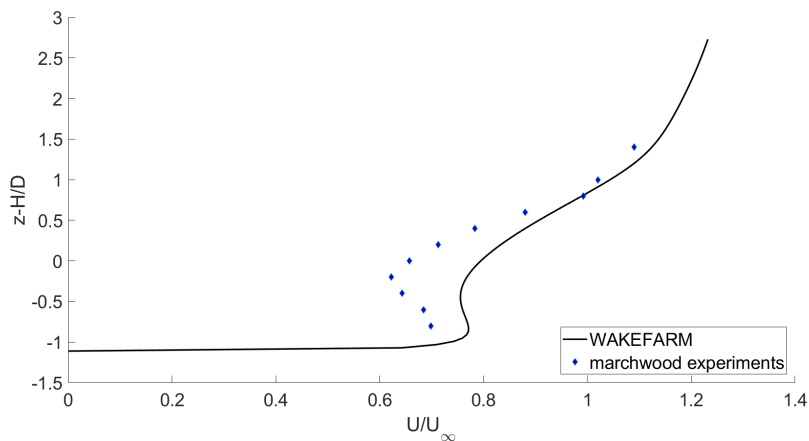
Figure 2.10: Comparison of centerline velocity profile at downstream distance of $x - 5D$ with Marchwood experimental data. The thrust coefficient at the rotor $C_t = 0.62$

Inviscid near wake model improvement

In chapter 2 it was mentioned that, in the axial momentum equation, pressure gradient was not calculated iteratively. The axial pressure gradient in far wake is neglected, as it is negligible. Earlier the near wake was not included in the numerical simulation of the fluid flow equations. The velocity profile in near wake was represented by a gaussian shaped velocity profile. The space marching was started at downstream position 2.25D. Later to reduce the dependency on tuning parameters and to model the wake in a realistic way, the wake of wind turbine was modelled using inviscid vortex methods. The pressure field is calculated using Bernoulli's equation. The pressure gradients are then calculated numerically using finite differences. The calculated axial pressure gradient is prescribed along with the body force. The induced velocities calculated in three directions are given as an initial guess to the perturbation in perturbed Navier Stokes equations (2.8-2.11). The existing vortex models used in WAKEFARM are discussed initially and later, the improvements made are discussed in detail.

3.1 Existing inviscid vortex model

3.1.1 Vortex tube model

In this model, the wind turbine is approximated as actuator disk, the wake is represented as vortex tube (see Figure 3.1). The vortex rings are discretized as straight vortex filaments. The method is free-wake method, where the wake radius is a part of the solution process. The boundary condition given is that there is no pressure jump across the tube. The free-wake method is computationally expensive. But since the flow in the wake and the resulting axial pressure gradient is only a function of the induction factor, for a set of induction factors the resulting velocity profile

scaled with rotor diameter is stored a priori in a database [4]. This database is known as **'Tube files'**.
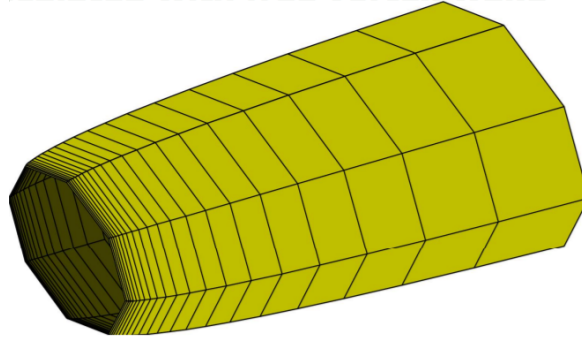
Figure 3.1: Wake represented as a vortex tube [4]

3.1.2 Oye's vortex ring model

Apart from the vortex-tube near wake model, another near-wake model exists in WAKEFARM. It is based on vortex ring model suggested by Oye [5]. Oye 's vortex model assumes wind turbine as an actuator disk (a rotor with infinite number of blades). The actuator disk has a constant loading throughout the disk and hence infinitely thin vortex rings are trailed from the edges of the disk. They describe the wake. The vortex ring wake structure expands behind the turbine forming a vortex tube of increasing radius as shown in figure 3.2. The vortex densities on the surface of the tube are resolved into axial and tangential components, as seen in Figure 3.3. The model also assumes infinite tip speed ratios, the hub radius to be zero and hence root vortex and the induced velocity contribution from the axial component of vortex density can be ignored. The velocities induced in axial and radial directions are produced by the tangential component of vortex density (see Figure 3.3). The tangential component of vortex density γ_t, is defined as follows [5],

$$\gamma_t = C_t \frac{U_\infty^2}{2V_a} \tag{3.1}$$

where U_∞ is undisturbed free stream velocity at hub height, V_a, velocity induced by tip vortices in axial direction and C_t, thrust coefficient at the rotor. Equation 3.1 is used to calculate the tangential vortex density γ_t at each iteration. A complete derivation of equation 3.1 is found in [5].

The wake is modelled by using discrete vortex rings. Each vortex ring represents a wake segment of length dx (see Figure 3.2). The vortex rings are placed in the middle of wake segment and at a distance equal to local wake radius in the $y-$direction. By knowing the vortex strength and wake radius, velocity induced by
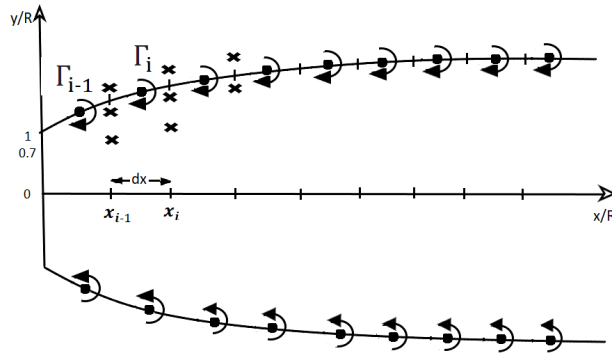
Figure 3.2: Model of wind turbine wake with discrete ring vortices
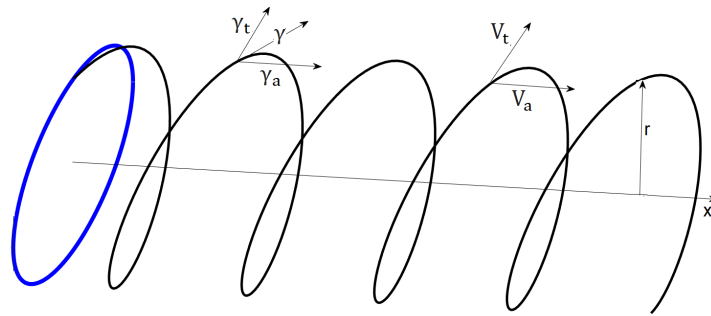
Figure 3.3: Resolving the vortex density on the surface of a single tip vortex into its axial and tangential components[5].

each vortex ring can be calculated from the analytical expression for velocity induced by a vortex ring (see equation A.1 and equation A.2). The elliptic integrals are evaluated numerically. As the vortex strength and axial induced velocity are interrelated, the system is non-linear. The wake radius is calculated from the continuity equation for axial flow, i.e. the total flow through each section of the wake is same as the flow through the rotor disc. The axial velocity at $0.7R$ is calculated at the rotor and at several downstream positions in the wake. It is assumed to be a good estimate to the average axial velocity at each cross-section in the wake. The continuity equation for axial flow is written as follows

$$\rho A_{rotor} V_{0.7}(0) = \rho A_{wake} V_{0.7}(x_i) \tag{3.2}$$

After further simplifications the following equation for wake radius r_i is obtained

$$r_i = R\sqrt{\frac{V_{0.7}(0)}{V_{0.7}(x_i)}} \tag{3.3}$$

with A$_{rotor}$ is the area of the rotor, A_{wake} is the cross sectional area at the selected downstream position, $V_{0.7}(0)$ is the axial velocity at $0.7R$ in the rotor plane, $V_{0.7}(x_i)$ is the axial velocity at $0.7R$ and downstream position x_i. The methodology is summarized below.

1. Iteration starts with an initial guess of tangential vortex density $\gamma_{t(i)}$ for each vortex ring. Equation 3.1 is used for the calculation. The strength of the vortex ring is calculated as follows,

$$\Gamma_i = \left(\frac{1}{2} \gamma_{t(i)} + \gamma_{t(i-1)} \right) dx \tag{3.4}$$

2. The axial induced velocity is initially guessed to be free stream velocity and the wake radius to be rotor radius (r)

3. Axial induced velocities w_x for the vortex ring strength Γ_i are calculated at three different locations, small distance dy outside the vortex ring, small distance dy inside the vortex ring, and at $0.7r_i$ (positions marked by crosses in Figure 3.2).

4. Axial velocity at wake surface is taken as the average of axial velocities at small distance dy to both sides of the surface (crosses in positions outside and inside the wake in Figure 3.2)

$$V_a = U_\infty + \frac{1}{2} (w_x(r + dy) + w_x(r - dy)) \tag{3.5}$$

5. The new estimate for the tangential vortex density $\gamma_{t(i)}$ is calculated with the newly calculated axial induced velocity V_a using expression 3.1

6. The wake radius is calculated by the equation of continuity for axial flow (equation 3.3).

7. The process is repeated till the wake radius is converged.

With the calculated vortex densities $\gamma_{t(i)}$, the axial and radial induced velocities at all grid points are calculated using formulae A.1 and A.2. A singularity results when the control points approach the vortex ring. To circumvent this issue, a linear profile is assumed near the vortex core. Total induced velocity at each evaluation point can be calculated by adding up the induced velocity contribution from each vortex ring. The total induced velocities in $x-$, $y-$ and $z-$directions at a point are calculated by adding up the velocity contributions from $N-$vortex rings, as follows

$$V_a = \sum_{i=1}^{N} w_x(r, \theta, x) \tag{3.6}$$

$$V_y = cos\left(tan\left(\frac{z-H}{y}\right)\right)\sum_{i=1}^{N} w_y(r,\theta,x) \tag{3.7}$$

$$V_z = sin\left(tan\left(\frac{z-H}{y}\right)\right)\sum_{i=1}^{N} w_y(r,\theta,x) \tag{3.8}$$

To reduce the computational time, domain is split into two equal parts, with $x-z$ plane as symmetry plane. The results are mirrored along the $x-z$ plane.

Pressure Gradients

The pressure in the wake can be calculated from Bernoulli's equation. Pressure at any evaluation point, p_2 is calculated using velocity u_2, free stream velocity u_∞ and ambient pressure p_∞ as follows,

$$p_\infty + \frac{1}{2}\rho u_\infty^2 = p_2 + \frac{1}{2}\rho u_2^2 \tag{3.9}$$

with, p_∞ is ambient pressure, u_∞, free stream velocity. The pressure gradients in 3 directions, $\frac{\partial p}{\partial x}$, $\frac{\partial p}{\partial y}$ and $\frac{\partial p}{\partial z}$ are calculated from pressure using finite differences. The perturbation variables u, v, w in the perturbed Parabolized Navier Stokes equations are initialized using the near wake model. The induced velocities V_a, V_y and V_z are given as an initial guess to the perturbation variables.

3.2   Purpose of improving the vortex models

There is a discrepancy between the WAKEFARM results and experimental data (see Figure2.10, Figure 2.9). The experiments show a higher velocity deficit compared to velocity deficit predicted by WAKEFARM. Towards the centre of the wake, the experimental velocity profile shows a flattened behaviour. This discrepancy might be the result of using a relatively simple vortex ring model to model the wake of wind turbine and ignoring the root vortex while modelling the wake of wind turbine

- **Need for radially varying circulation model:** The existing models in WAKE-FARM assume a uniform loading along the actuator disk, hence the vorticity is trailed only at the edges. Such a model of a wind turbine is hypothetical. In a real wind turbine, the bound circulation varies along its span, as the bound circulation has to vanish continuously at the blade extremities. Hence a model of wind turbine with radially varying circulation is needed.

- **Need for a root vortex model:** While modelling the wake of a wind turbine, the length of the root section and hub is mainly taken as zero. The hub vortex is

typically modelled as a single axial vortex not influencing the axial component of velocity[31]. Real wind turbines do have a root section and a rotor hub, to which all the blades are attached. The energy is not extracted in the hub and root sections of the wind turbine, hence their presence does have an impact on the axial velocity profile. The root vortex too plays an important role in the evolution of wake closer to the turbine, the near wake and hence on the wake far downstream of the turbine, known as far wake (see Figure 2.1) [12, 31]. Thus modelling the flow near the root section is essential.

- **Need for a helical wake model:** At extremely high tip speed ratios, the pitch of the helix becomes extremely small and the spirals of the helix come closer to each other (see Figure 3.4). In such conditions, the helical tip vortices can be approximated as circular vortex rings. The assumption is erroneous when the tip speed ratios are small. Apart from that, helical fragments with shorter radius cannot be approximated as vortex rings even at higher tip speed ratios (see Figure 3.4). To include the effect of finite tip speed ratios and finite number of blades, a helical model of the wake is necessary.
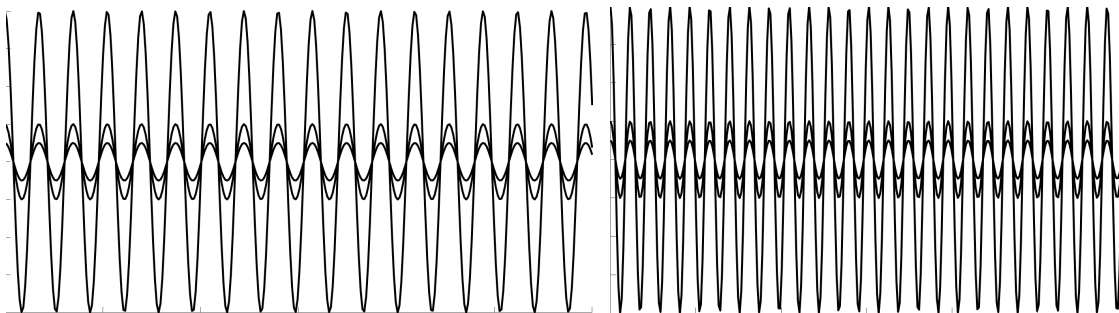
Figure 3.4: Side view of trailing helices, for different tip speed ratios.$\lambda = 6$(left),$\lambda = 9$(right)

In order to model the near wake of a wind turbine in a realistic way, a helical wake model of a wind turbine with a helical root vortex was developed. In the next section, the development of varying circulation constant axial induction model is explained.

3.3   Development of varying circulation, constant axial induction model

3.4   Span varying bound circulation

Joukowsky defined an ideal rotor as the one with constant circulation along its span [32]. The Joukowsky rotor has an uniform loading, hence a constant bound circulation along the blades. However in reality wind turbine rotors have a varying circulation along the blade span. For a real flow, the bound circulation varies along the span, because the circulation has to vanish continuously at the blade extremities. As a result of this, the strength of the vortex sheets increases towards the blade extremities [12]. Due to this varying bound circulation $\Gamma_b(r)$, vorticity is trailed from different sections along the blade. When the circulation is not constant along the blade, each blade sheds a helical vortex sheet from its trailing edge. The axial component of helical sheet induces tangential velocity in anti-clockwise direction (opposite to the direction of rotation of rotor). The azimuthal component of helical sheet induces an axial velocity in the upstream direction [12]. The helical sheet of vorticity undergoes expansion and distortion. As a starting point, wake expansion and distortion are ignored.

3.4.1   Discretization of the wake and blade

The blades of rotating machinery, whether wind turbines, propellers, or helicopter rotors, shed vortices into the wake. These vortices convect downstream and are described by helical paths. The helical wake behind a wind turbine is shown in Figure 3.5. The trailed vorticity follows a helical path as can be seen in Figure3.5 (see section D to know the components of vorticity in wind turbine). Straight vortex filaments were used to discretize the trailed vortex. The helical sheet is discretized into a finite number of azimuthal straight vortex filaments. After knowing the geometry of the wake, the bound circulation of the lifting line can be calculated for different flow conditions. The aerodynamic properties of the blade are required for this fixed wake type of modelling. The approach described in this section requires the axial induction factor of the blade to be known. The bound circulation along the blade varies in a continuous fashion. The continuous bound circulation in lifting line is discretized into discrete straight vortex filaments. At the extremities of each vortex filament, vorticity is trailed.
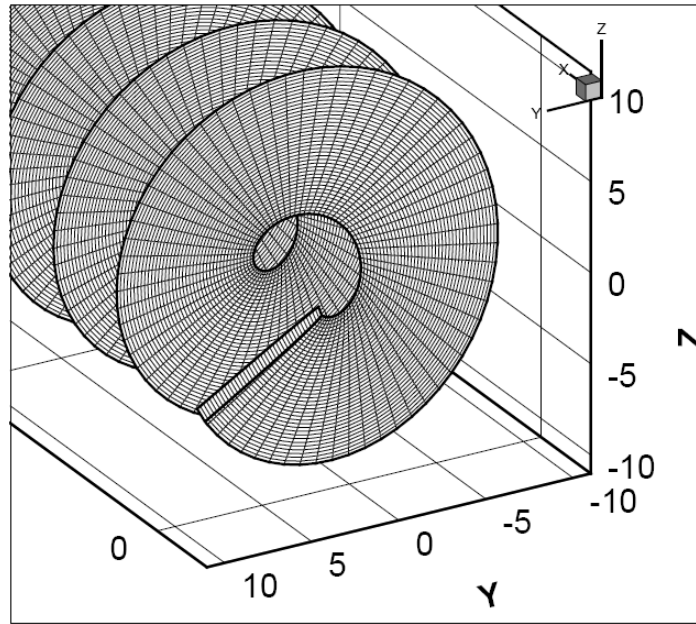
Figure 3.5: Helical wake structure behind a wind turbine
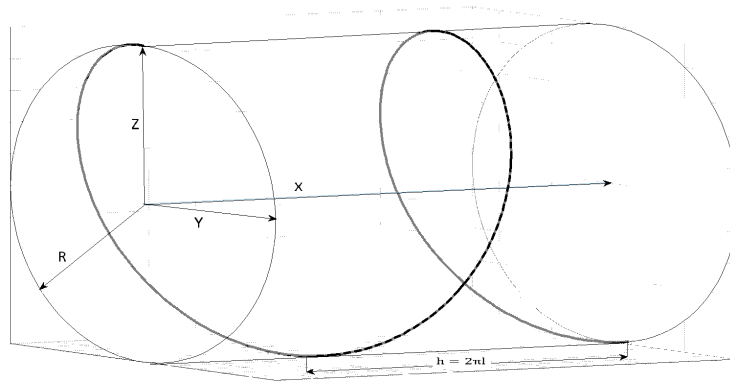
Figure 3.6: Geometrical parameters of a helical filament

3.4.2   Coordinate system

The numerical method employs two sets of coordinate systems. The global coordinate system used in WAKEFARM is defined in 2.1. A local coordinate system is defined for the near wake model. The origin of the local coordinate system is at the centre of the nacelle. The $x-$axis is aligned with stream-wise direction, $y-$axis along the cross flow direction and $z-$ axis extending from the hub upwards (see Figure 3.6).

3.4.3 Conventions

The canonical helix has a helical pitch $'h'$. The helix has a radius $'R'$. A relevant torsional parameter l, following the helix is defined as follows.

$$l = \frac{h}{2\pi} \tag{3.10}$$

the pitch h of the helix is calculated as follows,

$$h = \frac{2\pi R}{\lambda} \tag{3.11}$$

where λ is the tip speed ratio. The helical vortex trailed from each blade has a constant phase offset between them. The vortex trailed from blade b has the following azimuthal coordinate

$$\theta(t) = \Omega_w t + \frac{2\pi(b-1)}{N_b} \tag{3.12}$$

where Ω_w is the angular velocity of the helical wake It is assumed that the angular velocity of the helical wake Ω_w is same as the angular velocity of the wind turbine rotor. The canonical helix of radius R and slope $\frac{l}{R}$ or pitch $(2\pi l)$ is described by the following parameterization [33].

$$z(t) = R\cos(t) \tag{3.13}$$

$$y(t) = R\sin(t) \tag{3.14}$$

$$x(t) = lt \tag{3.15}$$

while including effects of wake expansion, the radius R of helix, is not constant, but a function of t $R(t)$. The parameter $'t'$ is dimensionless. As $'t'$ increases, the point $P[x(t), y(t), z(t)]$ traces a left-handed helix (see Figure 3.8). While defining the geometry of the vorticity system, the distribution of vorticity system is defined by

- The number of spanwise vortex filaments N_r

- The number of streamwise vortex filaments N_h

- Length of the wake

The length of the helix is selected as $7.5D$.

3.4.4   Constructing a vortex system

The helical sheet of vorticity is resolved into a vortex system. In steady, axisymmetric flow, the shed vortices can be ignored, and as a result the model can be simplified to a vortex system as shown in Figure 3.7. The blade is segmented in spanwise direction. A vortex ring is collocated at each blade segment. The bound vortex is located at the quarter-chord position. At the blade, vortex segments trail the chord up to 1/4 chord, and then convect along the helical wake. The helical trailed vortex is discretized into vortex rings made up of straight vortex filaments. As the shed vortex is neglected, the vortex ring ends where the wake ends (starting vortex). According to Helmholtz theorem, the circulation Γ_b is constant for all the filaments in the vortex ring. The direction of the filament defines the direction of the circulation.
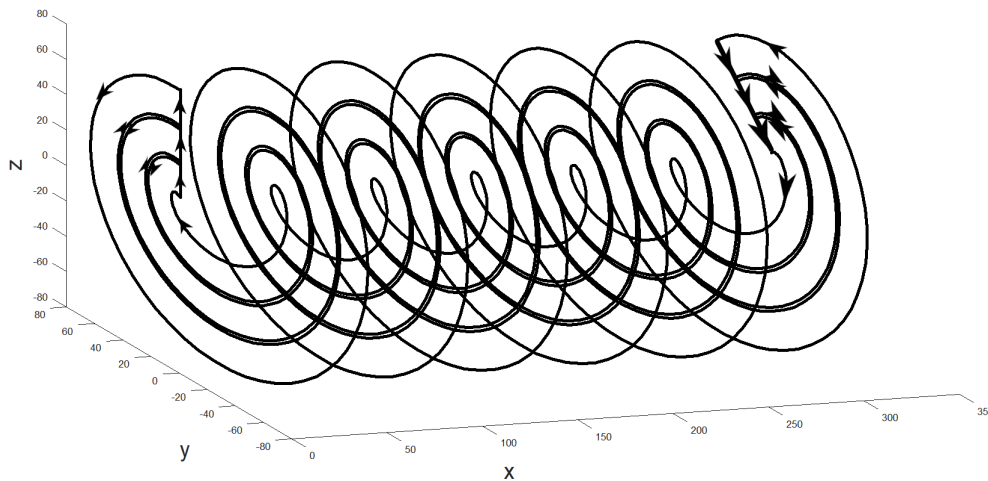
Figure 3.7: Vortex system in a single bladed wind turbine.

3.4.5   Assumptions

Assumptions used in this study are summarized below:

- The blade is represented as a lifting line with varying bound circulation along its span.

- The lifting line of the first blade is at azimuth position corresponding to azimuth angle $\theta = 0$.

- The flow is assumed to be axisymmetric and is assumed to be steady, i.e the bound circulation Γ_b doesn't change with time. As a consequence, there is no vortex shed in the wake (shed vortex is neglected).

- In reality the helical pitch h of the different trailed vortices vary along the span $h = h(r)$. For the sake of simplicity, the helical pitch of all the trailed vortices is assumed to be the same.

- Helical trailed vortices are assumed to be infinitely thin

- The straight vortex segments in lifting line and the wake have a constant vortex strength.
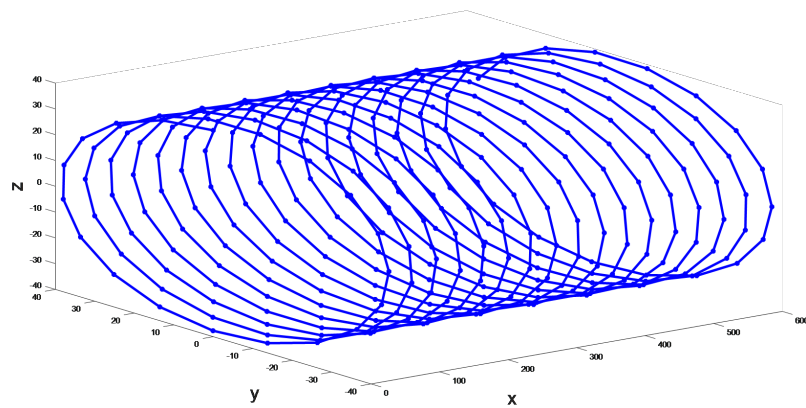
Figure 3.8: Representation of helix by straight vortex segments, the helix has a radius r_0 and length $7.5D$

3.4.6 Vortex line induced velocity

As both the trailed and bound vortices are discretized as straight segments, the velocity induced by a single vortex filament needs to be known in order to calculate the total velocity induced by the entire helix and lifting line. The velocity induced by a straight vortex filament of constant vortex strength Γ at control point x_p is expressed analytically by the Biot-Savart law [6].

$$\vec{u}_{\Gamma_b(x_p)} = \frac{\Gamma(r_1 + r_2)(\vec{r_1} \times \vec{r_2})}{4\pi r_1 r_2(r_1 r_2 + \vec{r_1}.\vec{r_2})} \tag{3.16}$$

where $\vec{r_1}$ and $\vec{r_2}$ are distance vectors from the start $\vec{x_1}$ and end of vortex segment $\vec{x_2}$, to the control point $\vec{x_p}$, Γ is the strength of the vortex filament, Γ_b in our case. All the straight vortex filaments that compose the helix have the same vortex strength Γ_b r_1 and r_2 are magnitudes of the distance vectors.
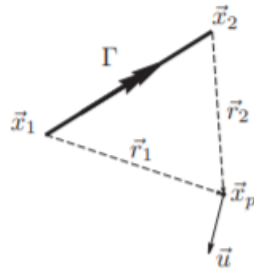
Figure 3.9: Schematic for Biot Savart law [6].

when the control point is close to the vortex filament or the vortex filament axis, the induced velocities show an asymptotic behaviour. As a remedy, a cut off radius parameter δ is included in the denominator in equation the following equation [6]

$$\vec{u}_{\Gamma_b}(x_p) = \frac{\Gamma_b(r_1 + r_2)(\vec{r_1} \times \vec{r_2})}{4\pi r_1 r_2(r_1 r_2 + \vec{r_1}.\vec{r_2}) + (\delta l_0)^2} \tag{3.17}$$

where l_0 is the length of the vortex filament.

3.4.7 Influence coefficients

The control points are selected as midpoints of the spanwise vortex filaments in the lifting line. The trailed helix is segmented into N_h stream-wise elements. As the control points are on the lifting line, the velocity contribution from the lifting line can be ignored. The lifting line is divided into N_r span-wise elements. These N_r blade sections trail N_r vortex rings. Let i be the index of a control point and j be the index of the vortex ring. The velocity induced by a vortex ring j, at a point i is $\vec{u}_{i-j}$. The

quantity $\vec{u}_{i-j}$ is a vector which has three components, u_{i-j}, v_{i-j} and w_{i-j} . Since the velocity induced by a vortex filament is linear, u_{i-j} can be written as

$$\vec{u}_{i-j} = \vec{u}_{i-j|\Gamma=1} \times \Gamma_{b(j)} \tag{3.18}$$

the total velocity induced by N_r vortex rings at the control point i is defined as follows

$$\vec{u_i} = \sum_{j=1}^{N_r} \vec{u}_{i-j} = \sum_{j=1}^{N_r} \vec{u}_{i-j|\Gamma_b=1} \times \Gamma_{b(j)} \tag{3.19}$$

Now, the term influence coefficient a_{i-j} is introduced as follows,

$$a_{i-j} = \vec{u}_{i-j|\Gamma_b=1} \tag{3.20}$$

It is the velocity induced by the vortex ring j of unit circulation, $\Gamma_{b(i)} = 1$ at the collocation point. Once the total velocity acting on the lifting line is computed, the boundary conditions can be applied on the right hand side. The axial component of velocity at the control points is a combination of induced velocity u_i and free stream velocity U_∞. The axial induction factor is assumed to be constant along the lifting line. From actuator disk theory, the axial component of velocity on lifting line can be calculated as $U_\infty(1-a)$. The number of blades N_b is assumed to be greater than 3. This is done to get closer to the actuator disk solution (infinite number of blades).

$$u_i + U_\infty = U_\infty(1-a) \tag{3.21}$$

The induced axial velocity component at control point 1, due to all horseshoe vortex ring is therefore

$$u_1 = a_{11}\Gamma_{b(1)} + a_{12}\Gamma_{b(2)} + a_{13}\Gamma_{b(3)} + ... + a_{1N_r}\Gamma_{b(N_r)} \tag{3.22}$$

In matrix notation, equation 3.21 can be written as,

$$A_{ij}\Gamma_{b(i)} = U_\infty(1-a) \tag{3.23}$$

A_{ij} is a matrix of dimension $N_r \times N_r$. $\Gamma_{b(i)}$ has a dimension of $N_r \times 1$. A_{ij} is given by,

$$A_{ij} = \begin{bmatrix} a_{11} & a_{12} & a_{13} & . & . & . & . & a_{1N_r} \\ a_{21} & a_{22} & a_{23} & . & . & . & . & a_{2N_r} \\ a_{31} & a_{32} & a_{33} & . & . & . & . & a_{3N_r} \\ . & . & . & . & . & . & . & . \\ . & . & . & . & . & . & . & . \\ a_{N_r 1} & a_{N_r 2} & a_{N_r 3} & . & . & . & . & a_{N_r N_r} \end{bmatrix} \tag{3.24}$$

The solution of the above described problem is obtained using LU matrix decomposition technique. Initially the root radius is set to zero, (the aerodynamics section of blade starts at 0). The induction factor a on the lifting line is specified. The input parameters used for the simulation are given in Table 3.1.

Table 3.1: Input parameters

Free stream velocity at hub height U_∞	11 m/s
axial induction factor at the rotor disk a	0.333 (Betz limit)
Tip speed ratio λ	6
Hub height H	80 m
Wind turbine diameter D	80 m
Number of blades N_b	6
Number of stream wise vortex segments N_h	318
Number of span wise vortex segments along the blade N_r	25
Length of wake	7.5 D

3.4.8 Wake expansion effects: prescribed wake model

The shape of the wake has a significant influence on the induced velocities at the rotor. The helical wake convects, distorts its shape, expands due to the continuity equation. Apart from this, roll up of wake also takes place. To include all these effects, the induced velocities at each point in wake should be calculated and based on the induced velocities, the location of each vortex filament has to be found out in the next time step [12, 7]. Such model is referred to as a free wake model. However, they take enormous amount of computational time when implemented in a straightforward way, since the wake radius is a part of the solution process. There are several problems associated with the model, which include, handling of vortex elements as they get close to each other and remeshing. To simplify the complexity of the problem, the geometry of the wake can be represented by a prescribed wake model. The location of vortex filaments is hence known. The wake radius is taken from the existing vortex ring model in WAKEFARM (Øye's vortex ring model) [5]. In this model, the one-dimensional wake radius is calculated using continuity equation for axial flow, i.e. the total flow through each section of wake is same as the flow through the rotor disc (see Equation 3.3). The wake radius varies depending on the thrust coefficient C_t specified at the rotor disk. The setbacks of the prescribed wake model are, wake roll up is not captured and it cannot be used in yawed inflow conditions. The wake remains as a helical sheet, in this prescribed wake approach. In the figure below, wake radius is plotted against the distance from the turbine in stream-wise direction.

3.5   Results from the vortex model

The trailed vorticity distribution and bound circulation distribution obtained by solving the system with input parameters in Table 3.1, is plotted in Figure 3.11 and Figure
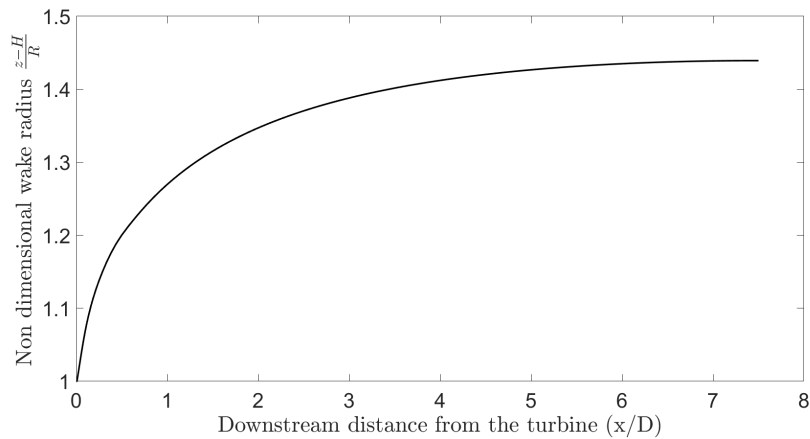
Figure 3.10: Non-dimensional wake radius calculated from Oye's vortex ring model [5], as a function of distance from the turbine for an axial induction factor, $a = 0.33$
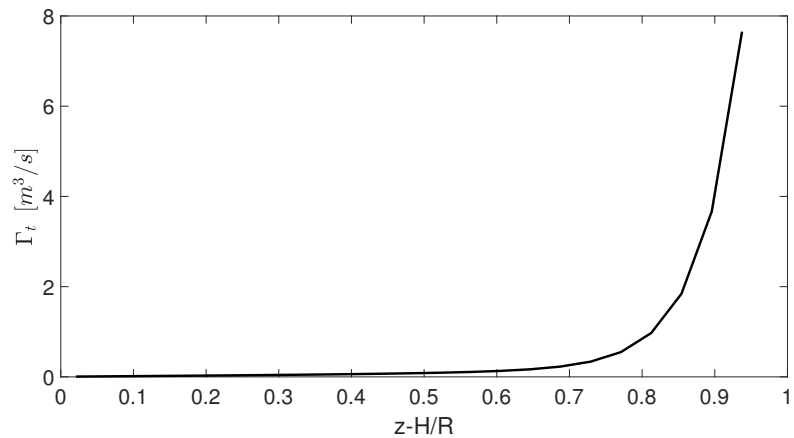
Figure 3.11: Trailed vorticity distribution along the blade span

3.12. Near the root section, no vorticity is trailed. This is because of the assumption that root radius is zero. The root vortex in this case, is a straight line and it does not influence the induced velocity in axial direction.

The horizontal velocity profile obtained in the cross flow direction at hub height at a downstream distance of $2.5D$ is shown in figure 3.13. The input parameters used to obtain the result are given in table 3.1. A hundred points were used in the scan line.
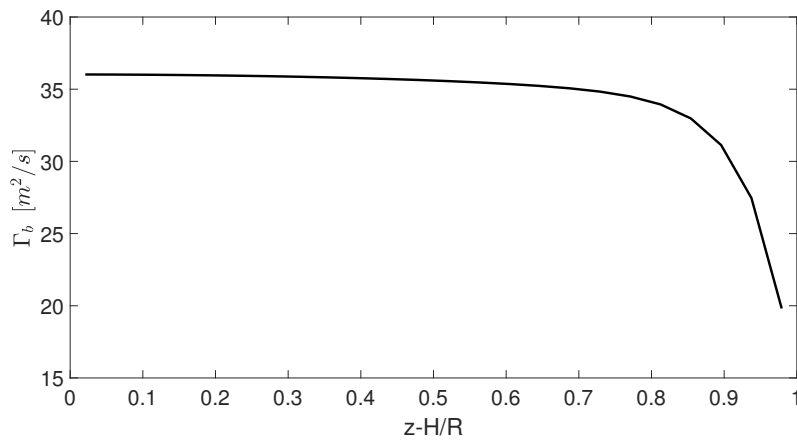
Figure 3.12: Bound circulation distribution along the lifting line corresponding to an axial induction factor, $a = 0.33$
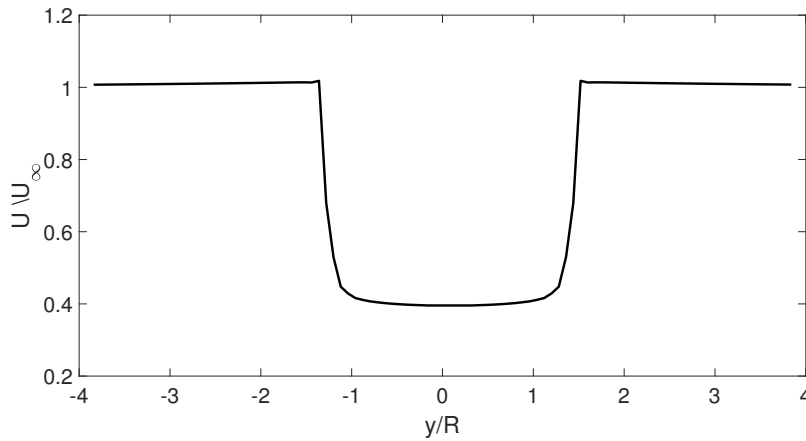
Figure 3.13: The horizontal velocity profile in the cross flow direction at hub height for a free stream velocity of $11 m/s$ at a distance of $2.5D$ downstream of the rotor.

3.5.1 Evolution of wake

In the figure 3.14, the horizontal velocity profile as a function of y at various positions downstream of the turbine is plotted. It can be seen that the velocity profiles in the wake of wind turbine are self similar. They are also axisymmetric (due to the assumption made). The wake radius gets larger as the distance from the turbine increases (continuity equation) and this is reflected in the velocity profiles.

3.5.2 Effect of Number of blades

The number of blades N_b is varied, keeping the same values of N_h, N_r to see its effect on the solution. Figure 3.15 shows the horizontal wind speed profile at $2.5D$
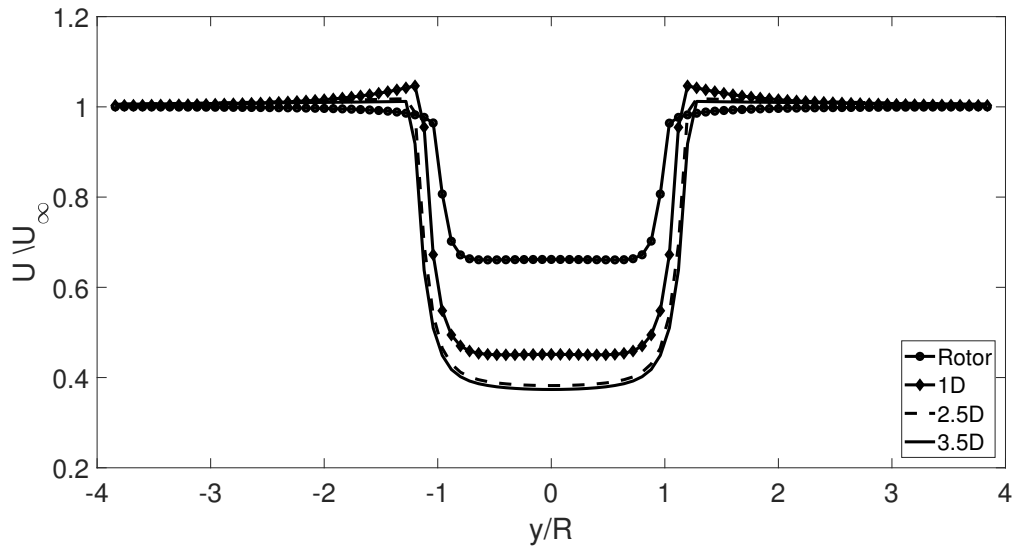
Figure 3.14: Normalized horizontal velocity profiles in the cross flow direction at hub height for an axial induction factor a of 0.33 at various locations downstream of the wind turbine rotor. The parameters used are $N_b = 6$, $N_r = 25$, $N_h = 318$

behind the rotor for different number of blades N_b. As the number of blades N_b increases, the velocity distribution, inside the wake radius becomes fairly constant. The velocity distribution gets closer to the Vortex ring case (infinitely bladed rotor). There is no significant change in the velocity profile for N_b values greater than 24.

3.5.3   Effect of number of span-wise vortex filaments

The number of span-wise vortex filaments is varied, keeping N_h at 318 and N_b at 12. From, it is inferred that as N_r is increased, there is no significant improvement in the velocity profile after $N_r = 45$. The solution obtained using $N_r = 75$ is most accurate result (Figure 3.16), as the continuous bound circulation is discretized into discrete bound circulation. The simulation with $Nr - 75$ takes 9 times the computational time required for $Nr - 25$. $N_r - 25$ can still be used, as there is no significant improvement with increase in N_r.

3.5.4   Cosine spacing

The bound circulation distribution shows large gradients near the tip and root sections of the blade and is relatively constant in the middle sections. Hence by using cosine distribution, the spanwise vortex filaments can be clustered near the tip and root of the blade.
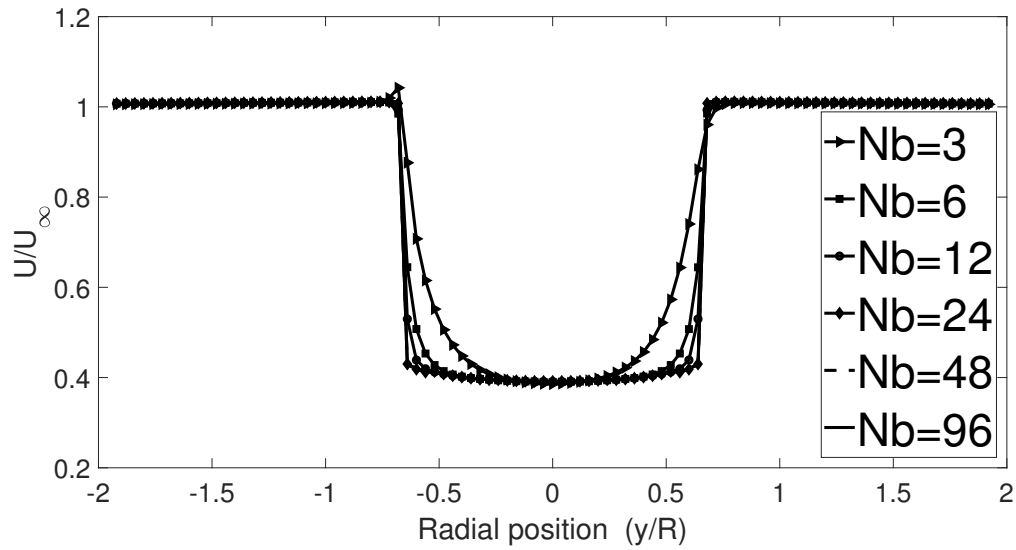
Figure 3.15: The horizontal velocity profile in the cross flow direction at hub height
for an axial induction factor, a of 0.33 at a distance of $2.5D$ downstream
of the rotor, for $N_b = 3, 6, 12, 24, 48, 96$ with $N_r = 25$ and $N_h = 320$
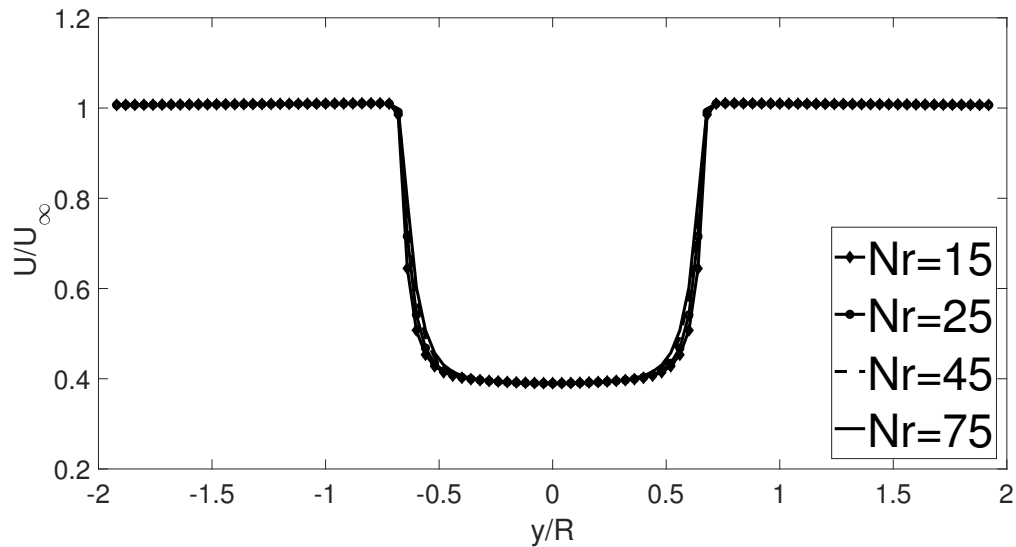
Figure 3.16: The horizontal velocity profile in the cross flow direction at hub height
for an axial induction factor, a of 0.33 at a distance of $2.5D$ down-
stream of the rotor. The number of span-wise vortex filaments are
$N_r = 15, 25, 45, 75$ with $N_h = 320$ and $N_b = 6$

$$r_i = R_r + \frac{(R - R_r)}{2} \times \left(1 - cos\pi \left(\frac{i - 1}{N_r - 1} \right) \right)$$

$$1 \leq i \leq N_r \tag{3.25}$$

where $R_r =$ root radius

   A comparison between horizontal velocity profile obtained using uniform spacing and cosine spacing is shown in figure 3.17. The input parameters used to obtain the result are given in table 3.1. The bound circulation obtained using both uniform and cosine spacing is shown in Figure 3.18 [7].
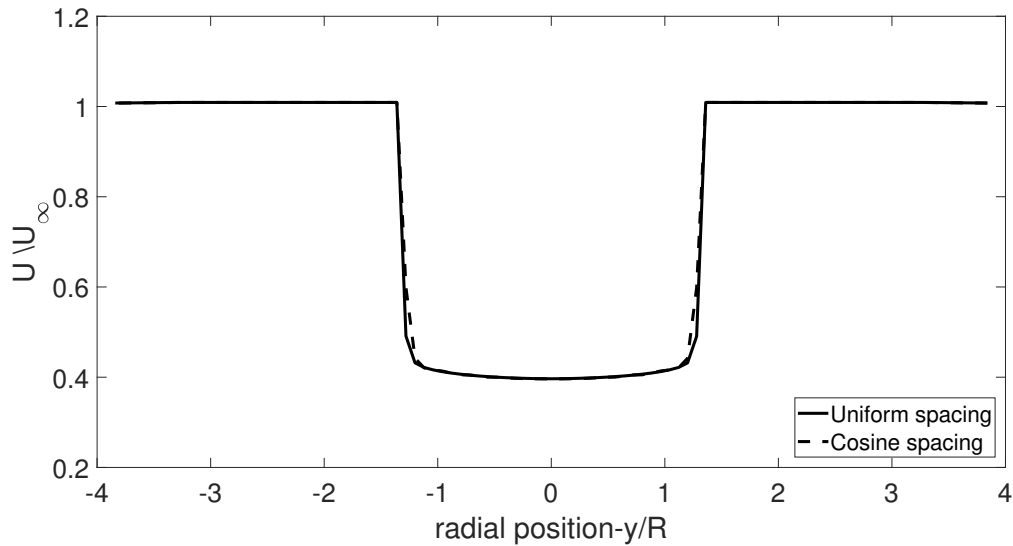

Figure 3.17: The horizontal velocity profile in the cross flow direction at hub height at a distance of $2.5D$ downstream of the rotor obtained using cosine and uniform spacing.
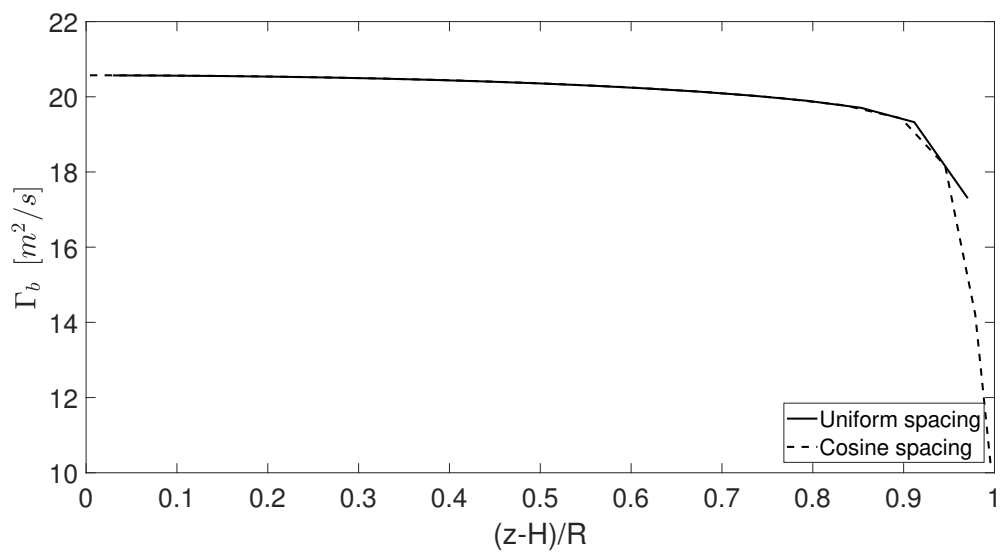

Figure 3.18: Bound circulation distribution along the lifting line obtained using cosine and uniform spacing

The velocity profile obtained with cosine spacing is better in terms of resolution (see Figure3.17).

3.5.5 Calculating pressure gradients

The induced velocities obtained from the near wake model are used as an initial guess to perturbation u, v, w in the perturbed RANS equations (see equation 2.8, equation 2.10, equation 2.11). The elliptic terms in the axial momentum equation are neglected to make the momentum equation parabolic. In the far wake the axial pressure gradient is negligible and hence it can be ignored in the axial momentum equation. However in near wake, the stream-wise pressure gradients are high due to the presence of wind turbine rotor. Hence the axial pressure gradient is prescribed using the axial pressure gradient calculated from the inviscid vortex method. This axial pressure gradient is added as a source term in momentum equations along with the body force term. In the previously existing vortex ring method, pressure field was calculated from Bernoulli's equation (3.26). Pressure gradients in all three directions are calculated from the pressure field using finite differences.

$$p_1 + \frac{1}{2}\rho V_1^2 = p_2 + \frac{1}{2}\rho V_2^2 \tag{3.26}$$

with, 1 is a point far downstream of the rotor, where the pressure is ambient pressure and 2 is the evaluation point for pressure. As the aim is to calculate the pressure gradients and not the pressure, Navier-Stokes equations can be used to obtain the pressure gradients, with the assumption that the flow is inviscid, incompressible and steady. Thus the pressure gradients corresponding to the velocity field predicted by inviscid vortex method can be found.

$$u_j \frac{\partial u_i}{\partial x_j} = -\frac{1}{\rho}\frac{\partial p}{\partial x_i} \tag{3.27}$$

The axial pressure gradient at hub height and centre of nacelle, obtained from Navier-Stokes equations is depicted in the figure 3.19. An axial induction factor , $a = 0.33$ was specified on the lifting line.

According to actuator disk momentum theory, the velocity of wind decreases behind the wind turbine and therefore the stream tube expands (continuity equation). The static pressure increases until it reaches atmospheric pressure p_∞ (Bernoulli's equation). This trend is also seen in Figure 3.19. Somewhere between downstream positions $2D$ and $3D$, pressure recovers back and reaches p_∞. Hence far wake region starts between downstream position $2D$ and $3D$.
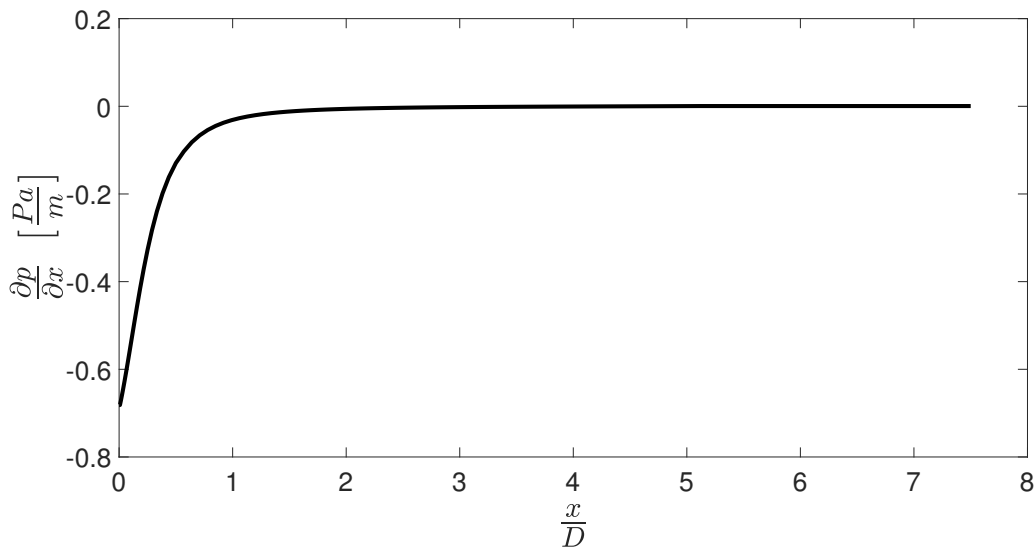
Figure 3.19: Axial pressure gradient at hub-height and centre of nacelle as a function of distance downstream of the turbine

3.6 Root vortex inclusion

In most modern wind turbines the aerodynamic shapes in the blades near the root are connected to a cylindrical section of the blade which then connects the blade to the hub. For the sake of simplicity, we assume that the root vortex behaves in a similar way as the tip vortex, i.e the blade starts at some root radius, hence there is a sharp gradient in bound circulation Γ_b at the root and tip, causing strong root and tip vortices. The root vortex is assumed to lie in the helical sheet, not different from other trailing vortices. The root vortex thus can be included, by specifying a root radius. The aerodynamic blade shapes now, do not start at 0 but start at the root radius. The root radius here includes the hub radius of the rotor and the length of cylindrical root section in the blade. The hub and the cylindrical root section is not modelled here. For analysis, an existing wind turbine is selected. The wind turbine has a hub radius of $2.5m$, cylindrical root section from the hub until $6.2m$. The specifications of the wind turbine are taken from [9].

The input parameters used for modelling the wake are given in the Table 3.2. The bound circulation distribution is shown in the left hand side of Figure 3.20. The trailed vorticity distribution is shown in left hand side of Figure 3.21. A negative trailed circulation can be seen near the root of the blade. The negative sign implies that the direction of rotation of root vortex is opposite to that of the tip vortex.

The horizontal velocity profile in cross flow direction at hub height and at a distance $2.5D$ downstream of the turbine is shown in Figure 3.22. A hundred points were used along the scan line. The hump near the root section is caused because

Table 3.2: Input parameters for modelling root vortex

N_h	318
N_r	25
N_b	12
U_∞	$11m/s$
a	0.33 (Betz limit)
R	$40m$
Root radius R_r	6.2 m
Length of wake L_w	$7.5D$
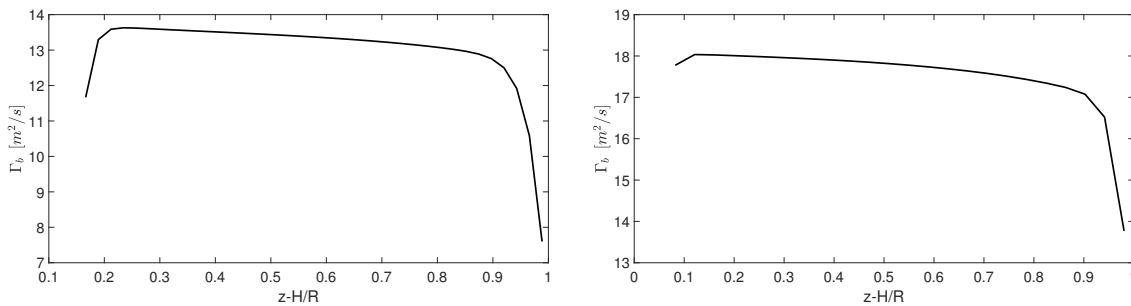
Figure 3.20: Bound circulation distribution along the lifting line corresponding to an axial induction factor, $a = 0.33$ and Root radius, $R_r = 6.2m$ (left),$R_r = 2.5m$ (right)
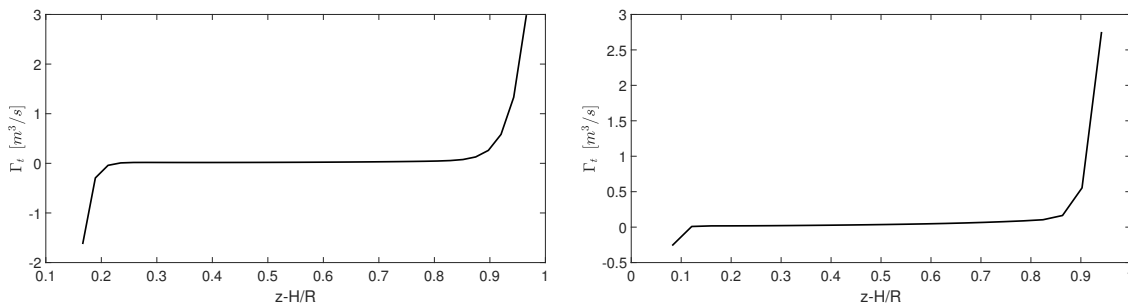
Figure 3.21: Trailed vorticity distribution along lifting line corresponding to an axial induction factor, $a = 0.33$ and $R_r = 6.2m$ (left),$R_r = 2.5m$ (right).

of the positive velocity induced by the root vortex. The flow in the root section becomes free stream velocity because of the strong gradient in bound circulation at the root section. This can be avoided by including a model for the cylindrical root section and hub of the rotor. By doing so, the sharp gradient in bound circulation can be reduced, which will result in a weaker root vortex.
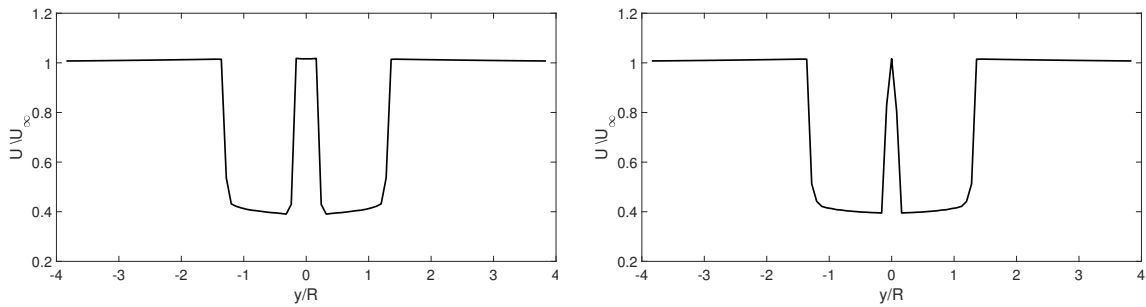
Figure 3.22: The horizontal velocity profile in the cross flow direction at hub height for an axial induction factor $a = 0.33$ and root radius, $R_r = 6.2m$ (left), $R_r = 2.5m$ (right) at a distance of $2.5D$ downstream of the rotor. A hundred points were used along the scan line.

The evolution of the wake is shown in Figure 3.23. The increase in the width of the wake, due to continuity equation can be seen. As per momentum theory, the velocity deficit at $2.5D$ is twice the velocity deficit at the rotor.
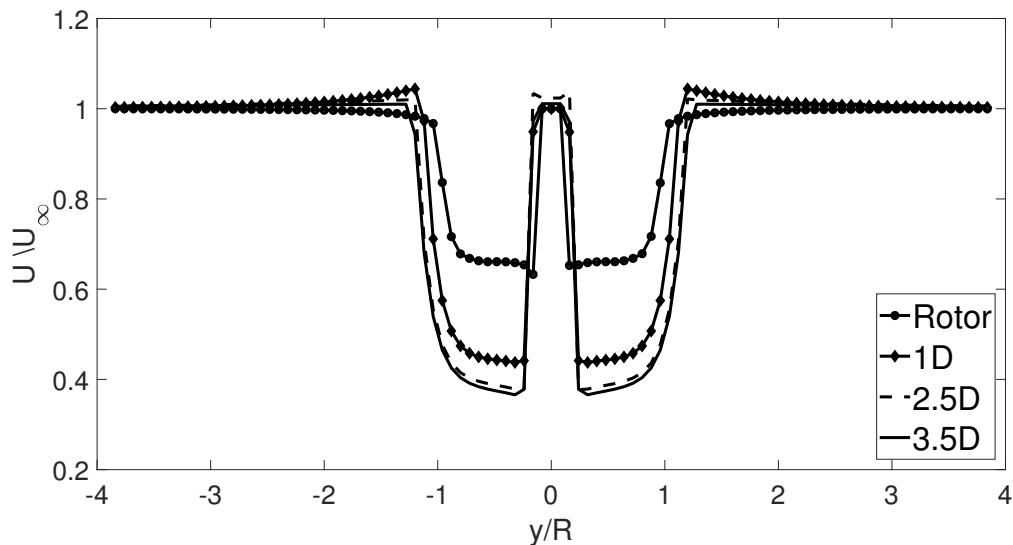
Figure 3.23: Normalized horizontal velocity profiles in the cross flow direction at hub height for an axial induction factor a of 0.333 at various locations downstream of the wind turbine rotor. A hundred points were used along the scan line. The root radius is taken as $6.2m$

Wind turbines produced by few turbine manufacturers have blades where the aerodynamic shapes start at the hub (see Figure3.24). The root radius in this case is taken as the hub radius. A root radius of $2.5m$ is assumed. The trailed vorticity distribution is shown in the right hand side of Figure 3.21. The size of the hump near

Table 3.3: Input parameters used to simulate the wind turbine.

N_h	N_b	N_r	U_∞	a	λ	R	H	L_w	Number of points
320	3	25	11 m/s	0.245	8	40 m	70m	600 m	97×97

the root section is reduced by reducing the root radius. This can be seen in Figure 3.22.

Figure 3.24: The hub designs in Enercon (left) and GE (right) blades [7].

3.6.1 Contour plots

In this section the axial induced velocity field in $X - Z$ plane behind the wind turbine is generated. An existing wind turbine is selected for analysis. The axial induction factor at the rotor is known as a function of wind speeds (see Figure B.1). The root radius is taken as $6.2m$, it includes the cylindrical root section and a hub (see Table B.1). The input parameters are listed in table 3.3. The axial induction factor is selected from the thrust coefficient curve in Figure B.1. A uniform velocity field is assumed. A total of 9409 points were used in the $X - Z$ plane with 97 points in x direction and 97 points in z direction

The contour plots of axial induced velocity at $y = 0$, are shown in Figure 3.25. The effect of root vortex can be seen close to the centre of the wake. Due to a stronger root vortex, the axial induced velocities near the centre of the wake become zero.

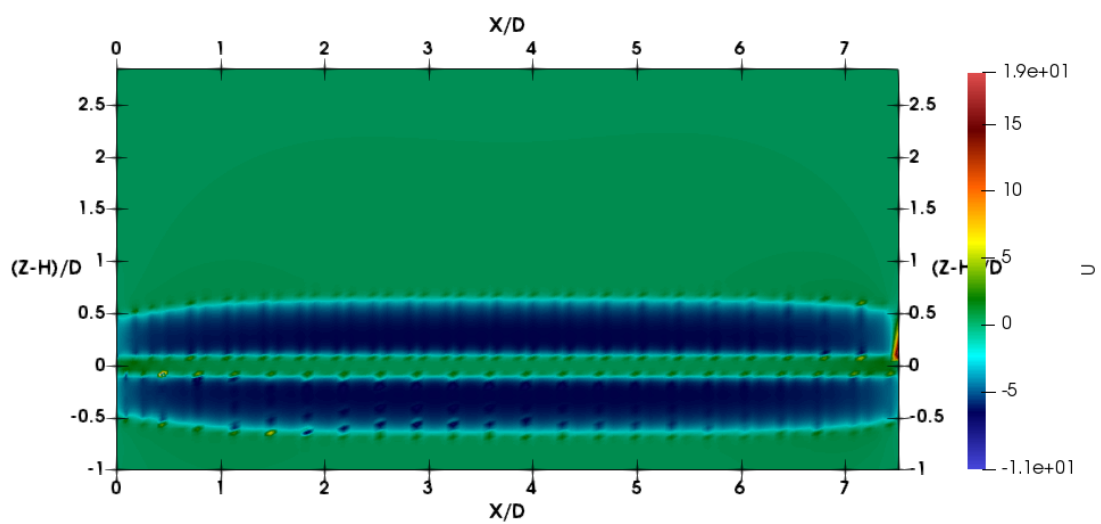**Figure 3.25:** Axial induced velocities in the $X - Z$ plane and $Y = 0$ for an uniform free stream velocity of $11 m/s$ and axial induction factor $a = 0.245$. The root radius is selected as $6.2m$

<div align="right">

Chapter 4

</div>

Varying axial induction along the blade

The upper limit for the maximum power that can be extracted by a wind turbine is defined by actuator disk theory. Actuator disk theory does not give an indication on the design of the wind turbine. The assumption of uniform induced velocity at the rotor used in the previous chapter does not hold for a real flow and most wind turbines have 3 blades. The axial induction factor in a real rotor is distributed along its span and also varies azimuthally due to tip losses associated with finite number of blades. The axial induction factor is high for azimuthal positions close to the blade and is lower for azimuthal positions away from the blade. Hence, a simulation of a real wind turbine with varying axial induction along its span was done and is explained in this chapter.

4.1 Calculating the bound circulation

The bound vortex strength can be calculated from the local flow velocities at the control points. Here, the bound circulation is calculated by matching the lift force obtained from Kutta-Jukouwski theorem to the lift associated with the local flow through an iterative process [7, 6]. A vortex system is constructed as explained in section 3.4.4. The assumptions used are the same as the ones explained in section 3.4.5 Alternatively, normal velocity boundary condition can be used to calculate the bound circulation along the blade. Once the bound vortex strength $\Gamma_b(r)$ is known, the flow field in the entire wake and the rotor plane could be calculated.

4.1.1 Methodology

The method is summarized below:
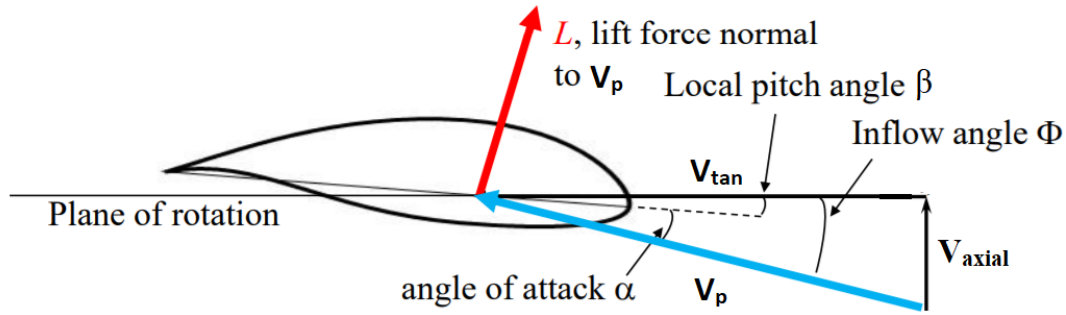
Figure 4.1: Velocity triangle in a wind turbine blade

1. The blade is approximated as a lifting line, which is then segmented into N_r span-wise vortex filaments.

2. The control points are at the midpoints of the span-wise vortex filaments.

3. Assume an initial distribution for bound circulation Γ_b

4. Calculate velocity perceived by the blade, axial V_{axial}, tangential V_{tan} and total V_p, from velocity triangle in (see Figure 4.1)

$$V_{axial} = U_\infty + u_i \tag{4.1}$$

$$V_{tan} = \Omega r + \left[U_\infty + u_i, \quad v_i, \quad w_i \right]^T \cdot \vec{\eta}_{tan} \tag{4.2}$$

$$V_p = \sqrt{V_{axial}^2 + V_{tan}^2} \tag{4.3}$$

u_i, v_i, w_i are velocity induced at the control point, as defined in section 3.4.7 $\vec{\eta}_{tan}$ is the normal vector in tangential direction

5. Calculate the flow angle ϕ and angle of attack α at the control points

$$\phi = tan^{-1} \left(\frac{V_{axial}}{V_{tan}} \right) \tag{4.4}$$

$$\alpha = \phi - \beta \tag{4.5}$$

with β is the blade twist angle at each control point.

6. Calculate bound circulation using formula given below. It is obtained by equating lift calculated with the angle of attack to the lift due to circulation

$$\Gamma_b = \frac{1}{2}cV_pC_l(\alpha) \tag{4.6}$$

where c-chord length at control point $C_l(\alpha)$, lift force coefficient calculated as a function of angle of attack from aerofoil polar data.

7. Update the new value of the circulation at each control point in the following manner

$$\Gamma_b = \Gamma_{b(old)} + D(\Gamma_{b(new)} - \Gamma_{b(old)}) \tag{4.7}$$

where, D is the relaxation factor, $\Gamma_{b(new)}$ is the value of bound circulation at current iteration and $\Gamma_{b(old)}$ is the value of bound circulation in previous iteration.

8. Go to step 4 with new estimate for Γ_b and repeat the steps 4-8 till convergence.

Figure 4.2 shows the span-wise segmentation of blade showing normal η_{axial} and tangential η_{tan} directions of a single blade panel.
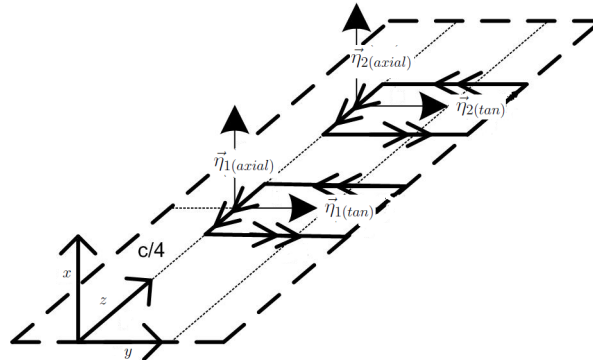
Figure 4.2: normal vectors in a wind turbine blade

4.1.2   Input requirements

The method requires the blade geometry to be known. The aerodynamic properties of aerofoils used in the blade are also needed. This is a setback of the model, as aerodynamic properties of the wind turbine are confidential. The input data needed is summarized below:

- Data of blade geometry: chord (c) and twist (β) distributions, number of blades N_b amount of span-wise vortex filaments N_r, root radius and tip radius (R)

Table 4.1: Properties of the selected wind turbine

Diameter	$80m$
Hub height	$70m$
Installed power	$2MW$
Cut in wind speed	$4m/s$
Rated wind speed	$16m/s$
Cut out wind speed	$25m/s$
Number of blades	3

Table 4.2: Input parameters used for simulation of the selected wind turbine blade

U_∞	$11.08m/s$
a	0.245
N_h	320
N_r	18
N_b	3
λ	8

- Operating conditions: Free stream velocities (U_∞), tip speed ratio, (TSR, λ), yaw angle (ψ), pitch angle(θ).

The flowchart of the algorithm is given in Figure 4.3. For analysis, an existing wind turbine was selected. The main properties of the turbine are listed in Table 4.1 [9].

Aerodynamic properties of the selected wind turbine

The power and thrust coefficient curves are listed in Figure B.1 [9]. A Generic model of the wind turbine selected has been established by Matthew J.Churchfield, National Renewable Energy Laboratory (manufacturer's specifications are confidential). The generic aerofoil properties have been extracted from [9] and are listed in TableB.1. The lift coefficient and drag coefficient data for the NACA airfoils were obtained from measurements in the VELUX wind tunnel [34, 10], whereas others were taken from the book by Abbott and von Doenho [35, 10]. The lift coefficient C_l as a function of angle of attack α for the five different aerofoils is shown in Figure B.9 The wake expansion effects are included by using a prescribed wake model (see 3.4.8). The axial induction factor as a function of wind speed is calculated from the thrust coefficient curves in Figure B.1. The input parameters used for analysis is given in Table 4.2. The rotor specifications are taken from Table B.1.
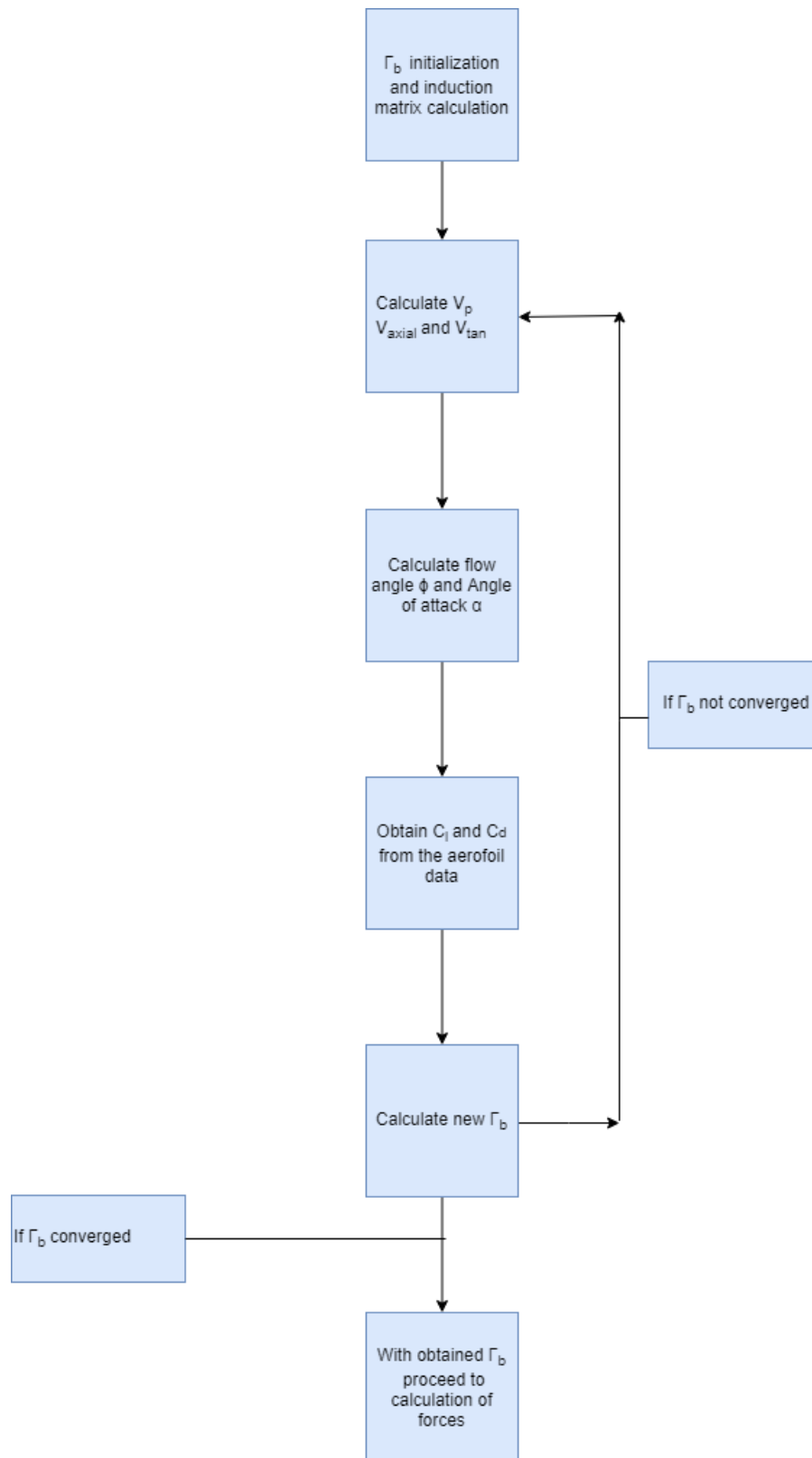
Figure 4.3: Flow chart of the lifting line algorithm
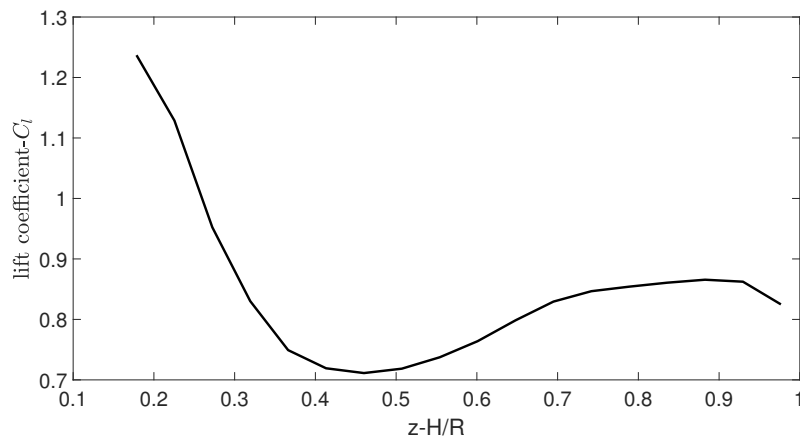
Figure 4.4: Distribution of lift coefficient, C_l along the lifting line
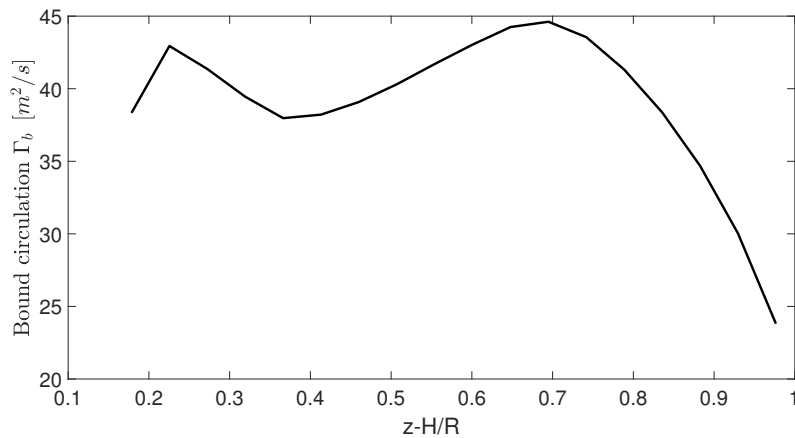
Figure 4.5: Distribution of bound circulation, Γ_b along the lifting line

4.2   Results from the model

The distribution of lift coefficient, C_l along the blade, obtained after the convergence of Γ_b is shown in Figure 4.4. The angle of attack and bound circulation distribution along the lifting line are shown in Figure 4.7 and Figure 4.5. It can be seen that the angle of attack in the outboard portion of blade is fairly constant. This is optimum for wind turbine operation. The horizontal velocity profile at hub height and at a downstream distance of $2.5D$ can be seen in Figure 4.8. The velocity profile inside the wake is not fairly constant as observed in the constant axial induction case mentioned in the previous chapter. The influence of the root vortex is felt in the form of hump near the centre of wake. The local axial induction factor along the lifting line is shown is Figure 4.6. The increase in axial induction near the root and tip sections of the blades is due to the presence of tip and root vortices.

Figure 4.6: Distribution of local induction factor, a along the lifting line
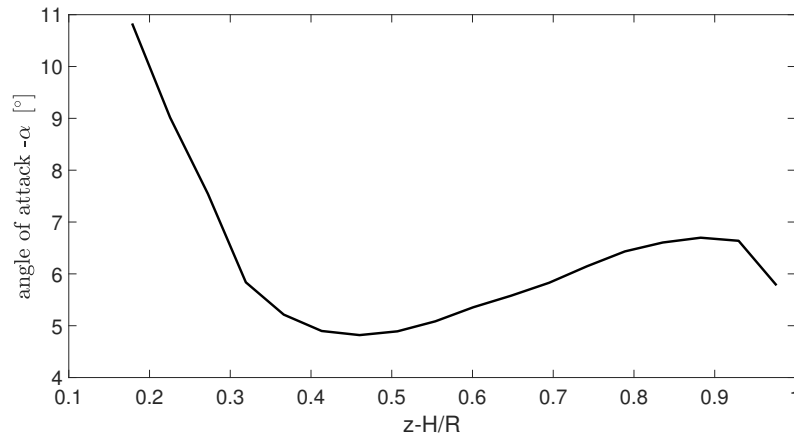
Figure 4.7: Distribution of angle of attack, α along the lifting line
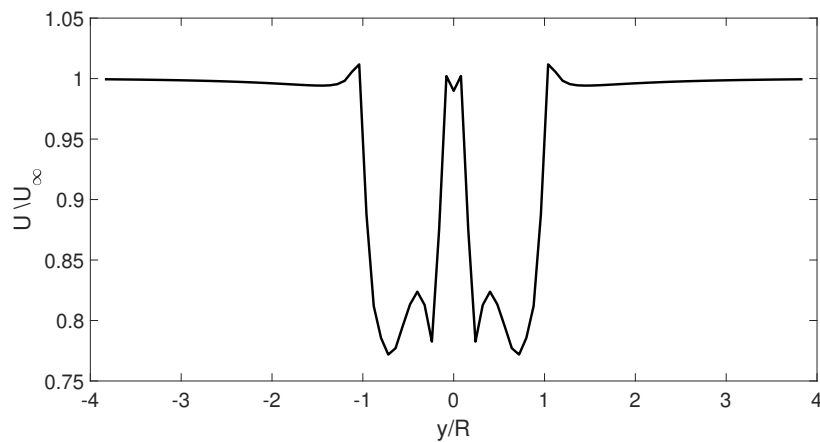
Figure 4.8: Horizontal velocity profile in the cross flow direction at hub height at rotor plane. Number of points along the scan line is 100
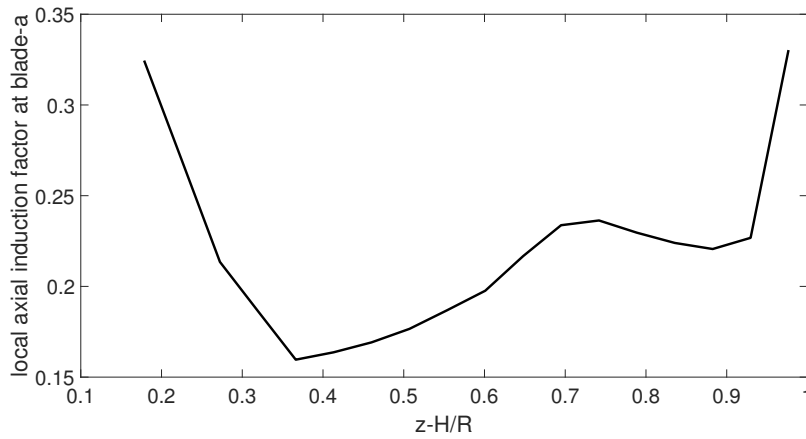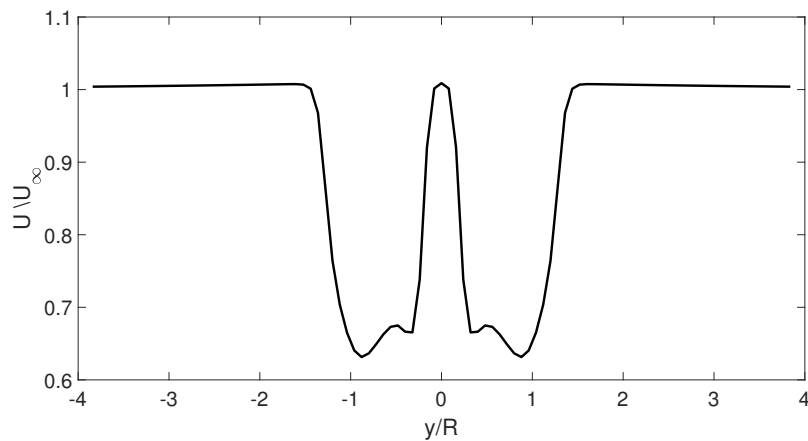
Figure 4.9: Horizontal velocity profile in the cross flow direction at hub height and at $x - 2.5D$. Number of points along the scan line is 100

4.2.1   Effect of N_r

The number of span-wise vortex filaments is doubled to see it's influence on the solution. The distribution of local axial induction factor, a, at the blade and the lift coefficient, C_l, along the blade are plotted in Figures 4.10 and Figure 4.11. The distribution of lift coefficient and local axial induction vary with variation in N_r. The distributed obtained using $N_r = 36$ is the most accurate one.
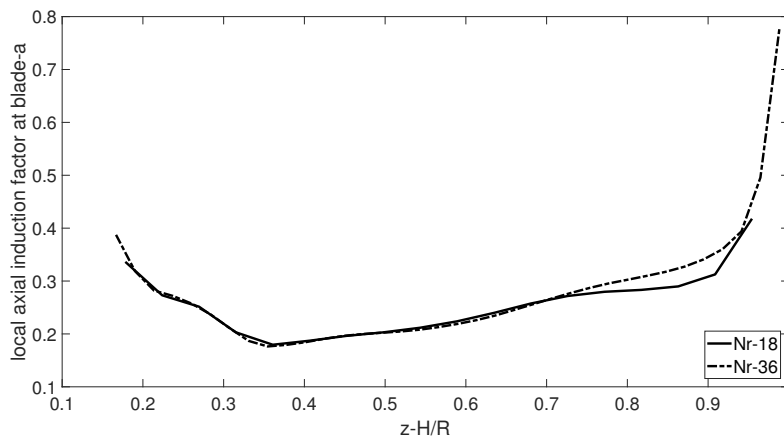
Figure 4.10: Distribution of local axial induction factor, a, along the lifting line for two different values of N_r.

Horizontal velocity profile at hub height in the cross flow direction and $x = 2.5D$ is plotted in Figure 4.12. There is no significant improvement in the velocity profiles at $x = 2.5D$ after using more span-wise vortex filaments.
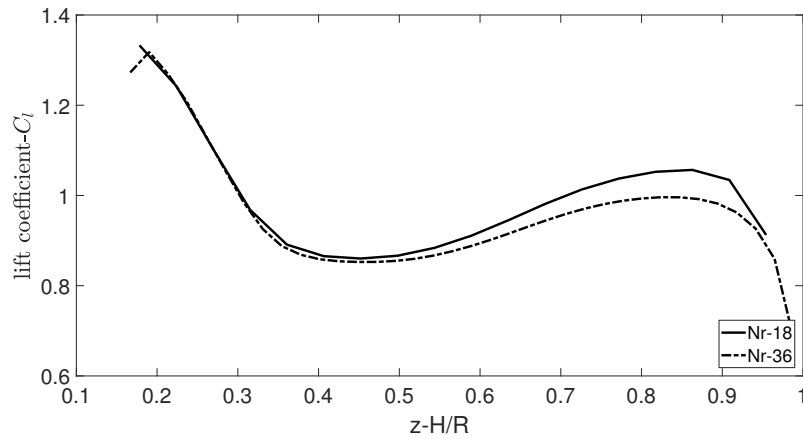
Figure 4.11: Distribution of lift coefficient, C_l, along the lifting line for two different values of N_r.
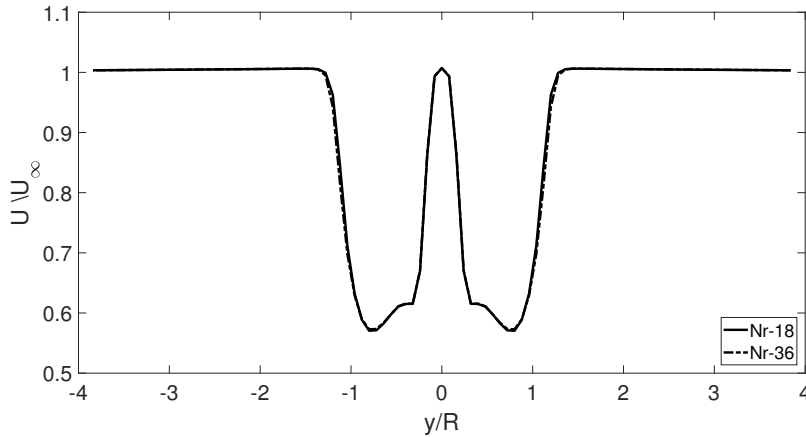
Figure 4.12: Horizontal velocity profile in the cross flow direction at hub height and at $x = 2.5D$ for two different values of $N_r = 18, 36$. Number of points along the scan line is 100

4.2.2 Comparison between constant axial induction rotor model and varying axial induction rotor model

A comparison is made between two new models: constant axial induction along the rotor and varying axial induction along the lifting line. The input parameters to the helical model are, $N_h = 320$, $N_r = 36$ and $N_b = 3$, N_r. The simulation is carried out for an existing wind turbine. The average axial induction along the lifting line is taken from the thrust coefficient curve in Figure B.1 for a uniform wind speed of 11m/s. The obtained horizontal velocity profile at $2.5D$ is shown in Figure 4.13. The constant axial induction model predicts a fairly constant velocity profile inside the wake radius, whereas, the varying axial induction model predicts a non uniform

velocity profile. A similar comparison is made between horizontal velocity profiles in the cross flow direction at hub height at the rotor plane (see Figure 4.14). The velocity profile predicted by the constant axial induction rotor model is fairly constant along the mid span. Due to tip losses, the velocity is not constant throughout the rotor. The velocity profile predicted by the radially varying axial induction model is not uniform. The axial induction factor is distributed along the span. The axial induction is higher, near the edges of the rotor (see Figure 4.14).
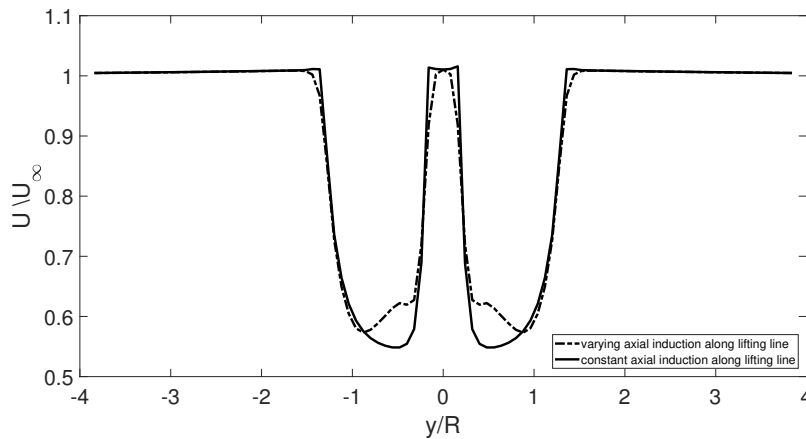
Figure 4.13: Horizontal velocity profile in the cross flow direction at hub height and at $x = 2.5D$ predicted by two different rotor models, constant axial induction model, and radially varying axial induction model. Hundred points were used along the scan line
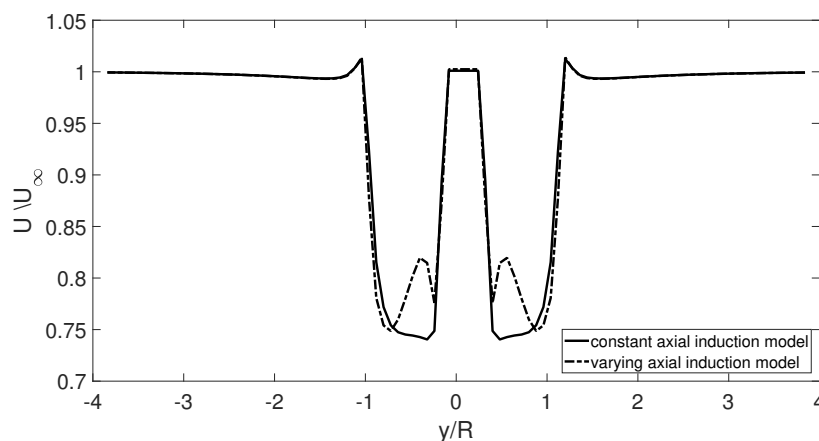
Figure 4.14: Horizontal velocity profile in the cross flow direction at hub height and rotor plane predicted by two different rotor models, the constant axial induction model, and radially varying axial induction model. Hundred points were used along the scan line
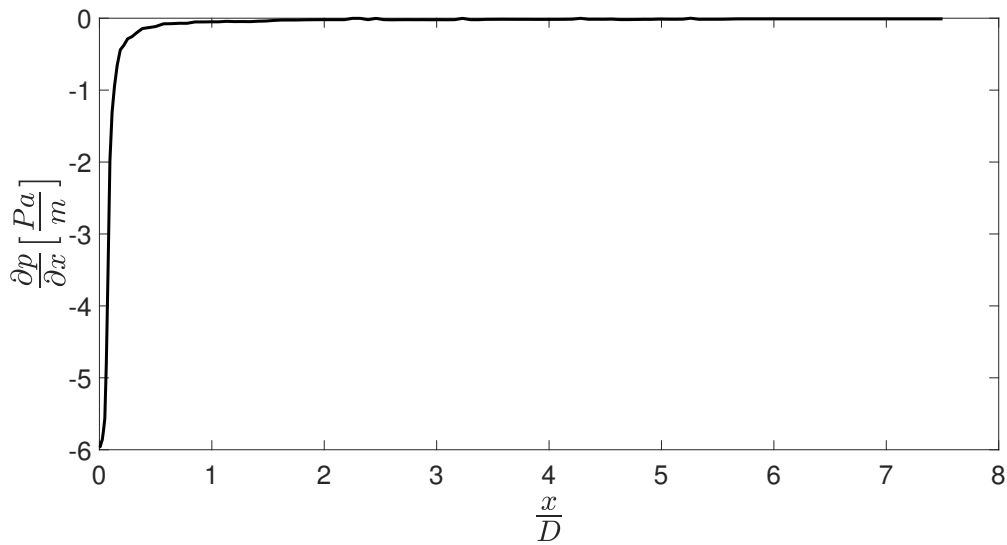
Figure 4.15: Axial pressure gradient at hub-height and at $y = 0.5R$ as a function of distance downstream of the turbine

4.2.3 Axial pressure gradient

The axial pressure gradient $\frac{\partial p}{\partial x}$ was calculated using the equation 3.27. At the centre of wake, the velocity becomes free stream velocity. Hence a different evaluation point was used for the evaluation of the pressure gradient. The input parameters used are listed in Table 4.2. The axial pressure gradient at hub height and at $y = 0.5R$, obtained from Navier-Stokes equations is depicted in the figure 4.15. The trend in axial pressure gradient is in agreement with momentum theory.

<div align="right">

Chapter 5

</div>

WAKEFARM Results

The two new vortex models explained in the two previous chapters were implemented in WAKEFARM. The results obtained from WAKEFARM were validated with experiments. This chapter gives a detailed explanation of the same.

5.1   Validation with EWTW measurements

Initially in this section, the first model (constant axial induction model) explained in 3 is validated. The second model explained in 4 is validated later in this ection. A comparison is made between the results of existing Vortex ring model (see section 3.1.2) and tube files (see section 3.1.1) with the constant axial induction model. The velocity profiles in 2 locations downstream of the turbine, namely, $2.5D$ and $3.5D$ are compared with the results obtained from the measurements at EWTW, ECNS wind turbine test field. ECN's Wind Turbine Test field Wieringermeer (EWTW) has 5 Nordex80 wind turbines of $2.5MW$ with a hub height and diameter of $80m$, situated in a row. A met mast is situated close to $T5$ and $T6$, as shown in Figure 5.1. The distance between the turbines is $3.8D$ ($305m$). The first turbine ($T5$) in the row, is free from wake effects [8]. The meteorological data is measured by met mast MM3. The data used for validation in this section is measured using sonic cup anemometer at hub height ($80m$) [8]. The row is inclined $95°$ with respect to north. Figure 5.1 shows the directions and distances from the mast to the wind turbines. When the wind blows from $31°$ or $315°$, the velocity at the center of the wake is measured. When the wind flows from other directions, the distance y to the wake center is calculated as follows,

$$y = S \cdot \sin \alpha \tag{5.1}$$

the error e in the distance from the rotor is evaluated as (Figure 5.2):

$$e = S - S \cdot \cos \alpha \tag{5.2}$$

The velocity at a circle with radius $2.5D$ and $3.5D$ is measured in the experiments. Measurements for 3 different mean wind speeds, $9m/s$, $11m/s$ and $13m/s$ are
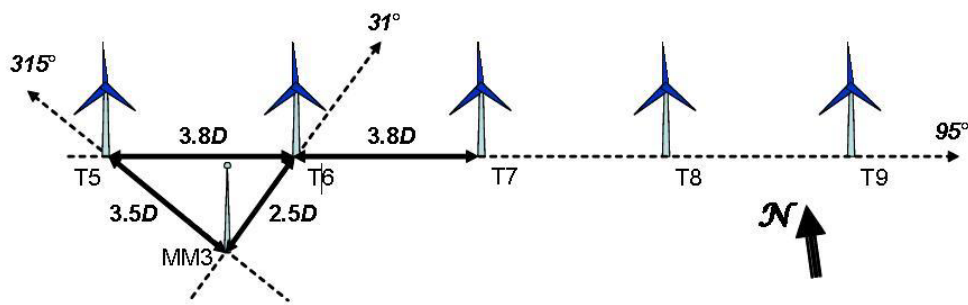
Figure 5.1: Location of wind turbines and meteorological measurement mast at EWTW [8].
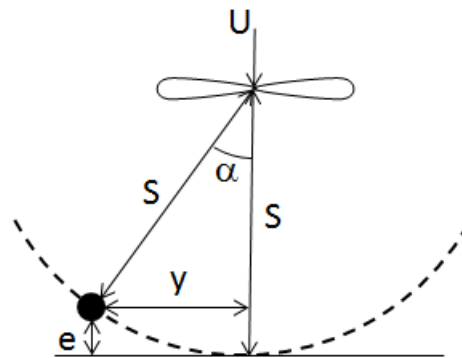
Figure 5.2: Top view of EWTW experimental setup. In yawed conditions, the met mast shifts along the dashed line with respect to the rotor.
[8].

selected. Figure 5.3 and Figure 5.4 show the measured velocity profiles at $2.5D$ and $3.5D$ downstream of the rotor. The maximum velocity deficit is higher at lower wind speeds. This is because, the axial induction factor is high at low wind speeds owing to higher tip speed ratios λ.

5.1.1   Comparison of different near wake models

The WAKEFARM results obtained using the old and new near wake models are compared with the EWTW experiments. The horizontal velocity profiles at $2.5D$ and $3.5D$ at hub height are plotted. The input parameters used for the simulation are given in table below.

The input parameters used in the helical model are given in table 5.2. The diameter D and hub height H are specified according to the dimensions of wind turbine
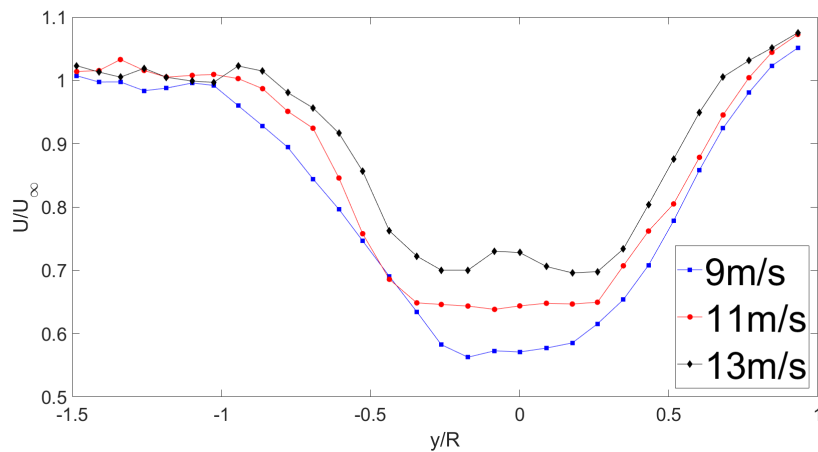
Figure 5.3: Horizontal velocity profile in a single wake at x-$2.5D$ measured at EWTW site for 3 ambient wind speed classes [8].
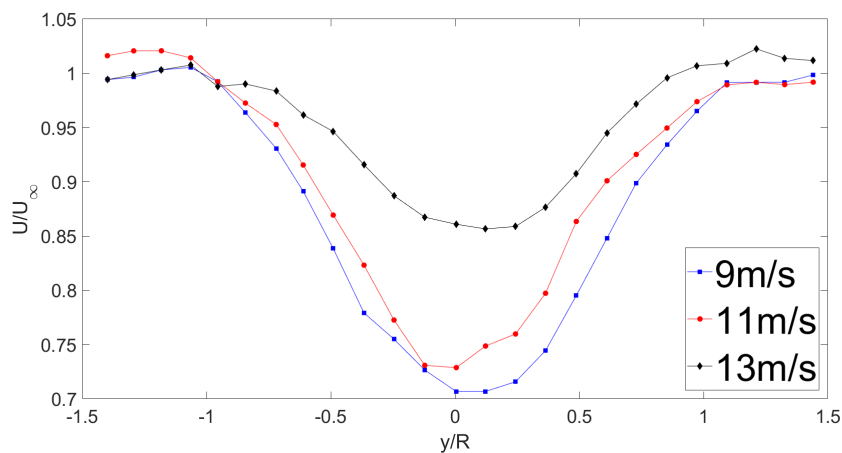
Figure 5.4: Horizontal velocity profile at x-$3.5D$ behind the rotor, measured at EWTW site for 3 ambient wind speed classes [8].

at EWTW. The ends of x-axis and y-axis are selected based on the spacing between the turbines in EWTW test site. The length of the z-domain is same as the length of y-domain. The axial induction factor a is not known from the experiments, hence a is taken from the thrust coefficient curves of the wind turbines (Thrust coefficient as a function of free stream velocity) in the site. The stability of the atmosphere is also not known from the measurements. A slightly stable (near neutral) atmosphere is assumed for the simulation. The root radius is taken as $2.2m$ initially. In this case, the cylindrical root section is ignored and the airfoil shaped blade is assumed to start at the hub of wind turbine rotor.

Table 5.1: Inputs parameters to WAKEFARM wake model.

Parameters	Value
U_∞	$11m/s$
D	$80m$
a	0.25 (thrust coefficent curves)
H	$80m$
z_0	$1.8x10^{-2}$
u_*	$0.48m/s$
L	$440m$
Xend	$7.5D$
Yend	$3.8D$
Mesh size	$119 \times 97 \times 97$

Table 5.2: Input parameters to the helical wake model

N_h	380
N_r	25
N_b	12
λ	8

Velocity profiles at $2.5D$ downstream of the wind turbine

Due to the turbulent diffusion, the velocity deficit is reduced, and the hat shaped horizontal velocity profile (seen in the inviscid results) transforms into a gaussian shaped velocity profile. This gaussian shaped velocity profiles can be seen in Figure 5.5. The width of the wake is predicted correctly by all the three near wake models considered. The newly developed helical model (constant axial induction model) correlates well with the experimental data. The velocity deficits obtained from the other two models are smaller than the helical model. The helical model has a flattened velocity profile near the centre of the wake. The flattened profile can be attributed to the root vortex. The experimental data has a flattened velocity profile, inside the wake, whereas the WAKEFARM results are more or less gaussian shaped. This can be attributed to the larger turbulence intensity values in the near wake of the WAKEFARM model.

Velocity profiles at $3.5D$ downstream of the wind turbine

The wake radius at $3.5D$ of downstream is predicted accurately by all the three models in WAKEFARM. Both tube files and the helical wake model (constant axial induction model) have good correlation with experimental data. The influence of the

root vortex still can be seen in the horizontal velocity profile predicted by the helical model. The other two models don't capture the effect of root vortex The non-physical behaviour seen in Oye's vortex ring model near the wake radius is because of the way pressure jump across the wake radius is treated. The irregularities in velocity profile from EWTW measurements close to the root region may be due to the errors in measurements.

Figure 5.5: Comparison of horizontal wind speed profiles predicted by three different near wake models at hub height and $x = 2.5D$, for a wind speed of $11m/s$. The root radius is taken as $2.5m$
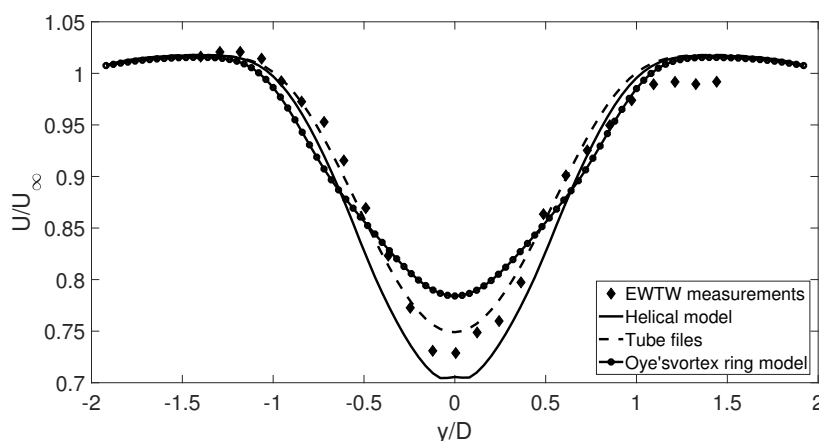
Figure 5.6: Comparison of horizontal wind speed profiles predicted by three different near wake models at hub height and $x = 3.5D$, for a wind speed of $11m/s$. The root radius is taken as $2.5m$

Varying root radius

The root radius now is changed from $2.5m$ to $6.2m$. The cylindrical root section is included in the root radius. As the root radius is increased, the velocity profile becomes more flattened at the centre. Apart from this, the maximum velocity deficit is also reduced after increasing the root radius. A similar trend is seen for the velocity profile at $x = 3.5D$ (see Figures 5.7 and Figure 5.8).

Figure 5.7: Comparison of horizontal wind speed profiles predicted by three different near wake models at hub height and $x = 2.5D$, for a wind speed of $11m/s$. The root radius is taken as $6.2m$
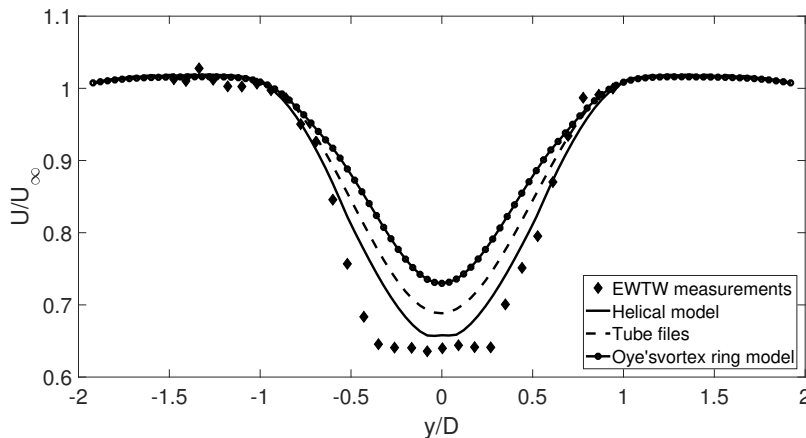

Figure 5.8: Comparison of horizontal wind speed profiles predicted by three different near wake models at z=hub height and $x = 3.5D$, for a wind speed of $11m/s$. The root radius is taken as $6.2m$
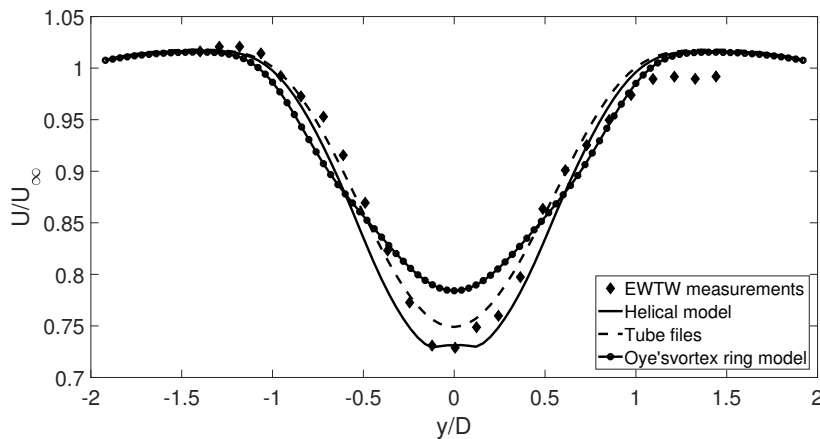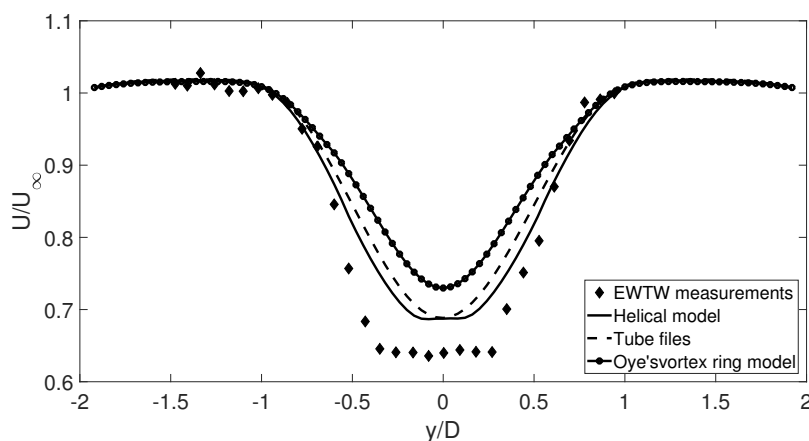
5.1.2 Effect of Number of blades, N_b

The simulation is carried out for three different values of N_b. The values of N_h, N_r are kept constant. Figure 5.9 shows the horizontal wind speed profile in $y-$ direction at hub height at $x = 2.5D$ behind the rotor for different number of blades $Nb = 3, 6, 12$. The input parameters to WAKEFARM are same as the ones listed in Table 5.1. Input parameters to the helical near wake model are listed in Table 5.2 except for N_b, which is varied. The velocity profile at $N_b = 12$ has the best correlation with experimental data. The velocity deficit increases with increase in the number of blades.

Figure 5.9: Horizontal wind speed profiles at hub height, predicted by helical model at various $x - 2.5D$ downstream of the turbine for 3 different values of $N_b = 3, 6, 12$ and for $N_r = 25$, $N_h = 320$. The wind speed at hub height is $11m/s$. The root radius is taken as $2.5m$.

Evolution of the wake

Figure 5.10 shows the evolution of horizontal wind speed profile at hub height. The wake radius increases, as we move away from the turbine. From $0.6D$ to $2.5D$, a large change can be seen in the velocity profile, due to strong pressure gradients in the near wake region. The change in shape of the velocity profile after $2.5D$ is lesser than the change in shape of velocity profile before downstream position $2.5D$. This is due to negligible pressure gradients in far wake. The double hump shape at $0.6D$ is due to the influence of root vortex. It's effect is still evident further away in wake. The size of the hump might vary depending the stability of the atmosphere.
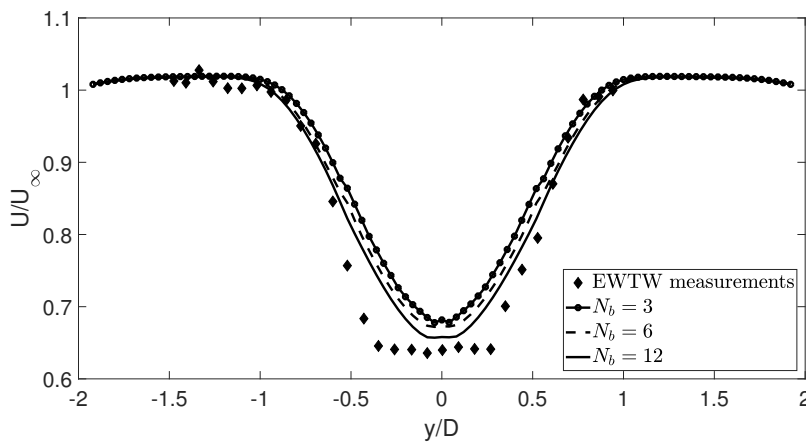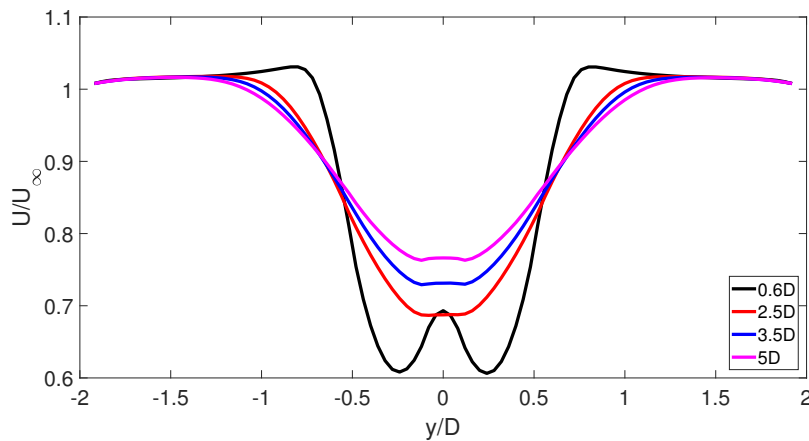
Figure 5.10: Horizontal wind speed profiles at hub height, predicted by helical model at various x-locations downstream of the turbine. The wind speed at hub height is $11 m/s$. The root radius is taken as $6.2m$

5.1.3   Comparison between constant and varying axial induction model

In this section, a comparison between the velocity profiles obtained from the constant axial induction model and varying axial induction model is made. The aerodynamic properties of the blade (chord distribution, twist distribution, aerofoil polar) needed for the varying axial induction model correspond to the aerodynamic properties of Nordex80 turbine. They are confidential, hence not included in the report. Input parameters are listed in 5.3. For the constant axial induction model, an axial induction factor $a = 0.251$ is assumed throughout the blade. This is taken from the thrust coefficient curves for Nordex80 turbine. The thrust coefficient corresponding to a wind speed of 11 m/s is selected. It is to be noted that the axial induction throughout the disc is not equal to 0.251. The axial induction distribution along the blades predicted by varying axial induction model (vortex model, before WAKEFARM) is presented in Figure 5.11. The mean value of axial induction taken along the blades is 0.2479. The horizontal velocity profiles at $2.5D$ and $3.5D$ obtained from both the models is compared with EWTW experiments.

The two velocity profiles from the WAKEFARM model look similar as opposed to the inviscid velocity profiles predicted by the vortex methods (see Figure 4.13). In addition to that, the velocity deficit obtained with constant axial induction model with 3 blades is smaller than the velocity deficit obtained with 12 blades. This can be seen by comparing the velocity profiles in Figure 5.12 and Figure 5.5. The physical explanation for the above two phenomena is not known. The constant axial induction rotor model has a better correlation with the EWTW measurements. The velocity

Table 5.3: Input parameters for comparison of constant axial induction and varying axial induction model

N_h	320
N_r	36
N_b	3
U_∞	$11m/s$
u_*	$0.48m/s$
L	$440m$
R	$40m$
z	1.8×10^{-2}
X_{end}	$7.5D$
Y_{end}, Z_{end}	$3.8D$
Mesh size	$119 \times 97 \times 97$
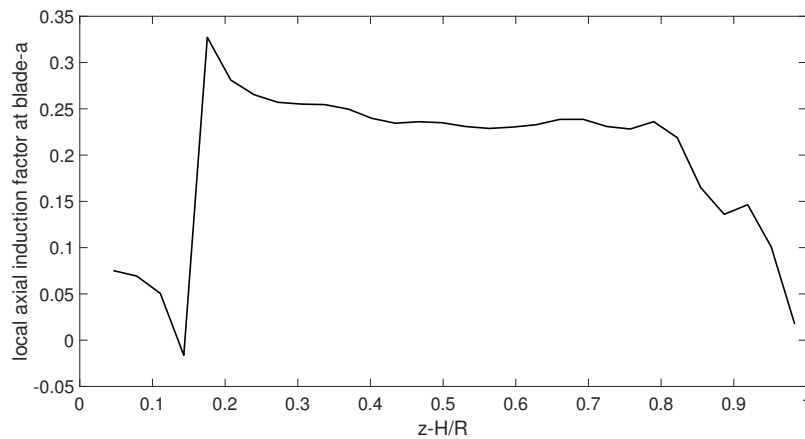
Figure 5.11: Local axial induction distribution along the blade.

profiles at $x = 3.5D$ match better with the experiments leading to the conclusion that WAKEFARM performs better in the far wake region.

5.2 Sensitivity to atmospheric boundary layer model

The influence of atmospheric boundary layer (ABL) models on the final solution is studied in this section. Two different ABL models (see section 2.4), namely Panofsky-Dutton[25] and Gryning[26] models are used for the simulations. The input parameters used for the simulation are listed in Table 5.4.

The free stream velocity profiles obtained using Panofsky-Dutton and Gryning model are shown in Figure 5.14. For a Monin-Obukhov length of $440m$ (Near neutral-
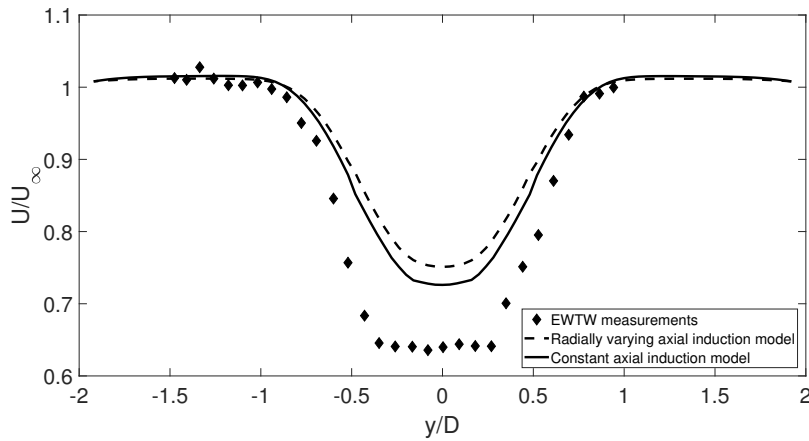
Figure 5.12: Comparison of horizontal velocity profiles at $x = 2.5D$ predicted by constant axial induction model and radially varying axial induction with EWTW experiments. The parameters used in the both the helical models $N_h = 320, N_b = 3, N_r = 36$.
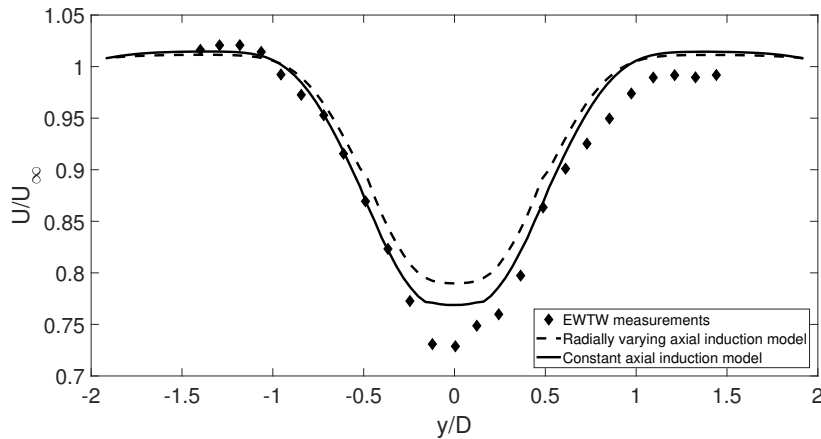
Figure 5.13: Comparison of horizontal velocity profiles at $x = 3.5D$ predicted by constant axial induction model and varying axial induction with EWTW experiments. The parameters used in the both the helical models $N_h = 320, N_b = 3, N_r = 36$

stability), the velocity profile predicted by Gryning model looks more physical. The velocity profile predicted by Gryning model is steeper compared to Panofsky-Dutton model. The steeper velocity profile is a result of larger turbulence intensity in the atmosphere. It is a characteristic of neutral atmospheric boundary layers. The centerline velocity profile at $x = 5D$ and $y = 0$ is shown in Figure 5.15. The centerline velocity profiles are not axisymmetric as compared to the velocity profile along the cross flow direction. (Figure 5.5-Figure 5.10). This can be attributed to the shear in z-direction. The velocity deficit predicted by Panofsky-Dutton model is higher than

Table 5.4: Input parameters for Panofsky-Dutton and Gryning test cases.

	Panofsky-Dutton model	Gryning model
N_b	12	12
N_h	320	320
N_r	25	25
U_∞	$11m/s$	$11m/s$
u_*	$0.48m/s$	$0.53m/s$
L	$440m$ (Stable,Near-neutral)	$440m$ (Stable,Near-neutral)
a	0.25	0.25
z_0	$0.018m$	$0.018m$
Mesh size	$119 \times 97 \times 97$	$119 \times 97 \times 97$

the velocity deficit predicted by Gryning model. This is due to smaller turbulent diffusion in Panofsky-Dutton model. Above hub height, the free stream velocity profile u_0 obtained from Panofsky-Dutton model (Figure 5.14) is a straight line. This is because the surface layer ends somewhere near hub height and Panofsky-Dutton model is not valid outside surface layer. This is reflected in final horizontal velocity profile above hub height in Figure5.15.
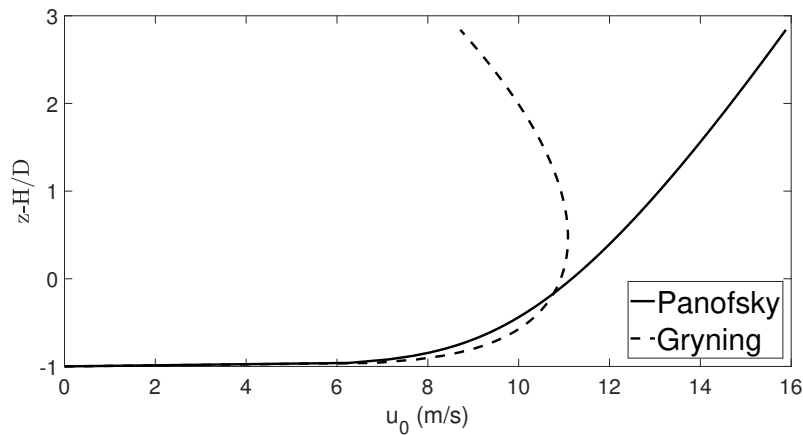
Figure 5.14: Free-stream velocity u_0 profiles obtained from Panofsky-Dutton and Gryning models. The free stream velocity at hub height is $11m/s$.

A comparison between the horizontal velocity profiles in $y-$ direction at hub height obtained using helical model for both Panofsky -Dutton ABL model and Gryning ABL model is made. The input parameters used for the simulation are listed in Table 5.4 The velocity deficit obtained using Gryning model is lesser owing to higher turbulent diffusion. The wake radius obtained using Gryning ABL model is higher compared to the wake radius obtained using Panofsky-Dutton ABL model. These effects can be observed in Figures 5.16 and 5.17 The root radius is set as $6.2m$.
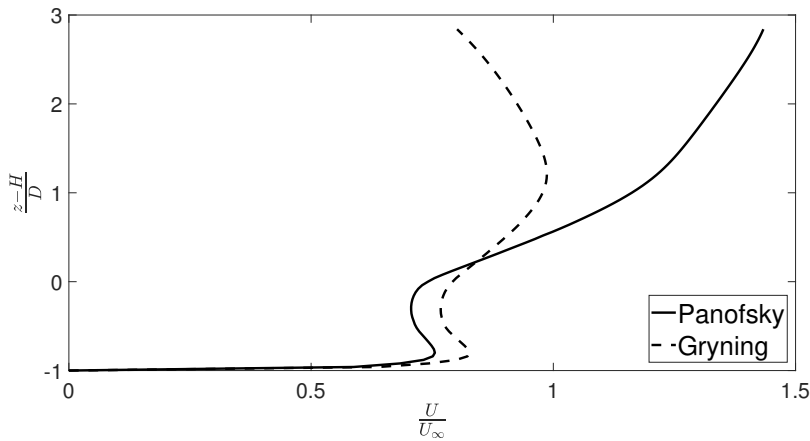
Figure 5.15: Horizontal velocity profiles along z-axis at $x = 5D$, $y = 0$ obtained from the WAKEFARM method using Panofsky-Dutton and Gryning models

Figure 5.16: Comparison of horizontal wind speed profiles at z=hub height and $x = 2.5D$, predicted by the WAKEFARM method using Panofsky-Dutton and Gryning models for a wind speed of $11m/s$. The root radius is taken as $2.5m$ and $N_b = 12$.

The input parameters to WAKEFARM are same as the ones listed in Table 5.1. The input parameters used for the helical near wake model are listed in Table 5.4. A comparison between the horizontal velocity profiles in $y-$ direction at hub height obtained using helical model for both Panofsky -Dutton ABL model and Gryning ABL model is made. Figure 5.18 and Figure 5.19 show this comparison. The contour plots of horizontal velocity profile in an $X - Z$ plane at $y = 0$ obtained for both the cases is shown in figure 5.20 and Figure 5.21.

A root radius of $2.5m$ is used for the simulation. The root vortex can be seen up to a downstream distance of $0.5D$ in Figure 5.15 and Figure 5.21. The velocity deficit obtained by using Panofsky-Dutton ABL model is higher compared to the

Figure 5.17: Comparison of horizontal wind speed profiles at z=hub height and $x = 3.5D$, predicted by the WAKEFARM method using Panofsky-Dutton and Gryning models for a wind speed of $11m/s$. The root radius is taken as $2.5m$ and $N_b = 12$.
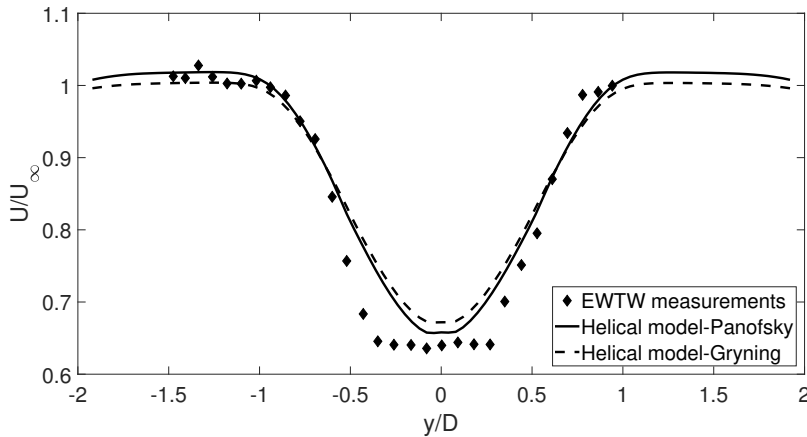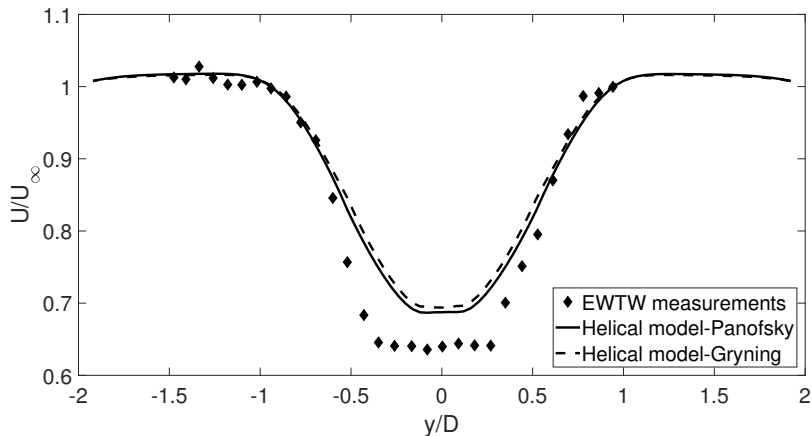

Figure 5.18: Comparison of horizontal wind speed profiles at z=hub height and $x = 2.5D$, predicted by the WAKEFARM method using Panofsky-Dutton and Gryning models for a wind speed of $11m/s$. The root radius is taken as $6.2m$ and $N_b = 12$.

velocity deficit obtained by using Gryning ABL model. In Figure 5.15 the turbulent mixing of slower inner flow (inside the wake) with the faster outer flow is less, owing to a smaller turbulent diffusion in Panofsky-Dutton model. Hence the wake takes a longer time to recover. However, in Figure 5.21 faster wake recovery can be seen due to higher turbulent diffusion.
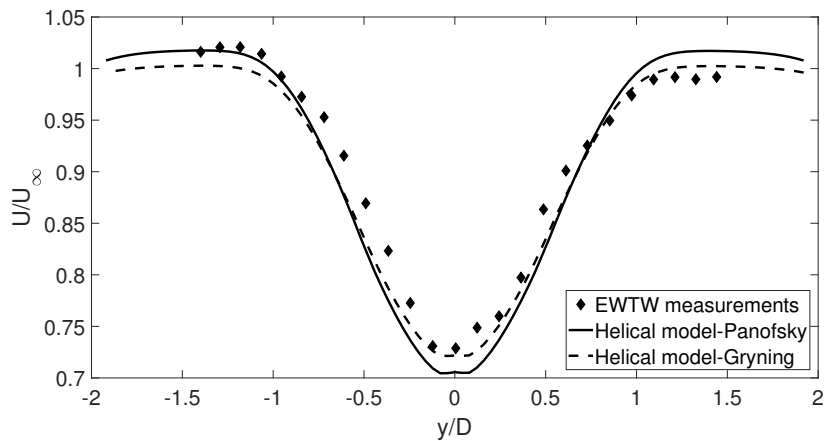
Figure 5.19: Comparison of horizontal wind speed profiles at z=hub height and $x = 3.5D$, predicted by the WAKEFARM method using Panofsky-Dutton and Gryning models for a wind speed of $11m/s$. The root radius is taken as $6.2m$ and $N_b = 12$.
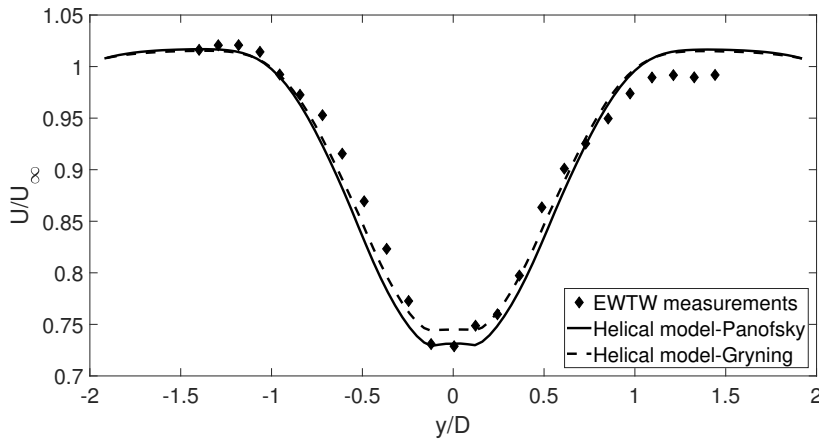
5.3 Far wake validation

Far wake is the most important region as it directly influences the power production of the next turbine, when the turbine aligned with the wind direction. The far wake of the new helical model (constant axial induction model) is validated with measurements which have been performed in the boundary layer wind tunnel of Marchwood Engineering Laboratories [36]. A comparison is also made between the velocity profiles predicted by constant axial induction helical model (Chapter 3), tube files (described in section 3.1.1) and Oye's vortex ring model (described in section 3.1.2). The scaled wind turbines used in Marchwood experiments have a rotor diameter of $0.27m$ and a hub height of $0.3m$. These measurements were performed at 3 different tip speed ratios $\lambda = 2.9$, 4.0 and 5.1 and at a free-stream velocity of $4.1m/s$. The thrust coefficients (measured) corresponding to the three tip speed ratios are: $C_T = 0.62$, $C_T = 0.79$ and $C_T = 0.85$. Since the tip speed ratios, 2.9 and 4.0 are not representative of tip speed ratios of modern wind turbines, the results corresponding to them, are not used for validation. The results corresponding to tip speed ratio $\lambda = 5.1$ were used for validation. A logarithmic free stream profile was simulated in the wind tunnel which can be approximated as [36]:

$$u_0(z) = \frac{u_*}{k} ln \left(\frac{z}{z_0} \right) \tag{5.3}$$

In WAKEFARM model, undisturbed flow u_0 is modelled using Monin-Obukhov length L, roughness length z_0 and friction velocity u_*. In Marchwood experiments, the undisturbed wind speeds at heights $(0.3m)$, $0.15m$ and $0.45m$ are $4.1m/s$, $3.7m/s$
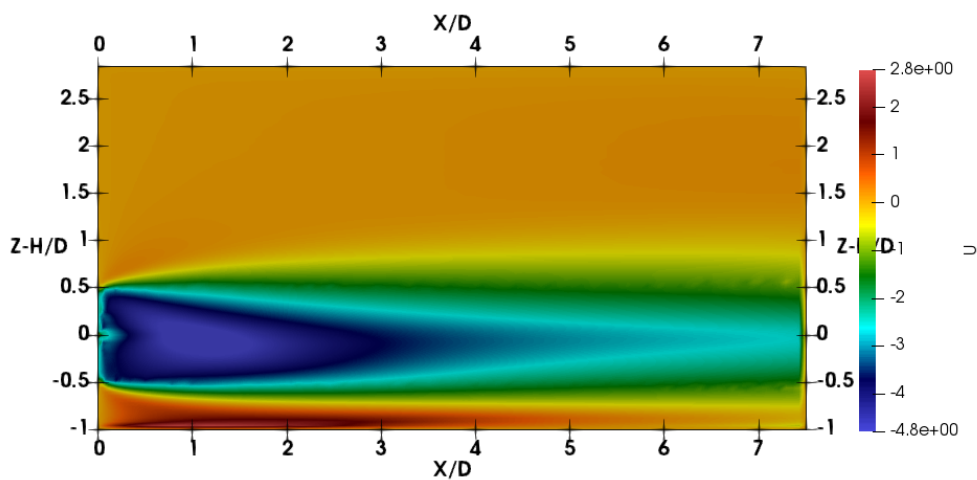
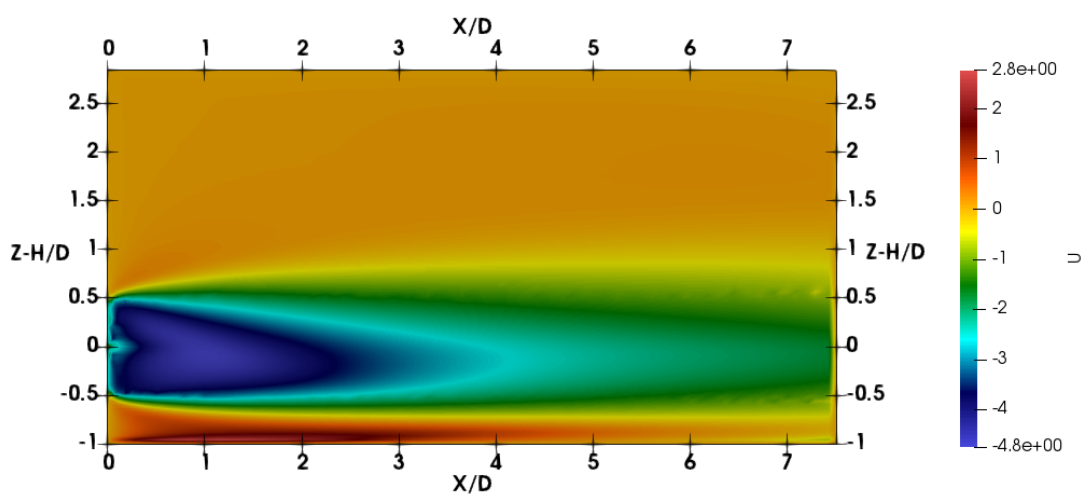**Figure 5.20:** Velocity deficit in $x - z$ plane and at $y = 0$ obtained using Panofsky-Dutton ABL model.

Figure 5.21: Velocity deficit in $x - z$ plane and at $y = 0$ obtained using Gryning ABL model.

Table 5.5: Inputs parameters to WAKEFARM .

Parameters	Value
U_∞	$4.1 m/s$
D	$0.27 m$
H	$0.3 m$
z_0	$7.56 x 10^{-6}$
u_*	$0.1444 m/s$
L	$2.4 m$
X_{end}	$7.55 D$
Y_{end}	$3.8 D$
Mesh size	$119 \times 97 \times 97$

Table 5.6: Input parameters to the constant axial induction -helical wake model

N_h	N_r	N_b	λ
380	25	12	5.1

and $4.3m/s$, respectively. In order to obtain the same free-stream conditions in WAKEFARM, the three parameters, u_*, L and z_0 were optimized. The best correlation for the undisturbed wind speed profile was obtained using $z_0 = 7.56 \times 10^{-6}$, $L = 2.4m$, and $u_* = 0.1444m/s$ [37]. The input parameters for WAKEFARM are the same as the conditions and design parameters used in Marchwood experiments. The input parameters to WAKEFARM are listed in Table 5.5. The turbulence intensity at hub height is also fitted well. The actual value of the turbulence intensity at hub height calculated by WAKEFARM is 9.3% (measured: 9.2%) [37]. The turbulence intensities at other heights deviate slightly. The velocity deficit profiles in the wake direction at downstream position $5D$ and $7.5D$ are compared with the results from Marchwood experiments. The Panofsky-Dutton ABL model was selected, as the heights are small. The centerline velocity profiles at $5D$ and $7.5D$ are compared with Marchwood measurements. The input parameters to the helical model are given in Table 5.6 The centerline velocity profile predicted by the helical model (constant axial induction model) at $5D$ has a higher velocity deficit compared to the other two models. The lower part of the velocity profile is in good agreement with experiments. The upper part of the velocity profile differs from the experiments. This is due to the difference between the free stream velocity profile in experiments and the one modelled by WAKEFARM. The free stream profiles of WAKEFARM don't exactly match with experiments. The helical model (constant axial induction model) predicts the lower part of the velocity better than the other two models. The centerline velocity profile at $7.5D$ predicted by the helical model (constant axial induction model) shows some deviation from the experiments. The centerline velocity profile

Figure 5.22: Comparison of centerline velocity profiles predicted by three different near wake models at $5D$ downstream of the turbine.

predicted by Oye's model and tube files seem to have recovered from the velocity deficit faster than the helical model. The smaller velocity deficits at $7.5D$ compared to the experiments might be because of the boundary condition specified at $7.55D$. By increasing the length of the x-axis, the higher velocity deficits can be obtained.
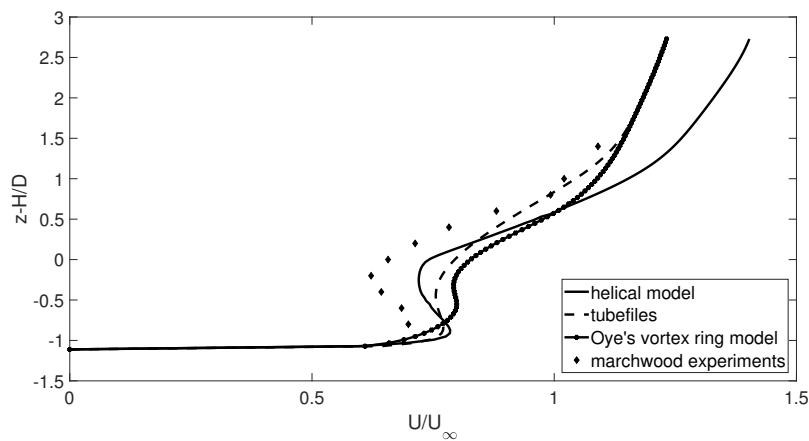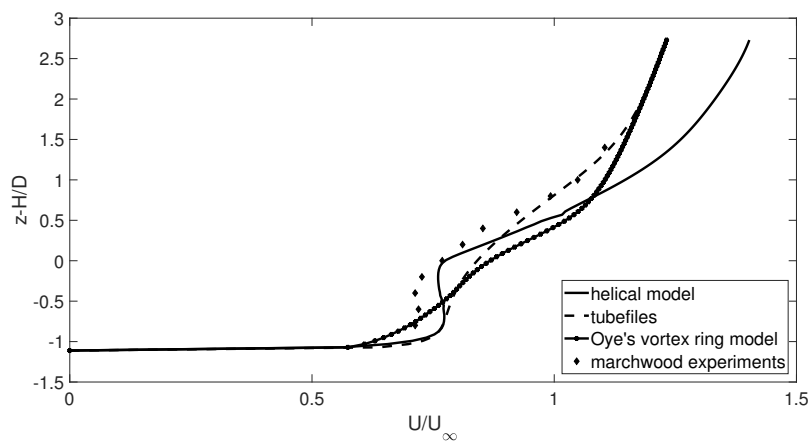

Figure 5.23: Comparison of centerline velocity profiles predicted by three different near wake models at $7.5D$ downstream of the turbine.

Chapter 6

Conclusions

1. **Constant axial induction, varying circulation model**

   - **Inviscid results** A model of wind turbine blade with constant axial induction and radially varying circulation was developed during the thesis. The wake is modelled as a helical sheet. Root vortex effect was included by specifying a root radius. Root vortex was assumed to behave in the same manner as tip vortex, i.e there is a sharp gradient in circulation distribution, which causes a strong trailing vorticity near tip and root sections. Because of this assumption, the velocity near the root section becomes free stream velocity. This can be avoided by including a model for the root section and the hub, thereby replacing a sharp gradient in bound circulation by a continuous gradient. The pressure gradients corresponding to the inviscid incompressible velocity field predicted by the helical model are calculated from the Inviscid, Incompressible Navier Stokes equations. The trend in axial pressure gradient is in agreement with the momentum theory.
     Demerits A downside of the new helical model is that it is computationally expensive compared to the previously existing vortex ring model. But since the flow in the helical wake and the resulting axial pressure gradient is only a function of the induction factor, for a set of induction factors the resulting velocity profile scaled with rotor diameter can be stored apriori in a database. This saves computation time.

   - **WAKEFARM Results**
     $y-$ **line horizontal velocity profile** The horizontal velocity profiles predicted by WAKEFARM in $y-$direction were validated with EWTW measurements. The new model correlates well with the experiments compared to the existing models. The root radius of $2.2m$, $N_b = 12$, $N_r = 25$ and $N_r = 25$ produces best results. The implementation of the root vortex

79

was successful. A flattened velocity profile is observed near the centre of the wake, due to root vortex effects.

Centerline velocity profile The centerline velocity profile at $x = 5D$ predicted by the helical model has the best correlation with the Marchwood experiments. The centerline velocity proile at 7.5D predicted by the helical model, doesn't match well with the experimental data. At $7.5D$, centerline velocity profile predicted by tube files capture the trend better than the other two models. Though the trend of the centerline velocity profile at $7.5D$ predicted by helical model is not similar to the measured centerline velocity profile, the velocity deficit is closer to the velocity deficit in the experiments. The existing two models predict a faster wake recovery. This is because of the boundary condition specified at $x = 7.55D$. Higher velocity deficit can be obtained by extending the length of $x-$domain.

2. **Radially varying axial induction, radially varying circulation model** In this model, an iterative process is followed, where the bound circulation is calculated iteratively by equating the lift force from Kutta Juokowsky theorem with the lift force calculated from local flow at the blade section.

   - **WAKEFARM results**

     $y-$**line horizontal velocity profile** While comparing the horizontal velocity profiles at hub height in the cross flow direction predicted by constant axial induction model and varying axial induction model, it was found that the constant axial induction model performs better and has a better correlation with the experimental data. The shape of the velocity profiles obtained from constant axial induction model and radially varying axial induction model, look similar.

3. **Atmospheric boundary layer stability model** Two different ABL models, Panofsky and Gryning were compared. The Gryning ABL model has greater turbulent diffusion, hence a faster wake recovery compared to the Panofsky ABL model. As the size of wind turbines have increased, the approximation that the wind turbines operate in the surface layer is not valid. Hence Panofsky ABL model is not reliable outside the surface layer. The velocity boundary layer is predicted by Panofsky Dutton model as a straight line outside the surface layer. This is also reflected in the centerline velocity profiles in regions above hub height. This might lead to an erroneous prediction of loads in the wake of the previous turbine. Thus it can be concluded that the Gryning ABL model is a better ABL model. Panofsky model can still be used for validation with wind tunnel experiments and also for simulation of wakes of smaller wind turbines.

Bibliography

[1] S. E. Gryning, H. Jørgensen, S. Larsen, and E. Batchvarova, "The wind profile up to 300 meters over flat terrain," in *Journal of Physics: Conference Series*, vol. 75, no. 1. IOP Publishing, 2007, p. 012066.

[2] R. Koole, "Performance optimization of wind turbine rotors for wind farm operation," 2015.

[3] B. Henneman, "Numerical aspects of the wakefarm program," ECN-C–03-035, ECN, Tech. Rep., 2003.

[4] J. Schepers and S. Van der Pijl, "Improved modelling of wake aerodynamics and assessment of new farm control strategies," in *Journal of Physics: Conference Series*, vol. 75, no. 1. IOP Publishing, 2007, p. 012039.

[5] S. Øye, "A simple vortex model–using vortex rings to calculate the relation between thrust and induced velocity at the rotor disc of a wind turbine," in *Proc. of the third IEA Symposium on the Aerodynamics of Wind Turbines, ETSU, Harwell*, 1990, pp. 4–1.

[6] A. Van Garrel, "Development of a wind turbine aerodynamics simulation module," 2003.

[7] M. H. M. Kloosterman, "Development of the near wake behind a horizontal axis wind turbine-including the development of a free wake lifting line code," 2009.

[8] L. A. H. Machielse, P. J. Eecen, H. Korterink, S. P. van der Pijl, and J. G. Schepers, "Ecn test farm measurements for validation of wake models," in *Proceedings of the 2007 European Wind Energy Conference & Exhibition, Milan*, 2007, pp. 7–10.

[9] J. C. Matthew, "A method for designing generic wind turbine models representative of real turbines and generic siemens swt-2.3-93 and vestas v80 specifications," 2012.

[10] B. Frank, S. Niels, J. Jeppe, and F. Peter, "Wind turbine airfoil catalogue," *Riso national laboratory*, 2001.

[11] T. Sant, "Improving bem-based aerodynamic models in wind turbine design codes," 2007.

[12] E. Branlard, "Wind turbine tip-loss corrections: review, implementation and investigation of new models," *Master's thesis, RisøDUT (Technical University of Denmark), Lyngby, Denmark*, 2011.

[13] I. E. A., "Key world energy statistics 2017," *International Energy Agency, Paris, France*, 2017.

[14] R. J. Barthelmie, K. Hansen, S. T. Frandsen, O. Rathmann, J. Schepers, W. Schlez, J. Phillips, K. Rados, A. Zervos, E. Politis *et al.*, "Modelling and measuring flow and wind turbine wakes in large wind farms offshore," *Wind Energy: An International Journal for Progress and Applications in Wind Power Conversion Technology*, vol. 12, no. 5, pp. 431–444, 2009.

[15] X. Gao, H. Yang, and L. Lu, "Optimization of wind turbine layout position in a wind farm using a newly-developed two-dimensional wake model," *Applied Energy*, vol. 174, pp. 192–200, 2016.

[16] B. Sanderse, "Aerodynamics of wind turbine wakes," *Energy Research Center of the Netherlands (ECN), ECN-E–09-016, Petten, The Netherlands, Tech. Rep*, vol. 5, no. 15, p. 153, 2009.

[17] S. Grassi, S. Junghans, and M. Raubal, "Assessment of the wake effect on the energy production of onshore wind farms using gis," *Applied Energy*, vol. 136, pp. 827–837, 2014.

[18] A. Crespo and et.al., "Numerical analysis of wind turbine wakes," in *Delphi Workshop on Wind turbine applications*, 1985.

[19] A. Crespo and J. Hernández, "Numerical modelling of the flow field in a wind turbine wake," in *3rd Joint ASCE?ASME Mechanics Conference*, 1989.

[20] H. Özdemir, M. C. Versteeg, and A. J. Brand, "Improvements in ecn wake model," in *ICOWES conference*, 2013.

[21] H. Özdemir and E. Bot, "An advanced method for wind turbine wake modeling," in *2018 Wind Energy Symposium*, 2018, p. 0515.

[22] J. H. Ferziger and M. Peric, *Computational methods for fluid dynamics*. Springer Science & Business Media, 2012.

[23] H. K. Versteeg and W. Malalasekera, *An introduction to computational fluid dynamics: the finite volume method*. Pearson Education, 2007.

[24] T. Chung, *Computational fluid dynamics*. Cambridge university press, 2010.

[25] H. A. Panofsky and J. A. Dutton, "Atmospheric turbulence: models and methods for engineering applications, 397 pp," 1984.

[26] S. E. Gryning, E. Batchvarova, B. Brümmer, H. Jørgensen, and S. Larsen, "On the extension of the wind profile over homogeneous terrain beyond the surface boundary layer," *Boundary-Layer Meteorology*, vol. 124, no. 2, pp. 251–268, 2007.

[27] A. S. Monin and A. M. F. Obukhov, "Basic laws of turbulent mixing in the surface layer of the atmosphere," *Contrib. Geophys. Inst. Acad. Sci. USSR*, vol. 151, no. 163, p. e187, 1954.

[28] A. Sathe, J. Mann, T. Barlas, W. Bierbooms, and G. J. W. van Bussel, "Influence of atmospheric stability on wind turbine loads," *Wind Energy*, vol. 16, no. 7, pp. 1013–1032, 2013.

[29] S. Mazumder, *Numerical methods for partial differential equations: finite difference and finite volume methods*. Academic Press, 2015.

[30] S. V. Patankar and D. B. Spalding, "A calculation procedure for heat, mass and momentum transfer in three-dimensional parabolic flows," in *Numerical Prediction of Flow, Heat Transfer, Turbulence and Combustion*. Elsevier, 1983, pp. 54–73.

[31] A. Nemes, M. Sherry, D. L. Jacono, H. M. Blackburn, and J. Sheridan, "Evolution and breakdown of helical vortex wakes behind a wind turbine," in *Journal of Physics: Conference Series*, vol. 555, no. 1. IOP Publishing, 2014, p. 012077.

[32] V. L. Okulov, J. N. Sørensen, and D. H. Wood, "The rotor theories by professor joukowsky: Vortex theories," *Progress in aerospace sciences*, vol. 73, pp. 19–46, 2015.

[33] E. Branlard, *Wind Turbine Aerodynamics and Vorticity-Based Methods*. Springer, 2017.

[34] P. Fuglsang, I. Antoniou, N. N. Sørensen, and H. A. Madsen, "Validation of a wind tunnel testing facility for blade surface pressure measurements," *RISO-REPORTS-RISO R*, 1998.

[35] I. H. Abbott and A. E. Von Doenhoff, *Theory of wing sections, including a summary of airfoil data*. Courier Corporation, 1959.

[36] J. F. Ainslie, U. Hassan, H. G. Parkinson, and G. J. Taylor, "A wind tunnel investigation of the wake structure within small wind turbine farms," *Wind Engineering*, pp. 24–31, 1990.

[37] J. G. Schepers, *ENDOW: Validation and improvement of ECN's wake model*. Energy research Centre of the Netherlands ECN, 2003.

[38] V. Bachtiar, F. Davies, and F. Danson, "A combined model for improving estimation of atmospheric boundary layer height," *Atmospheric environment*, vol. 98, pp. 461–473, 2014.

Velocity induced by Vortex ring

The analytical formulae for velocity induced by vortex ring with strength Γ which are derived from Biot Savarts law and are given below, [5]

$$w_x(x,y) = \frac{\Gamma}{2\pi} \frac{1}{\sqrt{x^2 + (y+a)^2}} \left(\frac{a^2 - x^2 - y^2}{x^2 + (y-a)^2} E(k) + K(k) \right) \tag{A.1}$$

$$w_y(x,y) = \frac{\Gamma}{2\pi y} \frac{x}{\sqrt{x^2 + (y+a)^2}} \left(\frac{a^2 + x^2 + y^2}{x^2 + (y-a)^2} E(k) + K(k) \right) \tag{A.2}$$

$$k = \sqrt{\frac{4ay}{x^2 + (y+a)^2}} \tag{A.3}$$

where $K(k)$ is complete elliptic integral of first kind $E(k)$ is complete elliptic integral of second kind a is the wake radius In 2D field, y is the $y-$coordinate of the evaluation point and in a 3D field, y becomes the radial position of the evaluation point
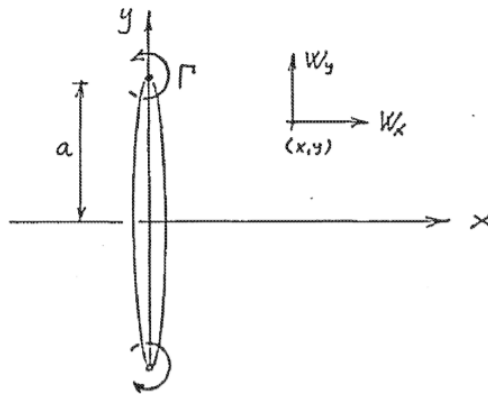

Figure A.1: Conventions in vortex ring model

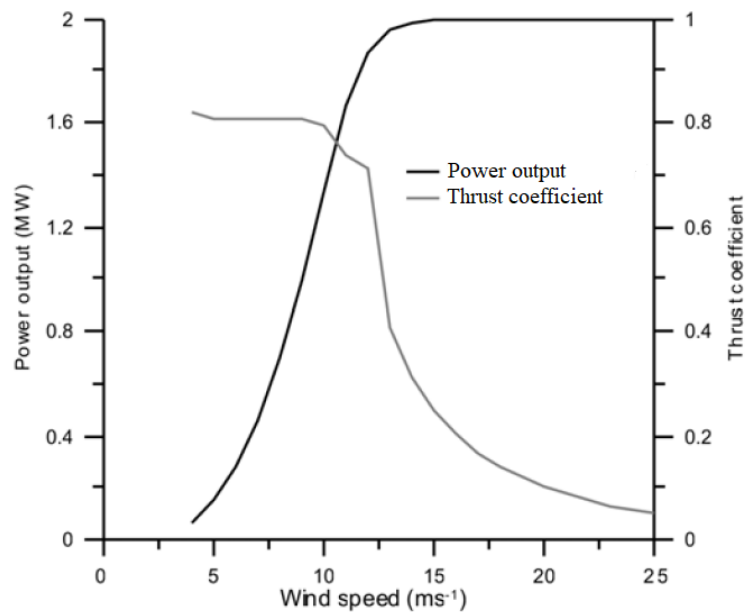# Wind turbine Geometrical and Aerodynamic data

Figure B.1: power and thrust coefficient curves as function of wind speed for the selected wind turbine [9].

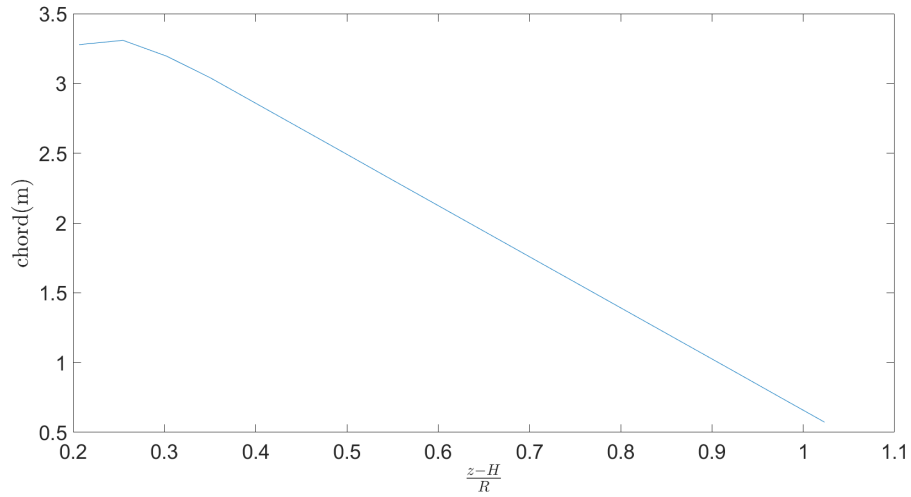The airfoils used in the blade are shown in Figures B.4 to B.8.

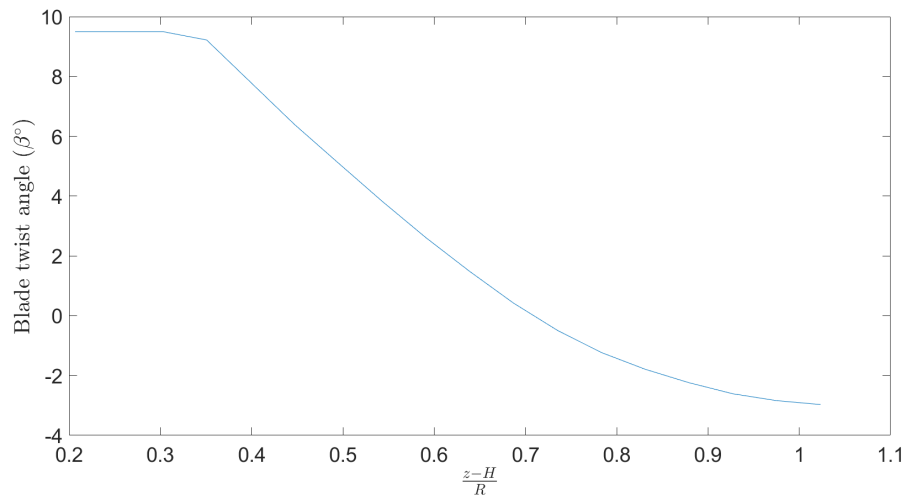**Figure B.2:** Chord distribution in the selected wind turbine.

Figure B.3: Twist distribution in the selected wind turbine.

Table B.1: generic aerofoil properties for the selected wind turbine

radius (m)	c (m)	twist (deg)	airfoil
2.563	2.004	9.50	Cylinder 1
4.389	2.523	9.50	Cylinder 1
6.216	3.015	9.50	FFA W3-301
8.042	3.278	9.50	FFA W3-301
9.868	3.309	9.50	FFA W3-301
11.694	3.195	9.50	FFA W3-301
13.520	3.039	9.22	FFA W3-241
15.346	2.863	7.81	FFA W3-211
17.173	2.687	6.40	FFA W3-211
18.999	2.511	5.11	FFA W3-211
20.825	2.334	3.83	FFA W3-211
22.651	2.158	2.61	NACA 63-221
24.477	1.982	1.48	NACA 63-221
26.304	1.806	0.42	NACA 63-221
28.130	1.630	−0.49	NACA 63-221
29.956	1.454	−1.23	NACA 63-218
31.782	1.278	−1.79	NACA 63-218
33.608	1.102	−2.24	NACA 63-218
35.435	0.926	−2.61	NACA 63-218
37.261	0.749	−2.84	NACA 63-218
39.087	0.573	−2.97	NACA 63-218
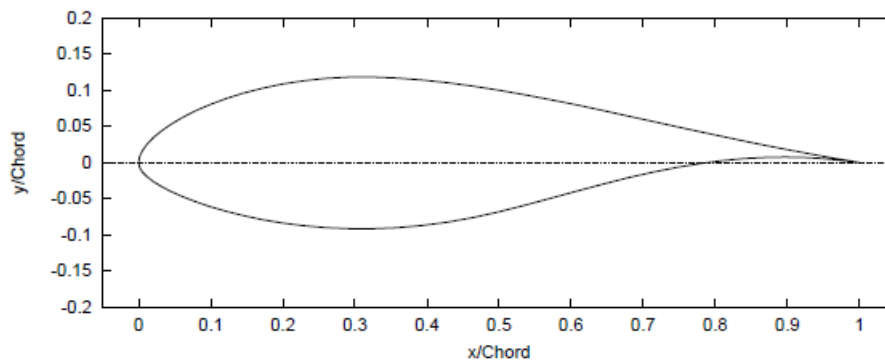
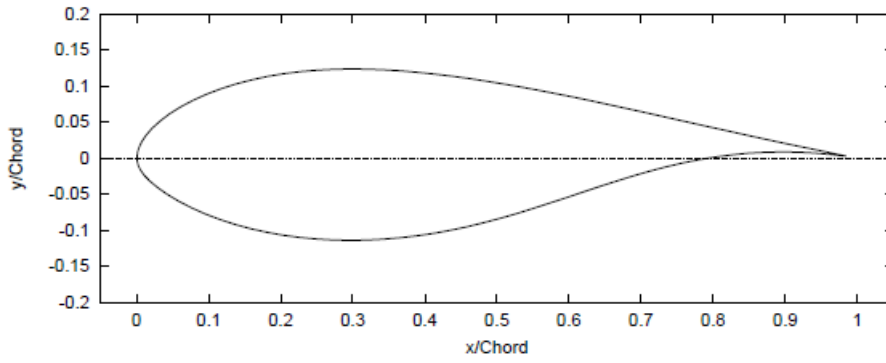
Figure B.4: FFAW3-211 airfoil [10]
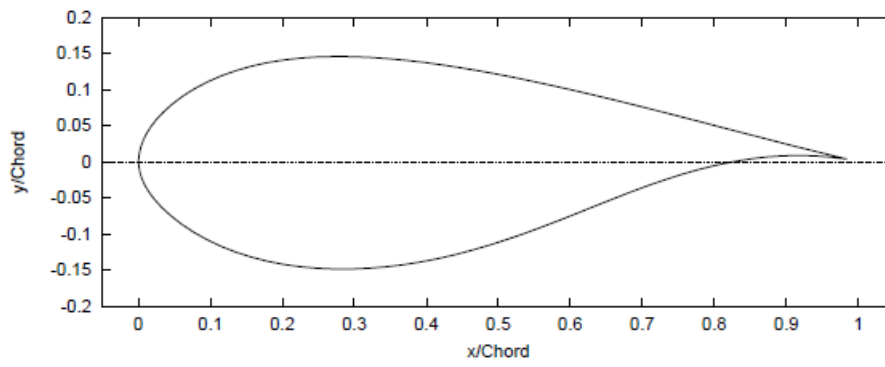
Figure B.5: FFAW3-241 airfoil [10]

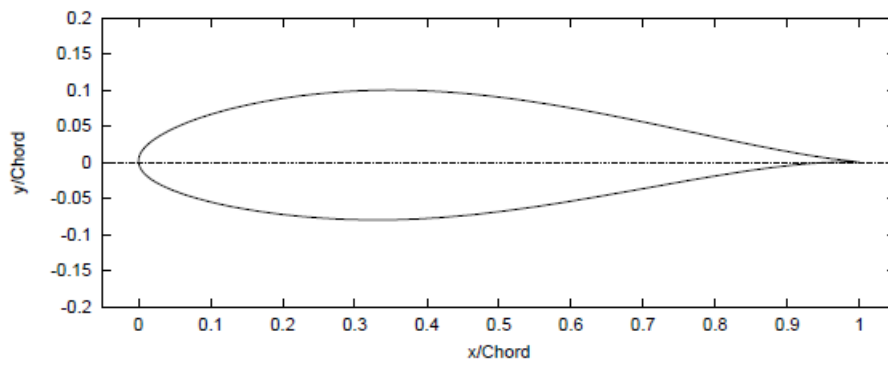**Figure B.6:** FFAW3-301 airfoil [10]

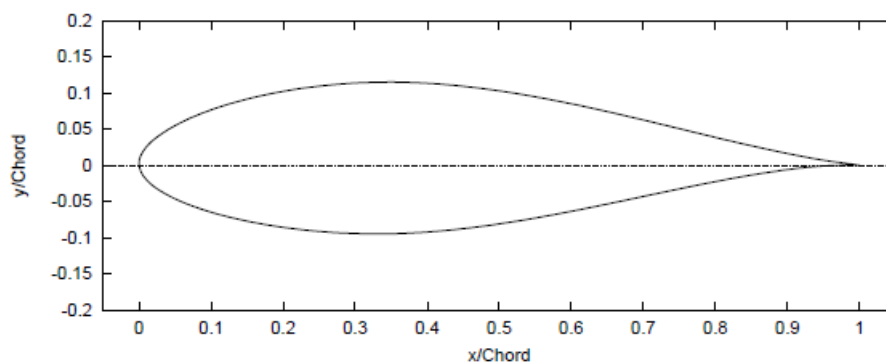**Figure B.7:** NACA63-218 airfoil [10]

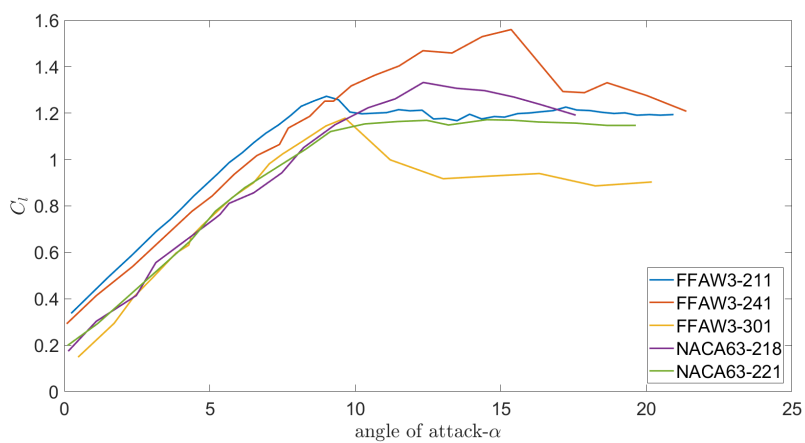**Figure B.8:** NACA63-221 airfoil [10]

Figure B.9: The lift coefficient C_l as a function of angle of attack α for the five different airfoils
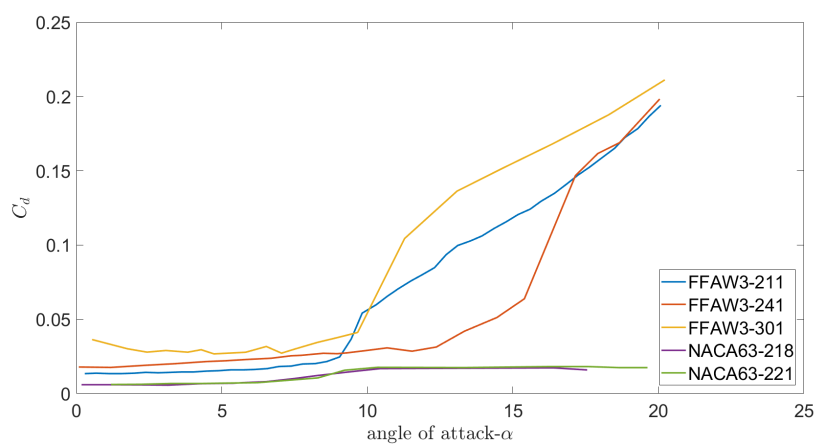

Figure B.10: The drag coefficient C_d as a function of angle of attack α for the five different airfoils

Stability classification and Monin Obukhov length

C.0.1   Monin Obukhov Length (L)

The Monin-Obukhov length is used to describe the role of buoyancy in turbulent flows, particularly in surface layer of atmosphere. Monin-Obukhov length can be defined as the height at which turbulence generated by buoyancy is more than the mechanical turbulence. The Monin-Obukhov length L is defined by [27, 38]

$$L = -\frac{u_*^3 \rho C_p \theta}{kQg} \tag{C.1}$$

where $k \equiv 0.4$ is the von Karman constant[18], C_p specific heat capacity at constant pressure, θ potential temperature, Q turbulent heat flux defined as follows

$$Q = \rho C_p \overline{\theta' w'} \tag{C.2}$$

w', θ' are the turbulent fluctuations of vertical velocity w and potential temperature θ. The Monin-Obukhov length is an indicator of atmospheric stratification. The stratification stability is divided into three cases. When L is positive the atmosphere is stable, while a negative value of L represents an unstable atmosphere. Neutral atmospheric condition is represented by an infinite value of L.

Stable atmosphere ($L > 0$)

During night time and during winter, the surface of the earth is cooler than the surrounding air (temperature gradient is positive). When an air parcel rises from the ground, it sinks to it's original position, as the rising air parcel has a higher density compared to the surrounding air. The turbulence in the atmosphere is suppressed. Such an atmosphere is called stable atmosphere.

Unstable atmosphere ($L < 0$)

Unstable atmosphere happens during a very sunny weather and during day time. During this time, the air in surface is warmer than the surrounding air above (temperature gradient is negative). When an air parcel rises from the ground, it continues to rise (the buoyancy force amplifies the motion of air upwards). Thereby the turbulence in the atmosphere is increased. Owing to a lot of mixing, the higher wind speed at the top of boundary layer is transported to lower altitudes, resulting in a steeper wind profile.

Neutral atmosphere ($L - \infty$)

In this case, the temperature gradient is negligible and turbulence is highest near the surface. Neutral stratification happens usually early in the morning or for a limited amount of time in the evening.

C.0.2 Stability correction functions

The Monin-Obukov function ψ_m in equation (2.33) has to be determined from experiments and is different for the three thermal stratification cases. For neutral stability, ϕ_m can be assumed 1, so that the profile is purely logarithmic (see equation (2.32)). These functions were adopted from Crespo et.al.[18].

$$\phi_m = \begin{cases} \left(1 + 5\left(\frac{z}{L}\right)\right), & \text{if } L > 0 \\ \left(1 - 16\frac{z}{L}\right)^{-0.25}, & \text{if } L < 0 \end{cases} \tag{C.3}$$

For stable conditions $(L > 0)$, integral in equation (2.33) reduces to

$$\Psi_m(\xi) = -5\xi \tag{C.4}$$

$$\Psi_k(\xi)(\xi) = \left(\frac{(1 + 2.5(\xi)^{0.6})^{1.5}}{\phi_m}\right)^{0.5} \tag{C.5}$$

$$\Psi_e = (1 + 2.5(\xi)^{0.6})^{1.5} \tag{C.6}$$

$$\Psi_h(\xi) = -5(\xi - \xi_0) \tag{C.7}$$

where,

$$\xi = \frac{z}{L}, \qquad \xi_0 = \frac{z_0}{L} \tag{C.8}$$

For unstable conditions $(L < 0)$, the evaluation of integral in equation (2.33) is more complicated,

$$\Psi_m(\xi) = ln\left(\frac{1 + \gamma^2(1 + \gamma)^2}{8}\right) - tan^{-1}(\gamma) + \frac{\pi}{2} \tag{C.9}$$

$$\Psi_k(\xi) = \frac{1 - \xi}{\phi_m} \tag{C.10}$$

$$\Psi_e(\xi) = 1 - \xi \tag{C.11}$$

$$\Psi_h = ln\left(\frac{1 + (\gamma(\xi))^2}{2}\right) \tag{C.12}$$

where $\gamma(\xi) = \frac{1}{\phi_m(\xi)}$. It should be noted that the above mentioned equations are valid only for heights, $z > z_0$.

Components of vorticity in a wind turbine blade

There are three vorticity components in a wind turbine blade, namely bound vorticity, trailed vorticity and shed vorticity. According to the Kutta-Joukowski theorem , the lift force is associated with bound circulation (circulation around an aerofoil). Helmotzs theorem states that vortex line cannot start and end in fluid. According to this theorem, the vorticity associated with bound circulation has to be trailed into the wake from the trailing edge and the blade extremities (the blade root and the tip for a rotor). The component of vorticity in streamwise direction is called trailed vorticity. The circulation of trailed vorticity Γ_t is equal to the bound circulations gradient.

$$\Gamma_t(r) = \frac{\partial \Gamma_b}{\partial r}(m^2/s)$$ (D.1)

If the wind turbine blade has a constant circulation, vortices are trailed only from root and tip. If a gradient of bound circulation is present, vorticity is trailed throughout the blade. The time variation of bound circulation gives birth to shed vorticity in the spanwise direction. The shed vorticity is related to bound circulation as follows,

$$\Gamma_s(r) = \frac{\partial \Gamma_b}{\partial t}dt(m^2/s)$$ (D.2)

The vorticity sheets are convected downstream with the wake velocity. The different type of circulations involved in wind turbine blade is illustrated in Figure D.1
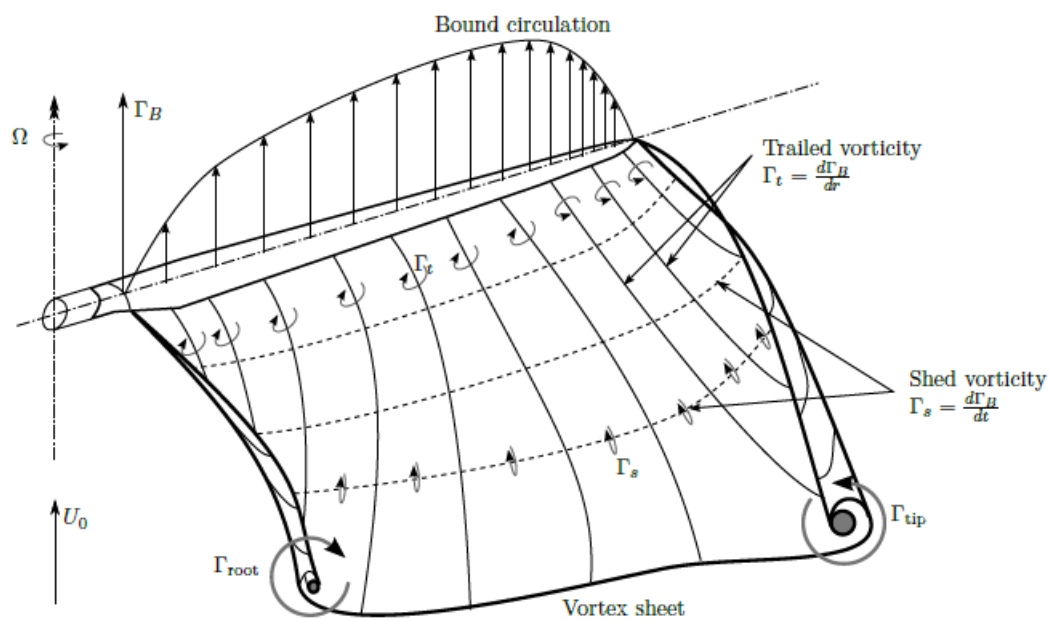
Figure D.1: Vortex sheet leaving a wind turbine blade. The trailed vortcity is generated to spanwise variation of bound circulation. The time variation of bound circulation produces shed vorticity [11, 12].